

UC Irvine

UC Irvine Electronic Theses and Dissertations

Title

Investigation of nanomaterials in the wearable electronics for health monitoring

Permalink

<https://escholarship.org/uc/item/6px4v99f>

Author

Yi, Qian

Publication Date

2022

Peer reviewed|Thesis/dissertation

UNIVERSITY OF CALIFORNIA,
IRVINE

Investigation of nanomaterials in the wearable electronics for health monitoring

DISSERTATION

Submitted in partial satisfaction of the requirements
for the degree of

DOCTOR OF PHILOSOPHY

In Engineering

by

Qian Yi

Dissertation Committee:
Professor Rahim Esfandyarpour, Chair
Professor Ozdal Boyraz
Professor James Earthman

2022

TABLE OF CONTENTS

| | |
|--|-----|
| LIST OF FIGURES | iv |
| ACKNOWLEDGEMENTS | xi |
| VITA..... | xii |
| ABSTRACT OF THE DISSERTATION | xiv |
| Chapter I. Introduction..... | 1 |
| Chapter II. Predictive 3D printing resolution model for optimizing 3D printing parameters | 5 |
| 2.1 Overview | 5 |
| 2.2 Investigation for pneumatic printing process | 6 |
| 2.3 Determination of the viscoelastic behavior of the printed material | 10 |
| 2.4 Boundary limitation..... | 14 |
| 2.4.1 Ink extrusion | 15 |
| 2.4.2 Filament deposition | 19 |
| 2.5 Future work: Physic-guided machine learning model..... | 24 |
| Chapter III. All-3D-printed, flexible, and hybrid wearable bioelectronic sensors using biocompatible nanocomposites for health monitoring..... | 26 |
| 3.1 Overview | 26 |
| 3.2 Ink material selection and characterization | 29 |
| 3.3 Printing parameters optimization | 35 |

| | |
|---|-----|
| 3.4 Active micro-structured dielectric layer integration | 38 |
| 3.5 Finite-Element Modeling for microcylinder dielectric layer | 39 |
| 3.6 M2A3DNC pressure sensor characterization | 43 |
| 3.7 In-situ characterization of the sensors | 50 |
| 3.8 Summary | 54 |
| 3.9 Materials and Methods | 55 |
| Chapter IV. A Self-powered Triboelectric MXene-based 3D-printed Wearable Physiological | |
| Biosignal Sensing System for On-demand, Wireless, and Real-time Health Monitoring..... | |
| 4.1 Overview | 58 |
| 4.2 High-performance MXene ink for additive manufacturing | 62 |
| 4.3 Wearable MXene-based triboelectric nanogenerator (M-TENG)..... | 73 |
| 4.4 Wearable MXene-based pressure sensor (M-PS)..... | 82 |
| 4.5 <i>In-situ</i> demonstration of the wearable MXene-based self-powered physiological signal sensing system (MSP ² S ³) | 88 |
| 4.6 Summary | 94 |
| 4.7 Materials and methods | 94 |
| Chapter V. Conclusion..... | 99 |
| Bibliography | 103 |

LIST OF FIGURES

| | |
|--|----|
| Figure 1-1. Diagram of different physiological signals can be measured on human body at different locations..... | 1 |
| Figure 2-1. Illustration figure about the pneumatic printing process and key printing parameters..... | 6 |
| Figure 2-2. (a) The force element analysis inside the dispensing nozzle. (b) The cross-section view of differential ring element..... | 7 |
| Figure 2-3. Viscosity plotted as a function of shear rate for the 3D printable MXene ink with different concentrations..... | 11 |
| Figure 2-4. The fitting curve of the power index measured from rheometer in terms of the ink concentration..... | 12 |
| Figure 2-5. The fitting curve of the flow index measured from rheometer in terms of the ink concentration..... | 13 |
| Figure 2-6. The optical image of different printing result..... | 15 |
| Figure 2-7. The flow behavior inside a circular pipe for laminar flow and turbulent flow..... | 16 |
| Figure 2-8. The number of uniform and non-uniform data under different Reynold number..... | 17 |
| Figure 2-9. The possibility of the occurrence of uniform printing features and ununiform printing features in terms of the Reynold number..... | 18 |
| Figure 2-10. The printing result under different cases..... | 20 |

| | |
|--|----|
| Figure 2-11. The optical microscope image for the uniform printing line and stretched curvy printing lines..... | 21 |
| Figure 2-12. The number of continuous and non-continuous data under different normalized extrusion diameter..... | 22 |
| Figure 2-13. The possibility of the occurrence of uniform printing features and ununiform printing features in terms of the normalized extrusion diameter..... | 23 |
| Figure 2-14. The flow chart for the generation of our physics guided machine learning model..... | 25 |
| Figure 3-1. Photograph and the schematic of the exploded view of the M2A3DNC pressure sensor for multiple physiological signals monitoring..... | 30 |
| Figure 3-2. Rheology property of ink materials and electrical property of CNT+PDMS..... | 33 |
| Figure 3-3. Electrical conductivity of CNT+PDMS composite with different CNT content ranging from 0 – 12wt%..... | 34 |
| Figure 3-4. Nyquist plot of 3wt% CNT in PDMS composite..... | 35 |
| Figure 3-5. Nyquist plot of 12 wt% CNT in PDMS composite..... | 35 |
| Figure 3-6. A schematic representation of 3D printing of inks..... | 36 |
| Figure 3-7. Characterization and optimization of 3D printing parameters for homemade 12wt% CNT+PDMS ink..... | 38 |
| Figure 3-8. Layer schematics, optical microscope image and SEM image of the M2A3DNC sensors..... | 40 |

Figure 3-9. The Finite Element Modeling (FEM) Simulation, Z-axis displacement distribution under the applied stress of 0.5, 1, 2, 4 kPa for the planar structure dielectric.....42

Figure 3-10. The Finite Element Modeling (FEM) Simulation, Z-axis displacement distribution under the same applied stress of 0.5, 1, 2, 4 kPa for the microcylinder structure dielectric.....43

Figure 3-11. Comparison of the average Z-axis displacement of the microcylinder structured dielectric with planar dielectric.....43

Figure 3-12. Relationship of the capacitance change with the applied pressure from 0 – 4 kPa for the M2A3DNC sensors with and without micro-structure patterned dielectric layer.....45

Figure 3-13. Calculation model for bending strain.....45

Figure 3-14. The change in capacitance of the M2A3DNC sensors upon applying a 5.4% bending strain followed by the strain release of one representative device.....46

Figure 3-15. The photograph showing the pressure measurement by the application of a water droplet and the M2A3DNC pressure sensor's response to the induced pressure by the addition of three sequentially applied water droplets.....46

Figure 3-16. Droplet tests on other location.....48

Figure 3-17. Mechanical stability and reliability test of the M2A3DNC pressure sensors.....50

Figure 3-18. Cyclic test of the M2A3DNC pressure sensor with cyclic bending of 5.4% bending strain for 1,600 cycles, and the enlarged view of the marked region.....51

Figure 3-19. Optical image of the M2A3DNC pressure sensor on a human's belly and breathing waves at normal breathing, shallow breathing, and deep breathing states by the M2A3DNC pressure sensor.....52

Figure 3-20. Optical image of the M2A3DNC pressure sensor on a human's throat for acoustic vibration measurement and the M2A3DNC pressure sensor attached to the throat detects the acoustic vibrations of the larynx.....53

Figure 3-21. Optical image of the M2A3DNC pressure sensor on a human's wrist with an adjustable wrist band, and the schematic showing the conformal contact between the sensor and the epidermal contact on the skin.....53

Figure 3-22. The real-time transient pulse signal of the radial artery pulse wave measured with the M2A3DNC pressure sensor. Inset: the enlarged view for one pulse.....54

Figure 4-1. The concept of new generation of self-powered wearable sensing platform.....59

Figure 4-2. Schematic of the MXene-based self-powered physiological sensing system (MSP²S³).....62

Figure 4-3. System-level block diagram illustrating the MSP²S³'s different modules in modes one and two.....63

Figure 4-4. Schematic of chemical structure of 2D Ti₃C₂T_x MXene.....64

Figure 4-5. Triboelectric series of different materials.....65

Figure 4-6. The mechanism of using sedimentation to select different size of particles.....65

Figure 4-7. Illustration schematic for the home-modified large flake MXene ink for 3D printing.....66

Figure 4-8. XRD patterns of the synthesized MXene (Ti₃C₂T_x) and MAX phase (Ti₃AlC₂) powder.....67

| | |
|--|----|
| Figure 4-9. FTIR pattern of the synthesized MXene..... | 68 |
| Figure 4-10. Side-view SEM image of a MXene film showing the stack layers of nanosheets...69 | |
| Figure 4-11. Top-view SEM image of the large flake MXene of the 3D printable ink showing surface morphology and typical flake sizes.....70 | |
| Figure 4-12. Lateral size distribution of large MXene flakes.....71 | |
| Figure 4-13. Top-view SEM image (scale bar: 500 nm) of the small MXene flake.....71 | |
| Figure 4-14. Lateral size distribution of small MXene flakes.....72 | |
| Figure 4-15. The average (a) and mean (b) particle size values between small and large flakes.....72 | |
| Figure 4-16. The Ink conductivity during different preparation processes.....73 | |
| Figure 4-17. Rheological properties of 3D printable MXene ink with the storage and loss modulus plotted as a function of strain.....74 | |
| Figure 4-18. Printing optimization for the 3D printed MXene.....75 | |
| Figure 4-19. Working mechanism of power generation from M-TENG in contact-separation mode.....76 | |
| Figure 4-20. Working mechanism of power generation from the single-electrode M-TENG in bend-release mode.....77 | |
| Figure 4-21. Finite-element simulation of the potential distribution between the electrodes.....78 | |
| Figure 4-22. Simulation result for the potential difference over the change in the separation distance.....78 | |

| | |
|---|----|
| Figure 4-23. Output open circuit voltage of the M-TENG on various contact-separation frequencies when subjected to 19.9N..... | 79 |
| Figure 4-24. Output open circuit voltage of the M-TENG on various applied force when subjected to the operation frequency of $f=8\text{Hz}$ | 80 |
| Figure 4-25. Output voltage and current of the M-TENG generated on contact-separation frequency of $f=8\text{ Hz}$ with 19.9 N vertical force as a function of the load resistance..... | 81 |
| Figure 4-26. Instantiates output power of the M-TENG as a function of the load resistance..... | 81 |
| Figure 4-27. Schematic of the M-TENG with a rectifier circuit..... | 82 |
| Figure 4-28. The capacitor voltage characteristic curves for various capacitors charged through the M-TENG..... | 82 |
| Figure 4-29. The voltage output characteristics of the single electrode M-TENG in response to bending at different bending angles of 30° , 60° , and 90° using a linear motor..... | 83 |
| Figure 4-30. Voltage signal of the M-TENG in response to the continues bend of the finger, and elbow..... | 84 |
| Figure 4-31. Schematic of the M-PS..... | 85 |
| Figure 4-32. Characteristic curve for the M-pressure sensor, showing the relative change in capacitance with respect to different external pressures..... | 86 |
| Figure 4-33. The response time and relaxation time of the M-PS..... | 87 |
| Figure 4-34. The minute pressure response from applying droplets of water..... | 88 |

Figure 4-35. Left: The actual pulse signal collected from the M-pressure sensor. Right: The enlarged view for one specific pulse shows the three typical peaks of the wrist pulse.....88

Figure 4-36. The entire radial artery pressure waveform over the recording period of 45 seconds.....89

Figure 4-37. Circuit diagram for the MSP²S³ including the M-TENGs, power management circuitry, energy storing circuitry, data collection, and wireless data/power transmission modules.....91

Figure 4-38. The charging capability with different stacks of the M-TENG.....91

Figure 4-39. Optical image of the wearable MSP²S³. The inset “on” and “off” status of the LED, respectively, represent the valley and peak of the pulse signal detected by the MSP²S³ in mode one.....93

Figure 4-40. The real-time pulse data monitored using MSP²S³ in mode two, displayed in the customized App.....94

Figure 4-41. The enlarged view for one specific pulse, showing the typical three peaks of a single wrist RAP pulse.....95

ACKNOWLEDGEMENTS

I would like to express the deepest appreciation first to my committee chair, Professor Rahim Esfandyarpour, who has the attitude and the substance of a genius: he continually and convincingly conveyed a spirit of professional research throughout all the projects. Moreover, he understands the strong points and weak points for each student, helping them in the best way to learn and practice during a lot of innovative projects. Without his guidance and persistent help this dissertation would not have been possible.

Secondly, I would like to thank my committee members, Professor Ozdal Boyraz and Professor James Earthman, for their engagement in the advancement process in my Ph.D, and their precious advice and comments on my work.

In addition, a thank you to the chair of Materials Manufacturing and Technology program, Professor Lorenzo Valdevit, and Mark Banderas, who offer generous help and support from the beginning of my Ph.D. journey to the end.

At last, I would like to show my appreciation to my family, they are always the strongest support behind me, and my lovely lab mates, Taeil Kim, Prativa Das, Xiaochang Pei, and Sangwon Lee. All of you helped me a lot and accompanied me in the lab days and nights.

Lastly, I acknowledge the good fortune I have had during the past years, which has led me to meet some of the most fantastic people in the world. The new friends I have made, and the lessons learned continue to shape me and challenge me to do my best, inside and outside the lab.

Thank you very much!

非常感谢

VITA

Education

PhD in Engineering

September 2022

University of California, Irvine

Henry Samueli School of Engineering, Ph.D. in Materials Manufacturing and technology

Dissertation title: “Investigation of nanomaterials in the wearable electronics for health monitoring”

Advisor: Rahim Esfandyarpour

MS in Materials Engineering

University of Southern California

May 2017

BS in Materials Science and Engineering

June 2015

Wuhan University of Technology

Field of Study

Materials Manufacturing and Technology

Publications

1. **Yi, Q.**, Pei, X., Das, P., Qin, H., Lee, S. W., & Esfandyarpour, R. (2022). A self-powered triboelectric MXene-based 3D-printed wearable physiological biosignal sensing system for on-demand, wireless, and real-time health monitoring. *Nano Energy*, 101, 107511.
2. **Yi, Q.**, Najafikhoshnoo, S., Das, P., Noh, S., Hoang, E., Kim, T., & Esfandyarpour, R. (2022). All-3D-Printed, Flexible, and Hybrid Wearable Bioelectronic Tactile Sensors Using Biocompatible Nanocomposites for Health Monitoring. *Advanced Materials Technologies*, 7(5), 2101034.
3. Kim, T., **Yi, Q.**, Hoang, E., & Esfandyarpour, R. (2021). A 3D Printed Wearable Bioelectronic Patch for Multi-Sensing and In Situ Sweat Electrolyte Monitoring. *Advanced Materials Technologies*, 6(4), 2001021.

4. Das, P., Najafikhoshnoo, S., Tavares-Negrete, J., **Yi, Q.** & Esfandyarpour, R. A bioprinted in-vivo-mimicking 3D Lung-cancer-on-a-chip model to study the effect of external stimulus on the progress and inhibition of cancer metastasis, *Bioprinting*.
5. **Yi, Q.**, Ghandehari, A. & Esfandyarpour, R. Identification of the High-resolution 3D Printing Parameters based on Hybrid Physics Machine Learning. (In preparation for submission)
6. Liu, C., Zhao, B., Yang, J., **Yi, Q.**, Yao, Z., & Wu, J. (2020). Effects of brace-to-chord angle on capacity of multi-planar CHS X-joints under out-of-plane bending moments. *Engineering Structures*, 211, 110434.

ABSTRACT OF THE DISSERTATION

Investigation of nanomaterials in the wearable electronics for health monitoring

By

Qian Yi

Doctor of Philosophy in Engineering

University of California, Irvine, 2022

Professor Rahim Esfandyarpour, Chair

Physiological signals contain a wealth of personal health information which needs continuous monitoring for early detection of disease-induced physiological irregularities and can be established as a potential approach to developing personalized healthcare devices. It has a very urgent need for the development of a new generation of convenient, low cost, reliable, and stable wearable devices to keep track on such critical signals in case of the firsthand notice of any abnormal changes indicating the pathological changes in our body.

In the past decades, various categories of wearable sensors and platforms have been developed targeting the continuous, on-demand recordings of wide ranges of signals by different fabrication methods. Additive Manufacturing, also named three-dimensional (3D) printing has been developed in the past few years and received tremendous interest. It enables distributed manufacturing, allowing users to easily produce customized 3D objects in office or at home. In addition, additive manufacturing allows to reduce the production waste and energy consumption and possesses great potential to replace the conventional clean-room based fabrication technology with the potential of circumventing the requirement of sophisticated equipment and

highly trained specialists. Moreover, it offers a broader range of material selection, and allows customization of the desired ink for different application purposes.

Here, in this thesis, a series of application of 3D printing technology with different home developed nanomaterials in the development of the next generation of the wearable sensing platforms have been studied. In the first study, the physics behind the 3D printing process has been detailed analyzed and quantified the relationship between the different printing parameters to the final printed resolution. It helps the improvement of the reliability of the fabrication process by eliminating the unreliable trial and error method to optimize the required printing parameters. In the second study, an all-3D printed pressure sensor has been developed for radial artery pulse monitoring. Taking the advantaged of the material selection and preparation, all the ink shows good printability and strong mechanical properties. In addition, by carefully managing the printing path, direct 3D printed micropattern has been generated to enhance the sensor's performance for subtle pressure detection. At last, the proposed all 3D printed pressure sensor exhibits high sensitivity and good mechanical property while mounting on human body, achieving reliable real-time biosignal recording. In the last study, a novel integrated sensing platform has been proposed. A triboelectric nanogenerator has been introduced as the power supply to remove the need of the battery, eliminating the potential drawbacks of the battery charging, replacement, and safety concerns. By careful selection of the materials, the two-dimensional (2D) MXene turns out to be the proper material satisfied the requirement of the conductivity, triboelectricity, and the extrusion printing capability. The performance of the 3D printed triboelectric nanogenerator has been well characterized, and the integrated sensing platform with the pressure sensor has been successfully demonstrated. Furthermore, a LED illuminator and an NFC antenna are added to the entire sensing platform to enable the direct

visualization of the signal and real-time waveform recording. To the best of our knowledge, it is the first report of a wearable system for continuous and real-time physiological biosignals monitoring fully powered by human motion, signaling exciting potential in the field.

Chapter I. Introduction

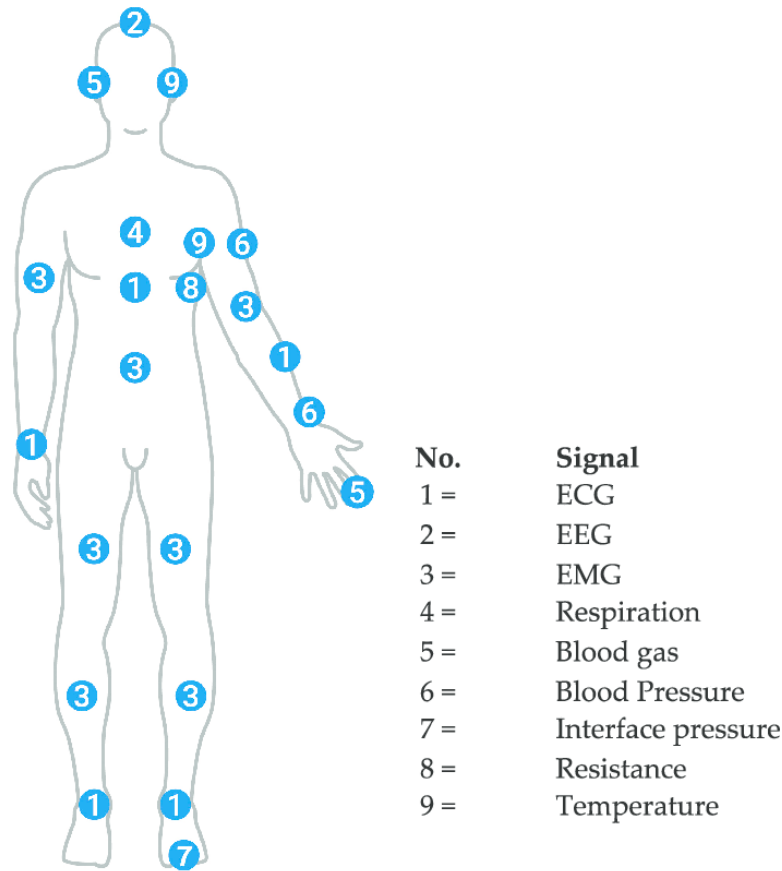


Figure 1-1. Diagram of different physiological signals can be measured on human body at different locations.

Physiological signals and biomarkers provide sufficient information for the functionality of different organs in human body. Electrocardiogram (ECG) can be recorded from chest and arm to check the heart's rhythm and electrical activity. Galvanic skin response (GSR) can be measured from fingers, allowing us to spot strong emotions. Cortisol can be detected by analyzing the concentration in body fluid and interprets the stress level of the person. The precise recording of all those biomarkers can greatly assist the early detection of disease-induced

physiological irregularities and can be established as a potential approach to developing personal healthcare devices.

The need for wearable sensors is growing due to the increased importance of in-situ real-time health monitoring.[1-5] It provides a non-invasive method to detect those physiological signals on different locations of human body. The number of wearable sensors users is approaching 900 million by 2021, and the expected market size is more than \$75 billion in 2025.[6] In recent years, there has been a great interest in developing innovative wearable technologies in healthcare research and development, since it provides a non-invasive access to interpret the health condition of our body.[7-9] The stability, balance, and equilibrium within the human body are critical for the normal function of human organ systems. The imbalance of electrolytes may lead to several diseases including but not limited to hypertension, heart failure, and kidney disease. Sweat electrolytes analysis, one of the noninvasively accessible biofluids, can provide valuable information about physiologically relevant quantities, and a combination of them can be employed for more comprehensive studies. On the other hand, wearable pressure sensors with intimate contact with the human skin possess great potential due to their capability to monitor physiological health signals in real-time. This monitoring includes wrist pulse, blood pressure, heart rate, and respiration rate for the early diagnosis of diseases.[10] Multiple research groups have developed innovative noninvasive wearable sensors for in-situ continuous monitoring of different parameters from the biofluids such as sweat and urine, or direct collecting the signal by intimate contact on the skin. For instance, a research group developed a wearable chemical barcode device to monitor sweat's pH level based on a microfluidics platform incorporating ionic liquid polymer gels[11], and another group developed a wearable microsensor array to monitor Zn, Cu, Cd, Pb, and Hg ions in both sweat and urine[12]. Moreover, recent research has

verified the relationship between the risk of COVID-19 infection and the human respiratory rate during the pandemic year of 2020. The reported model successfully identifies 20% of COVID-19 positive individuals in the validation dataset two days prior to symptom onset and the other 80% of COVID-19 positive cases three days prior.[13] Likewise, the early detection of abnormality in systolic blood pressure may reduce the probability of a rise in arterial wall stress and further control atherosclerosis development.[14]

Additive manufacturing (AM) technologies have developed rapidly in diverse fields among the existing manufacturing approaches over the past decade. With this technology, 3D structures can be directly created by laying off filaments sequentially along the model geometry, which enables the custom production of parts and prototypes accessible to the broad community. Various 3D printing technologies used in fabrication of an assortment of structures have been well reviewed and summarized,[15] namely light-based 3D printing[16-18], powder bed fusion-based methods[19], inkjet 3D printing[20], and extrusion-based printing[21, 22]. Among all of them extrusion-based printing is widely used due to its simple printing mechanism and low-cost of fabrication. The first step of this approach is the extrusion of materials through a nozzle with the aid of an applied air pressure. The extruded and deposited polymer then undergoes solidification through mechanisms such as crystallization, chain rearrangement, recovery of noncovalent bond, or chemical crosslinking. After the completion of a single layer, the extrusion head either moves up or the build platform moves down for the deposition of the next layer. Extrusion-based printing has been commercialized by several companies,[15] hence a wide selection of cheap 3D printers are available for researchers. This technology has also been adopted into various fields and has been used in several areas such as energy devices[23], biomaterials[24], and soft actuators[25, 26].

Comparing with the traditional molding or micro fabrication process, it provides a vast selection of the printing material, precise control over material deposition and structural modulation, and the potential of circumventing the need for traditionally required sophisticated equipment and highly trained specialists.

Combining all of the above-mentioned advantages, the 3D printing technology has a great potential to be applied to the wearable sensor industry, with a lower cost and an easier customized approach.

In this thesis, 3D printing technique has been explored from its basic physic principle to broad ranges of applications with different functioning materials. They are going to be described in detail in the flowing sections.

Chapter II. Predictive 3D printing resolution model for optimizing 3D printing parameters

2.1 Overview

As the 3D technology matures, the scope is expanding from simple bulky mechanical structures to miniaturized functional devices,[27] with increasing concerns of resolution control. However, few research works have been trying to understand and predict how the properties of printed ink and the printing parameters relate to the final form of the printed construct. For example, Bruneaux et al. (2008) showed how viscosity relates to shear rate inside the nozzle and how applied pressure relates to materials flow rate.[28] This work provides a basic understanding of a micro-extrusion bioprinting system. Cheng et al. (2008) focused on cell-laden hydrogel behavior and cell viability on extrusion.[29] This interesting work showed the relationship between cell viability and shear stress, but not the relationship between viscosity and resolution of the printed scaffold. Lee et al. (2015) developed a mathematical model on the relationship between printing speed and resolution; nonetheless, important parameters such as applied pressure and materials viscosity are not considered in the model.[30] Ratima et al. further developed the model, and showing the accuracy comparing with the experimental result.[31] However, all of the mathematical works developed so far still lack a feasible approach to determine the optimum resolution based on different printing parameters. Each time a feedstock formulation is changed, the exact printing conditions must be re-learned through time-consuming and labor-intensive trial-and-error work. Moreover, because of the large number of adjustable parameters for pneumatic extrusion printing, deep optimization by traditional brute-force methods is nearly impossible. To accelerate the process of learning optimal printing conditions and determine the

printing resolutions, a rational, easy-accessible, and accurate model should be developed to break the hindrance in the advancement of the AM application.

2.2 Investigation for pneumatic printing process

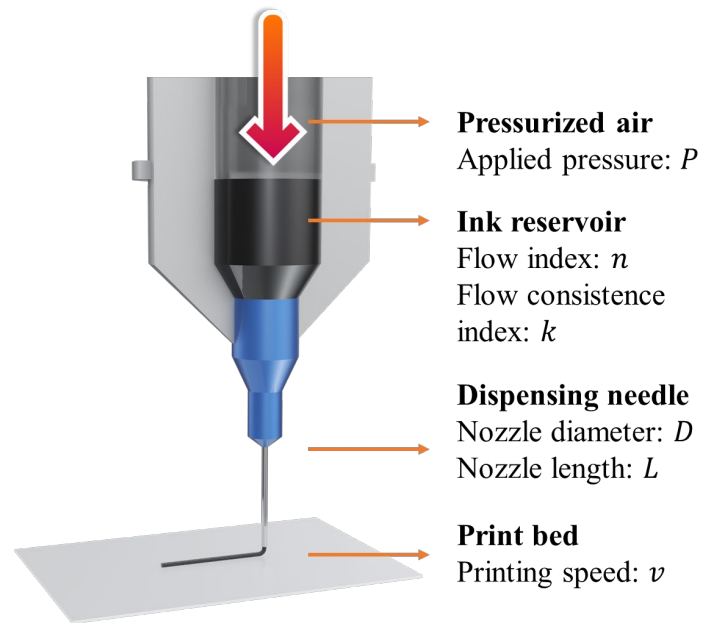


Figure 2-1. Illustration figure about the pneumatic printing process and key printing parameters

As stated previously, many parameters can be tuned to optimize a specific print. The awareness of how each parameter effect on the final printed strand should be first identified. The entire pneumatic 3D printing process can be split into two parts, material extrusion, and filament deposition, whereas the first part describes the ink flow throughout the needle, and the latter describes the material buildup on the printing stage.

As reported from previous research conducted by Khalil et al[32], there are 5 major controllable parameters in pneumatic printing system, which are,

- Extrusion pressure P (kPa)
- Ink rheology (Pa s), including the power index n and consistency index k

- Printing speed V_p (mm/s)
- Nozzle diameter D (mm)
- Nozzle length L (mm)

For the first part, the material extrusion part, it can be simplified into a model of flow inside the pipe cylinder.

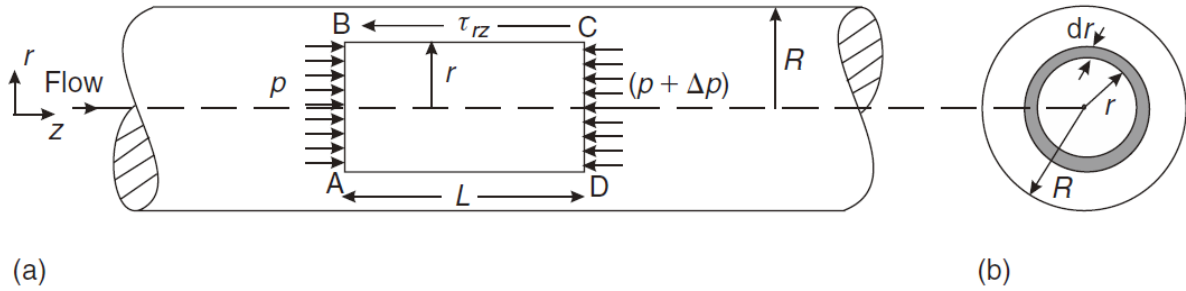


Figure 2-2. (a) The force element analysis inside the dispensing nozzle. (b) The cross-section view of differential ring element

A fully developed flow through the printing needles of a pneumatic printer holds similar flow characteristics to steady simple shear flow,[33] which is known as capillary or Poiseuille flow. The fully developed, steady flow of an incompressible ink in a needle of radius, R is shown in Figure 2-2. The flow is caused by the pressure difference (Δp) imposed across the two ends of the needle. Since there is no angular velocity and the ink is flowing at a steady state, the linear momentum balance (in the direction of flow, z) on a fluid element ABCD of radius r and length L , in terms of the shear stress (τ_{rz}), may be written as

$$p(\pi r^2) - (p + \Delta p)\pi r^2 = \tau_{rz}2\pi rL \quad (1)$$

Or,

$$\tau_{rz} = \left(\frac{-\Delta p}{L}\right) \frac{r}{2} \quad (2)$$

This shows the linear variation of the shear stress across the needle cross-section, increasing from zero at the axis of the needle to a maximum value at the needle. The shear stress (τ_{rz}) may then be evaluated in terms of the shear rate (γ) at the wall,

$$\gamma = -\frac{dV_z}{dr} \quad (3)$$

to yield steady shear rate data for a fluid. As summarized by previous reports about the materials applied for pneumatic 3D printing systems, the ink material with the non-Newtonian flow behavior benefits the printing process. Abdel-Hamid et al. (2006) reached to the conclusion that, the power-law model was the best fit for pneumatic printing viscoelastic material compared to the Bingham and Casson model.^[34] The relationship between shear stress (τ), shear rate (γ) can be described as follow:

$$\tau = k\gamma^n \quad (4)$$

Where, n is the power index, k is the flow consistency index or apparent viscosity, the z -direction flow velocity V_z at radius r can be expressed as:

$$dV_z = -\left\{\left(\frac{-\Delta p}{L}\right)\frac{1}{2k}\right\}^{1/n} r^{1/n} dr \quad (5)$$

Integrate with the respect of r to obtain the expression for the velocity distribution:

$$V_z = -\left(\frac{n}{n+1}\right)\left\{\left(\frac{-\Delta p}{L}\right)\frac{1}{2k}\right\}^{1/n} r^{(n+1)/n} + constant \quad (6)$$

At the walls (i.e., when $r = R$), the velocity V_z must be zero in order to satisfy the no-slip condition. Substituting the value $V_z = 0$, when $r = R$ in Eq.6,

$$constant = \left(\frac{n}{n+1}\right)\left\{\left(\frac{-\Delta p}{L}\right)\frac{1}{2k}\right\}^{1/n} R^{(n+1)/n} \quad (7)$$

The velocity distribution can be expressed as:

$$V_z = - \left(\frac{n}{n+1} \right) \left(\frac{-\Delta p R}{2kL} \right)^{1/n} R \left\{ 1 - \left(\frac{r}{R} \right)^{\frac{(n+1)}{n}} \right\} \quad (8)$$

The volume flow rate (Q) is used to represent the amount of the ink material extrusion rate, which may be given by:

$$dQ = 2\pi r V_z dr \quad (9)$$

And the total volumetric flow rate is obtained by integration over the cross-section of the needle as:

$$Q_{extrusion} = \int_0^R 2\pi r V_z dr \quad (10)$$

For the material buildup stage, the certain filament extruded from the printing needle, is laid on the printing stage by the controlled movement at a velocity v . Assuming the extruding filament is continuous through the extrusion and maintained circular shape after the extrusion,

$$Q_{printing} = \pi d^2 v / 4 \quad (11)$$

Where, d is the diameter of the printed filament, v is the moving speed. The volume is conservation throughout the entire printing process, $Q_{extrusion} = Q_{printing}$. As a result,

$$d = \sqrt{\left(\frac{n}{3n+1} \right) \left(\frac{D^3}{2vk^{1/n}} \right) \left(\frac{D\Delta p}{4L} \right)^{1/n}} \quad (12)$$

The width of the printed filament (resolution, d) could be determined by the other major printing parameters including extrusion pressure (Δp), stage moving speed (v), viscosity parameters (n , k), and the needle diameter (D). And these four major parameters are going to be used for the

modeling and experiments in the later sections. It is noteworthy to mention that other parameters including the needle length, needle angle, and the printing gap, they have the specific defined from the company or by the machine itself. And the parameters like the temperature, UV exposure etc. for the combined printing process are not considered in our study.

2.3 Determination of the viscoelastic behavior of the printed material

The investigation of the relationships between structural features of materials and their flow properties to achieve high structural fidelity of constructs is, to a great extent, a matter of rheology. The materials used in pneumatic printing are mainly viscoelastic and may exhibit thixotropy. This complex flow behavior enables the gel ink to behave as a fluid and to present the characteristics of a soft solid material, depending not only on the time scale that they are subjected to perturbations but also on their amplitude.

As shown in the previous equations, for non-Newtonian material for pneumatic printing, the viscosity is not a given fixed number. It usually shows a shear thinning behavior which the viscosity decreases under shear strain. Instead of a fixed given number, it represents by two parameters: n as power index, and k as flow consistency index, the relationship is defined as follow (Ostwald and de Waele power law):

$$\eta = k\gamma^{n-1} \quad (13)$$

And it can be further written in logarithmic form:

$$\log \eta = (n - 1) \log \gamma + \log k \quad (14)$$

Both indexes can be easily obtained from by linear fitting the data obtained from rheometer study. Most of the cases, the ink used for the pneumatic printing is composed of multimaterial, the function filler and the solvent, like CNT+PDMS for the electronic devices, and living cell+GelMA for the biomedical application, etc. In those cases, the viscosity is determined based on the specific

types of the material, and concentrations based on different ink components. Therefore, to achieve the tunability of the viscosity parameters, the relationship between the ink concentration for certain kind of material mixture should be developed. In this study, different concentrations of the conductive MXene ink have been prepared by evaporation or addition of the water solvent. All the viscosity plots have been characterized, and the corresponding viscosity indexes are obtained according to the concentration C.

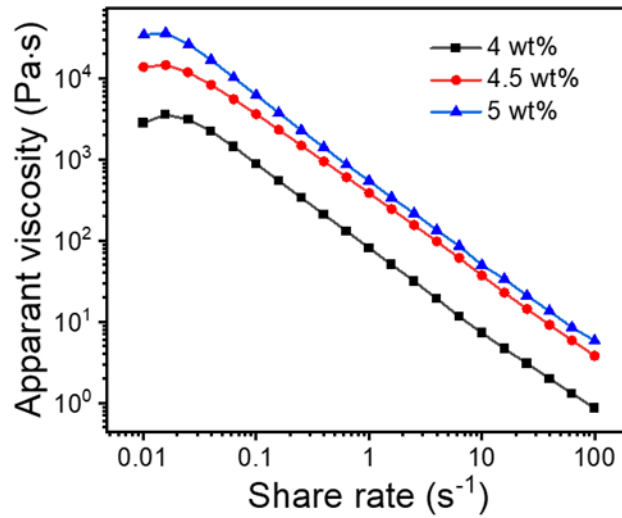


Figure 2-3. Viscosity plotted as a function of shear rate for the 3D printable MXene ink with different concentrations. The data followed the Ostwald-de Waele power law: $\eta = k\gamma^{n-1}$, where k and n are the flow index and shear-thinning power index, respectively.

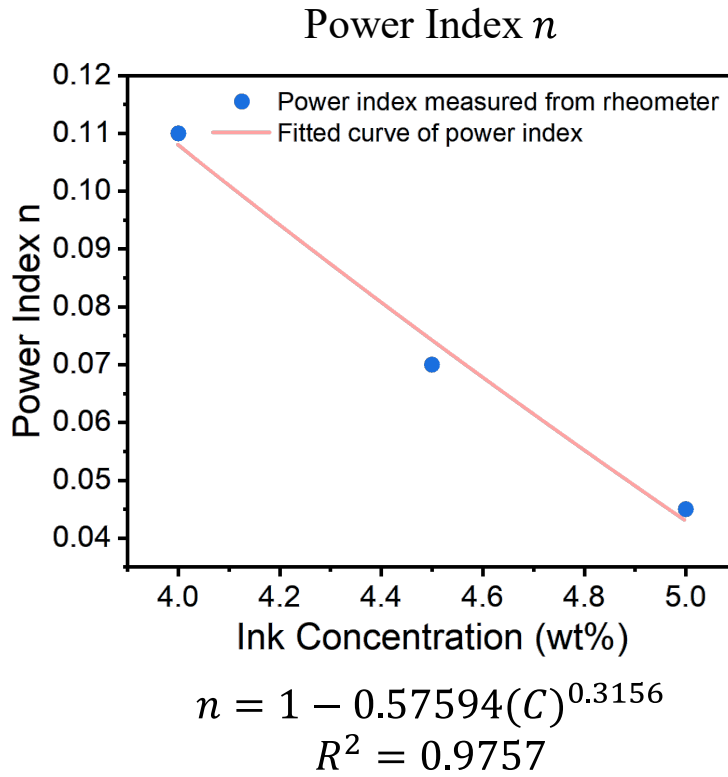
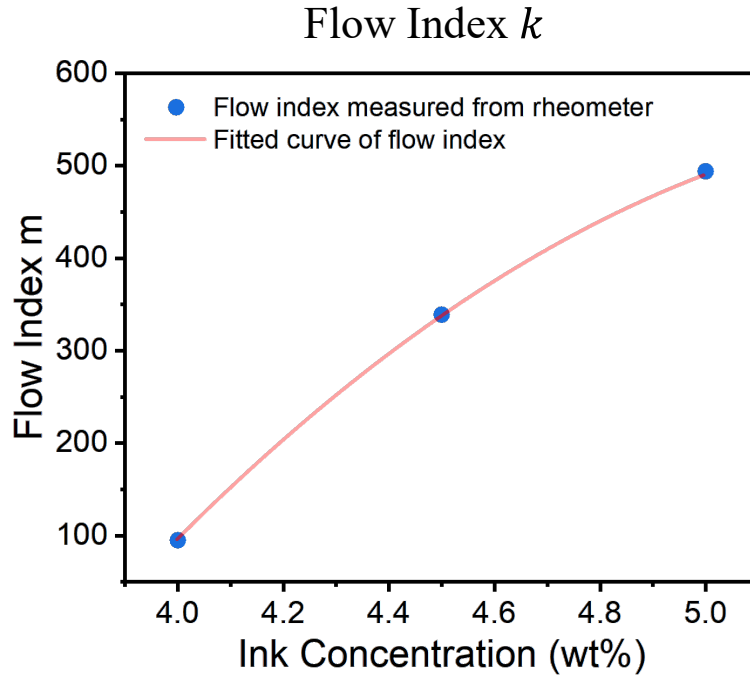


Figure 2-4. The fitting curve of the power index measured from rheometer in terms of the ink concentration



$$m = -172C^2 + 1980C - 5010$$

$$R^2 = 0.99955$$

Figure 2-5. The fitting curve of the flow index measured from rheometer in terms of the ink concentration

As shown in Figure 2-4 & 2-5, the power index (n) and flow index (k) followed the governing equation of $n = 1 - 0.57594(C)^{0.3156}$ and $k = -172C^2 + 1980C - 5010$, respectively, depending on the ink concentration, allowing a flexible viscosity adjustment according to different extrusion systems. The concentration C and the corresponding viscosity indexes relationship are going to be applied in the model to show the viscosity tunability and for the following optimization process. It is worth to mention that for a different ink materials with different concentrations, their own viscosity parameters' relationship with the ink concentrations should be experimentally defined first and can be used for the further calculation.

2.4 Boundary limitation

In order to optimize the printing parameters for a precise control of the printing resolution. It is important to understand all the possible printing result from different printing parameters. In this experiment, single line filaments are printed under 800 random generated data points from different combination of printing parameters, including extrusion pressure P , print bed moving speed v , Mxene ink concentration C , and different dispensing nozzle D . The printing result can be categorized into 5 different categories, non-extrudable (labeled as “0”), discrete printing (labeled as “1”), ununiform printing (labeled as “2”), uniform printing (labeled as “3”), overflowed printing (labeled as “4”). The representatives are shown in Figure 2-6. Non-extrudable printing and discrete printing, they cannot provide a continuous extruded filament, which is not favored for the 3D printing process. Ununiform printing has a very thin filament width, but due to the large standard deviation, it is not suitable for the precision control of the extrude filament. The overflowed printing result in the excess deposition of the ink material, it is neither controllable nor optimized in resolution. Therefore, only the uniform printing is the target printing type for the parameter’s optimization. It must be clearly selected out of all the printing condition. So, boundary conditions need to be considered for the optimization process.

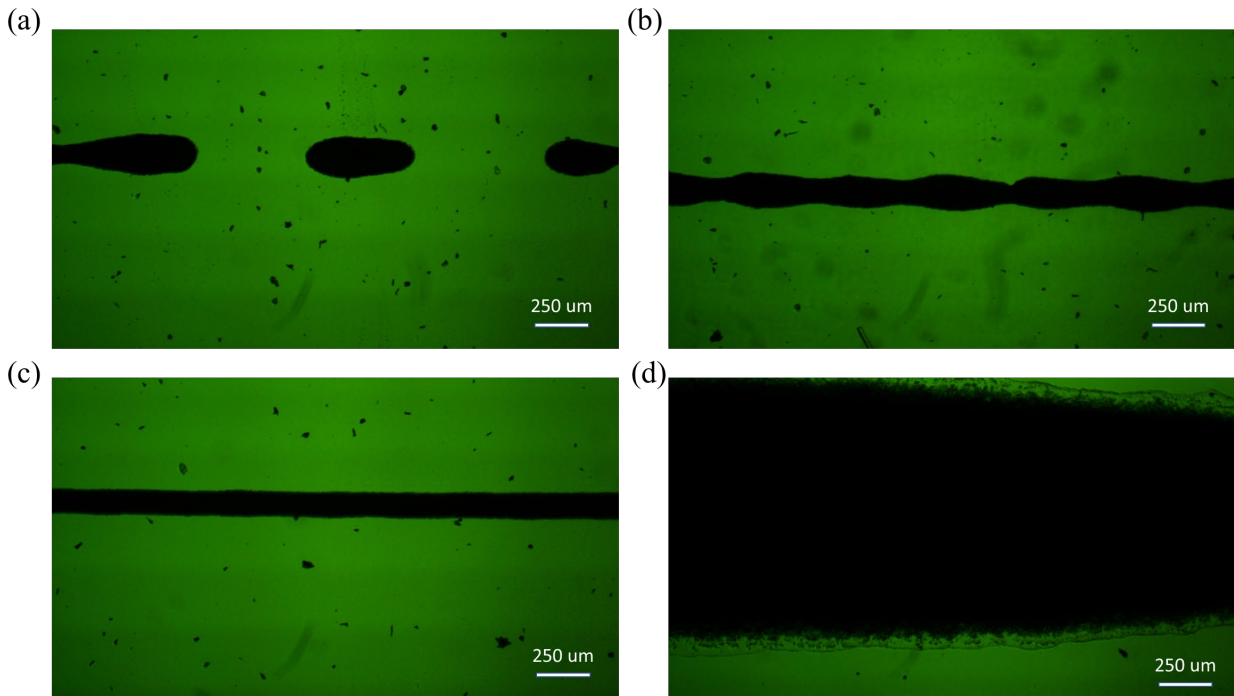


Figure 2-6. The optical image of different printing result. (a) discrete printing, (b) ununiform printing, (c) uniform printing, (d) Overflowed printing

As described in the previous section, the entire printing process can be separated into two different parts, ink extrusion and filament deposition. Each part of the process plays an important role in the finalized printing pattern. These assumptions, applications and effects on the printed filament are well examined.

2.4.1 Ink extrusion

Considering the structure of the extrusion system, the most critical part for the extruded filament formation is the dispensing nozzle. According to the geometry of the nozzle, the entire extrusion process can be simplified into the similar proposed physics model of the flow behavior inside a circular pipe.

The ink is going to exhibit flow behavior during the extrusion. The flow behavior can be characterized into different conditions: Laminar flow, transition flow (something between the laminar and turbulent) and turbulent flow. Regarding the initial condition of the flow velocity, diameter of the cylinder, and the material property, the flow type can be classified into three different categories: Laminar flow, turbulent flow, and transition flow (something between the laminar and turbulent). The flow behavior can be directly visualized in the Fig 2-8. The laminar flow provides a homogenous flow, where the stress and velocity distribution remain constant at different places in the tube. However, for the turbulent flow, it shows a random stress distribution. It results in an uncontrollable extrusion, which is impropriated to apply on the optimization of the printing parameters for the precise control of printing resolution.

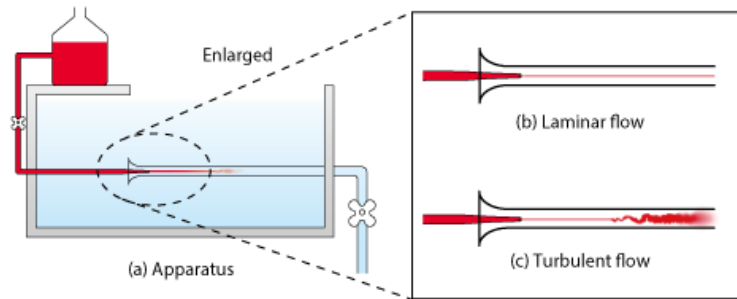


Figure 2-7. The flow behavior inside a circular pipe for laminar flow and turbulent flow

The gold standard to evaluate the flow type is Reynold number, it can be defined as:

$$Re = \frac{\text{Inertial forces}}{\text{Viscous forces}} = \frac{V_{avg}L}{\nu} = \frac{\rho V_{avg}L}{\mu} \quad (15)$$

Where,

V_{avg} is the averaged flow speed

L is a characteristic linear dimension

ν is the kinetic viscosity

μ is the dynamic viscosity

However, this is the relationship for the Newtonian flow, which means that the viscosity behavior is constant under different applied stress conditions. But for our case, the ink we are using they all follow the non-Newtonian behavior. So, this equation cannot be directly applied. According to the proposed idea from [35], they proposed a revised form of the Reynold number for Non-Newtonian material, by replacing the constant viscosity parameter into the expression of power index and flow index,

$$Re_{non} = \frac{\rho V^{2-n} D^n}{8^{n-1} k} \quad (16)$$

The Non-Newtonian Reynold number has been calculated for all the printed data points, and further classified by the uniform printing result and ununiform printing result.

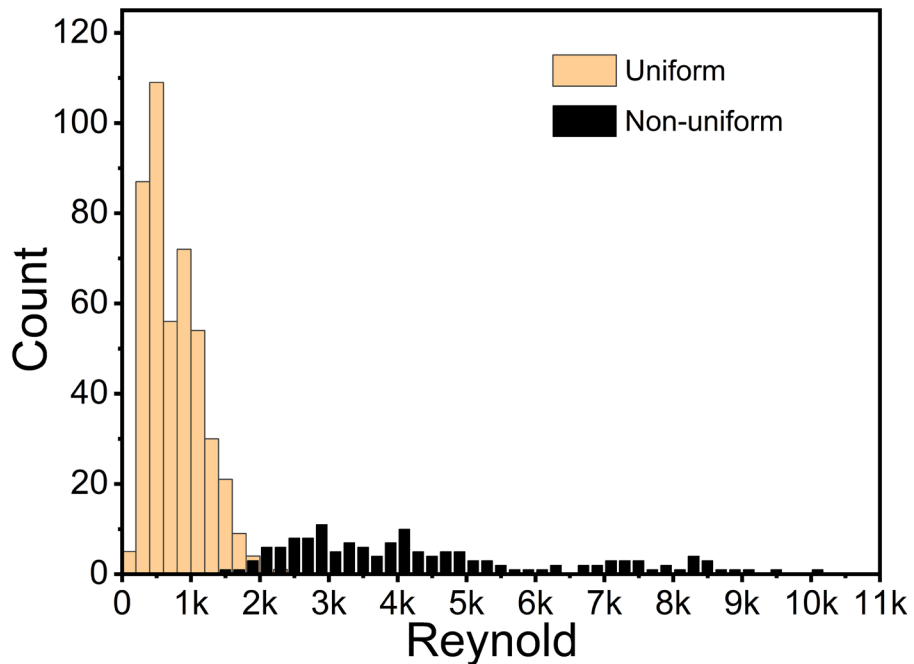


Figure 2-8. The number of uniform and non-uniform data under different Reynold number.

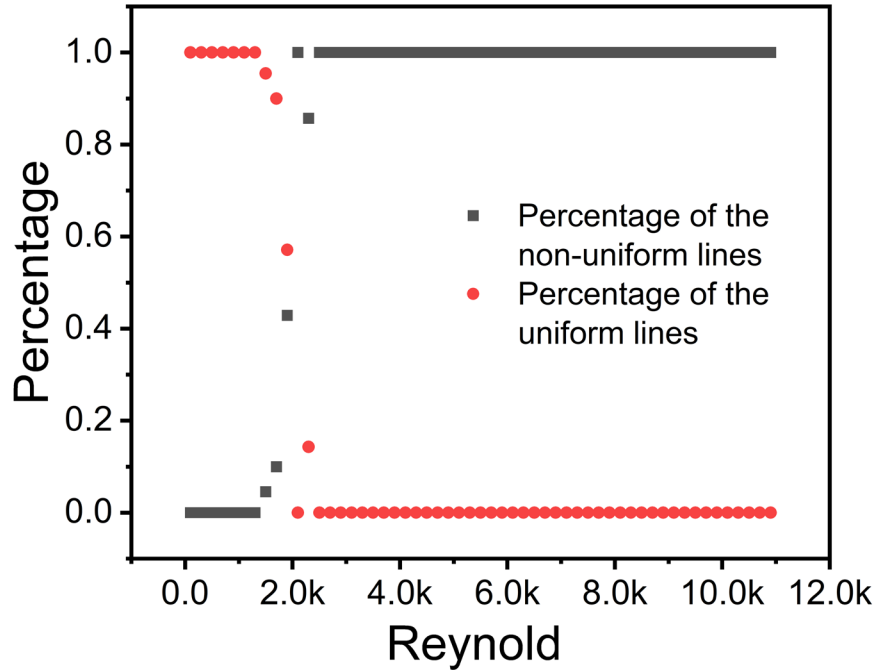


Figure 2-9. The possibility of the occurrence of uniform printing features and ununiform printing features in terms of the Reynold number.

All the result has been transformed into the uniform printing probability versus the Reynold number, and a uniform printing is labeled as printability of 1, where the other printing results are labeled as printability of 0. From the Figure 2-8 & 2-9, it is clearly observed that the plot has been separated into 3 parts. The first part with relative low Reynold number shows a higher probability (printability of 1) for the uniform printing result. Whereas the region with high Reynold number exhibits higher chances to result in a uniform printing result (printability of 0). There is a transition region between those two regions (in this region, the profitability of 0 and 1

exists under the same range of Reynold number). Within this transition region, the probability is decreasing from high to low when the Reynold number increases from low to high. Similar to the case from the observation of the flow type for Newtonian liquid. The flow is showing a laminar flow with a low Reynold number. It turns into transition flow with the increase of the Reynold number, and finally becomes the turbulent flow. Our statistical analysis could also be explained by the same scenario. In the extrusion part, lower Reynold number gives a steadier flow, which is easier for the uniform extrusion and filament deposition. As the Reynold number increases, the uncontrollable flow behavior occurs, and causes larger deviation in the extruded material, leading to an ununiform printing result.

2.4.2 Filament deposition

After the material has been homogeneously extruded from the dispensing nozzle, the next step is to lay the filament onto the print bed. The competing mechanism during this process is the extrusion speed (V_N), and the print bed moving speed (v), which is also called printing speed.

Considering the volume conservation, the amount of the material extruded throughout the nozzle is going to be the same as the amount of the material laid on to the print bed. Assuming the deposited filament still maintains the circular structure, which is commonly observed in a lot of the 3D printing process[36].

However, there are certain concerns for the different between the extrusion speed and the printing speed. According to the paper presented by Khalili et., al.[32] (shown in the Figure 2-10), the printing velocity (v) should be the same as the extrusion velocity (V_N). If the printing speed (v) is greater than the extrusion speed (V_N), the fabricated strut diameter is usually smaller than the nozzle diameter, which will easily introduce the stretch of the printed filament and cause

non-uniformity. If the printing speed (v) is smaller than extrusion speed (V_N), the fabricated strut diameter is usually greater than the nozzle diameter, which is not good in optimizing the printing width. As a result, to maintain the high resolution and good uniformity, the expected extrusion diameter (d) should be in the same range as the nozzle diameter (D), and the printing speed (v) should be in the same range as the extrusion speed (V_N). The same scenario was also observed in our study, the stretched filament and the uniform filament is shown in the Figure 2-11.

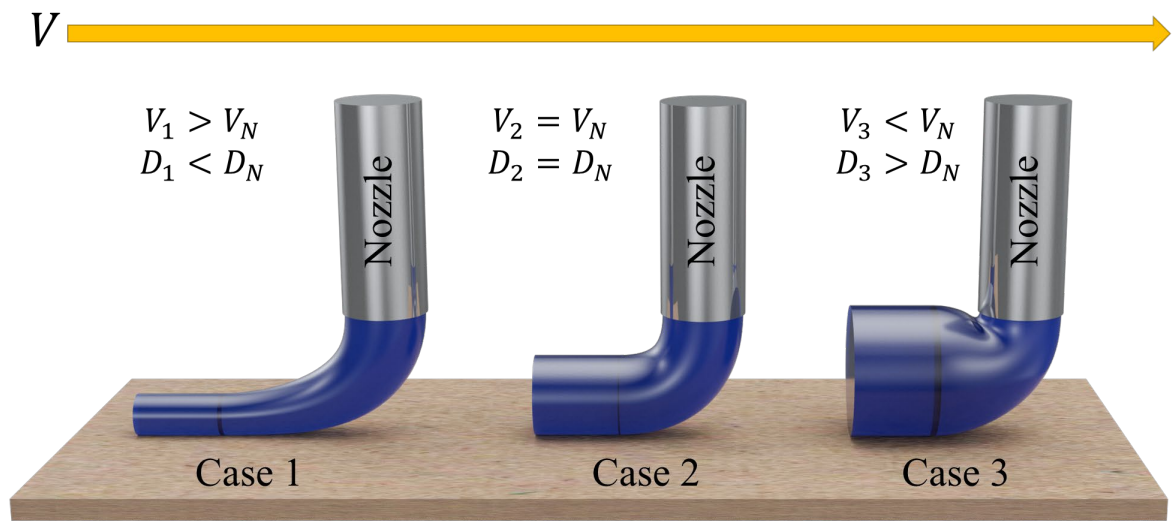


Figure 2-10. The printing result under different cases. Case 1: The moving speed is larger than the extrusion speed, the printed diameter is smaller than the nozzle diameter. Case 2: The moving speed is similar than the extrusion speed, the printed diameter is similar than the nozzle diameter. Case 3: The moving speed is smaller than the extrusion speed, the printed diameter is larger than the nozzle diameter.

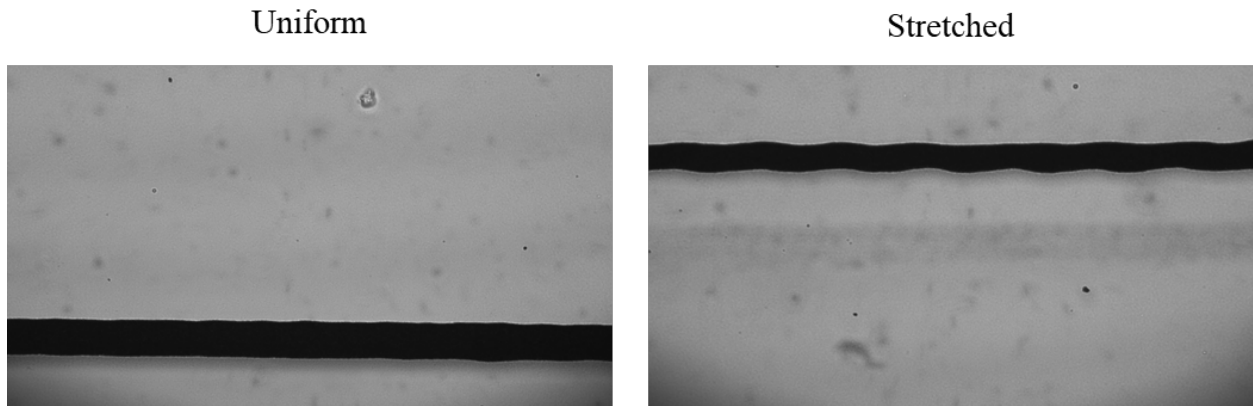


Figure 2-11. The optical microscope image for the uniform printing line and stretched curvy printing lines.

Similar statistical analysis has been studied for the filament deposition part. Because of the observation boundary between the case 2 and case 3 is not clear to identify, and the main concern for this project is to optimize the printing resolution, so we classify the printing data into two different categories: continuous printing including the uniform printing (class 3) and overflowed printing (class 4), and non-continuous printing, including discrete printing (class 1) and ununiform printing (class 2). As shown in the Figure 2-12, all the data points obtained experimentally has been plotted as histogram. The normalized variance in the printed filament width and the nozzle diameter is labeled as X-axis, and the counts of continuous printing and non-continuous printing is labeled as Y-axis for the statistical analysis, each bin size is 0.02.

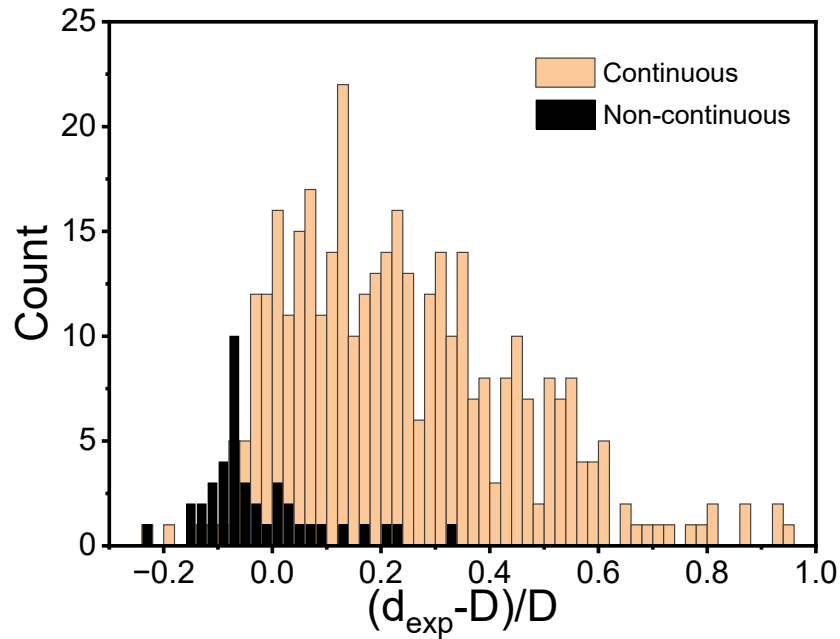


Figure 2-12. The number of continuous and non-continuous data under different normalized extrusion diameter.

To further visualize the relationship of the printing condition to the normalized extrusion diameter, the static histogram has been plotted as the percentage of uniform printing. As shown in the Figure 2-13, when the normalized extrusion diameter is increased, the possibility of the occurrence of discrete printing features and ununiform printing features decreased. When the normalized printing diameter is exceeding -3%, the possibility of having uniform printing result is larger than 80%, which we can consider as a reliable printing result. So, the -3% is set as the boundary conditions for the filament deposition for a reliable uniform printing result.

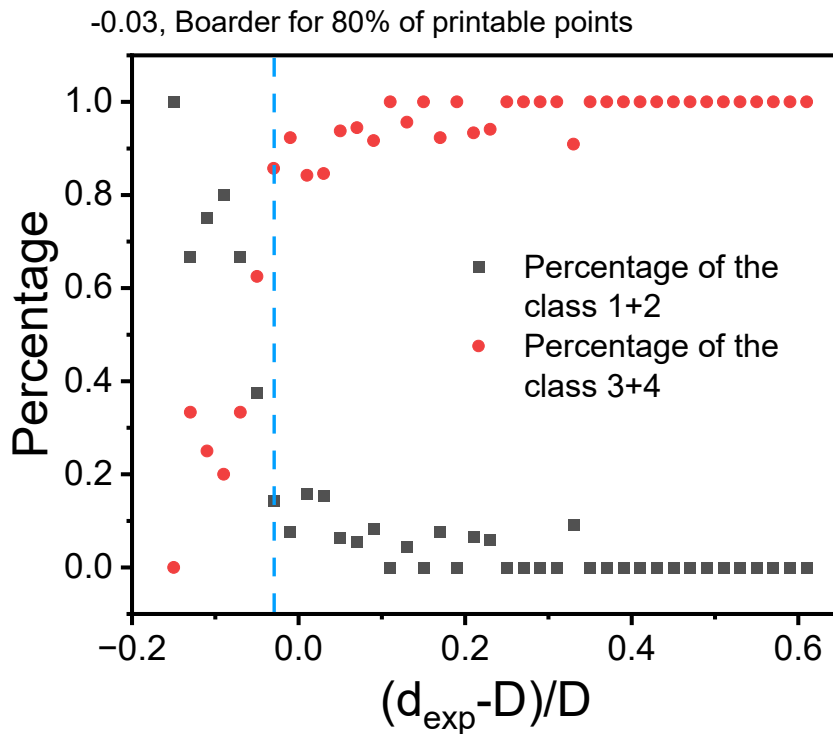


Figure 2-13. The possibility of the occurrence of uniform printing features and ununiform printing features in terms of the normalized extrusion diameter.

It is worth to mention that the boundary between the uniform printing (class 3) and overflowed printing (class 4) is not taken into account in our study. The first reason is that the transition between these two categories is not as clear as the transition between ununiform curvy printing and the uniform printing. The second and the most important reason is because this work is mainly focused on the optimization of the printed resolution, which means that under the uniform continuous printing conditions, the smaller printed resolution is preferred. In the future plan, the controllable printing condition is going to be considered. The upper boundary for the normalized extrusion diameter is going to be detailed analyzed in those cases.

2.5 Future work: Physic-guided machine learning model

The physic based mathematic model has been developed in the previous section, and the boundaries are clearly considered in different stages of the pneumatic printing process. However, all of the conclusions are drawing from the ideal cases. For instance, during the extrusion process, the friction between the inner wall of the nozzle and the material has been ignored. It can be disregarded when the material has a very low viscosity like water, but when it comes to more viscos materials like gels and pastes. In those cases, the stress distribution is not a linear function regarding to the distance to the center. In addition, the gap between the dispensing nozzle and the printing stage, and the partially clogging of the nozzle also influences the final printed filament.

In order to eliminate the inevitable non-ideality error, these hard to mathematically modelled factors should also be taken into account. Physics-guided machine learning turns out to be the ideal solution for our problem. Training the physics derivative mathematical model and the boundary conditions with the mass printed data, the actual hidden relationship between the printing parameters to the printing resolution can be discovered.

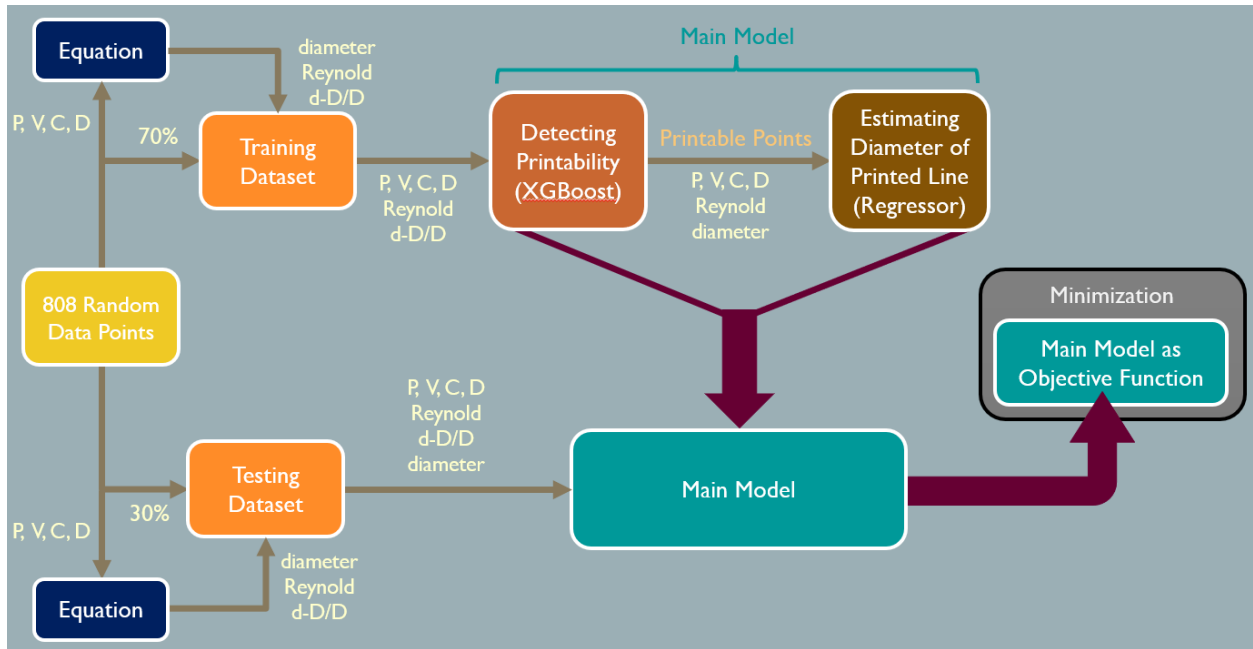


Figure 2-14. The flow chart for the generation of our physics guided machine learning model

The flow chart of the generation of our physics guided machine learning model is depicted in the Figure 2-14. 808 random data points were first been randomly selected into two categories, the training dataset with 70% of the data, and the testing dataset with the rest 30%. The data was first feed into the physics-induced equation, with the extrusion and deposition boundary conditions. All those features together with the classified printed result were delivered to the main model, the determination of the printability and the estimation of the line diameter were conducted in this step, and further got trained from the dataset. After the model training was completed, the test dataset is going to be used for the evaluation of the accuracy of the printing result prediction. The reliability of the prediction will be performed at last to verify the accuracy of the predicting physic-guided ML model.

Chapter III. All-3D-printed, flexible, and hybrid wearable bioelectronic sensors using biocompatible nanocomposites for health monitoring

3.1 Overview

Wearable biosensors have received tremendous interest and increasing demand over the past decade in many existing and emerging applications, including personalized healthcare, electronic skin and textiles, soft robotics, human/machine interfaces, and drug delivery.[37, 38] Flexible wearable pressure sensors with intimate contact with the human skin possess great potential due to their capability to monitor physiological health signals in real-time. This monitoring includes wrist pulse, blood pressure, heart rate, and respiration rate for the early diagnosis of diseases.[39] Over the past few years, several classes of pressure sensors, such as capacitive,[40-44] resistive/piezoresistive,[45-49] piezoelectric,[50-54], and triboelectric[55-58] have attracted considerable attention for healthcare application. Among all of these, the capacitive-based pressure sensor offers high sensitivity[59, 60], low power consumption[61], simplified design[62], high flexibility[39], higher immunity to environmental noises[63], and a fast response time[64] to external stimuli, revealing the potential of being used to supervise vital human signals and can further find application in providing real-time personalized medicine. On the other hand, recent efforts have led to notable developments in manufacturing techniques, which pave the approaches to fabricate complex electronics and soft sensors in more convenient, rapid, and lower-cost methods than traditional clean-room-based microfabrication techniques.[65-67] Over the years, various printing techniques such as inkjet printing,[68, 69] screen printing,[70, 71] fused depositing modeling,[72] stereolithography printing, and extrusion-based mold printing[73] have been applied to fabricate wearable sensors. However, to achieve reliable and precise monitoring of physiological signals, high sensitivity, mechanical

flexibility, and reliability are required. To address the sensitivity requirement, efforts have been made to micro-engineer the active layer, which deforms under pressure and dictates changes in the output signal of pressure sensors. In recent years, a wide range of designs has been developed, including micro-domes,[74] micro-pyramids, lines or micro-ridges,[75] papillae,[76] micro-spheres,[77] micro-pores,[78] and micro-cylinders,[75] each offering different advantages for a particular application. Nevertheless, to date, the majority of pressure sensors containing a micro-engineered active layer were either been fabricated by complicated and lengthy microfabrication steps in cleanrooms or by mold-casting techniques.[79] These complicated processes hindered rapid innovation and the broad selection of functional materials.

The innovation in the 3D printing provides an entirely new approach for the fabrication of wearable pressure sensor in an easier design manner with less material consumption. Emon et al. (2019) proposed 3D printing of CNT and ionic liquid-based polymer (1-ethyl-3-methylimidazolium tetrafluoroborate, TangoPlus) and find application in pressure sensors [80]. However, without microengineering of the dielectric layer and exploration of the limit of detection (LOD), the sensor's capability for subtle signal detection on human skin was restricted. Another group, Zhenhua et al. (2020), proposed the 3D printing of a sensitive pressure sensor by the introduction of a porous structure made by printing of CNTs and fumed silica nanoparticles (SiNPs).[81] By the incorporation of the structured active layer, the deformation according to the external pressure was amplified and improved their sensitivity. However, in terms of the entire device construction, it required incorporation of the several fabrication methods together and assembly processes which raised the complexity of the sensor fabrication and the thick sensor design may limit their wearability applications. Similarly, Tiancheng et al. (2021) reported 3D printed microstructures with gold nanoparticles for the flexible pressure sensors, for electronic

skins.[82] In their work, by taking the advantage of an expensive stereolithography (SLA) printer, they employed a bottom-up fabrication process, and a microcylinder structure of flexible substrate was fabricated. Yet, not enough effort was spared in the combination of the structured layer formation and device fabrication to enable rapid, consistent, and cost-effective fabrication of sensitive, reliable, stable, and cost-effective wearable and flexible bioelectronic wearable sensors. Even though the 3D printing technique has been recently employed for sensor fabrication, it still lacks the proper adaption in multi-material and multi-layer 3D printed flexible sensors with the micro-engineered layer for subtle physiological signal detection on the human body.

In this section, we are reporting a novel multi-material and multilayer all-3D-printed nanocomposite-based (M2A3DNC) microengineered flexible wearable pressure sensor for recording sensitive and multiple physiological signals for real-time human health monitoring. Our approach provides a novel path to develop a highly compressible microstructured device with high sensitivity and low detection limit in a rapid, and cost-effective manner during consecutive multilayer printing, using a single tool. By applying the intrinsic property of extrusion printing, the hemicylinder microstructure dielectric layer was directly 3D printed by managing the moving path of the nozzle, with air voids formation after assembling to enhance the compressibility of the active layer, as it is shown in Figure 3-1.

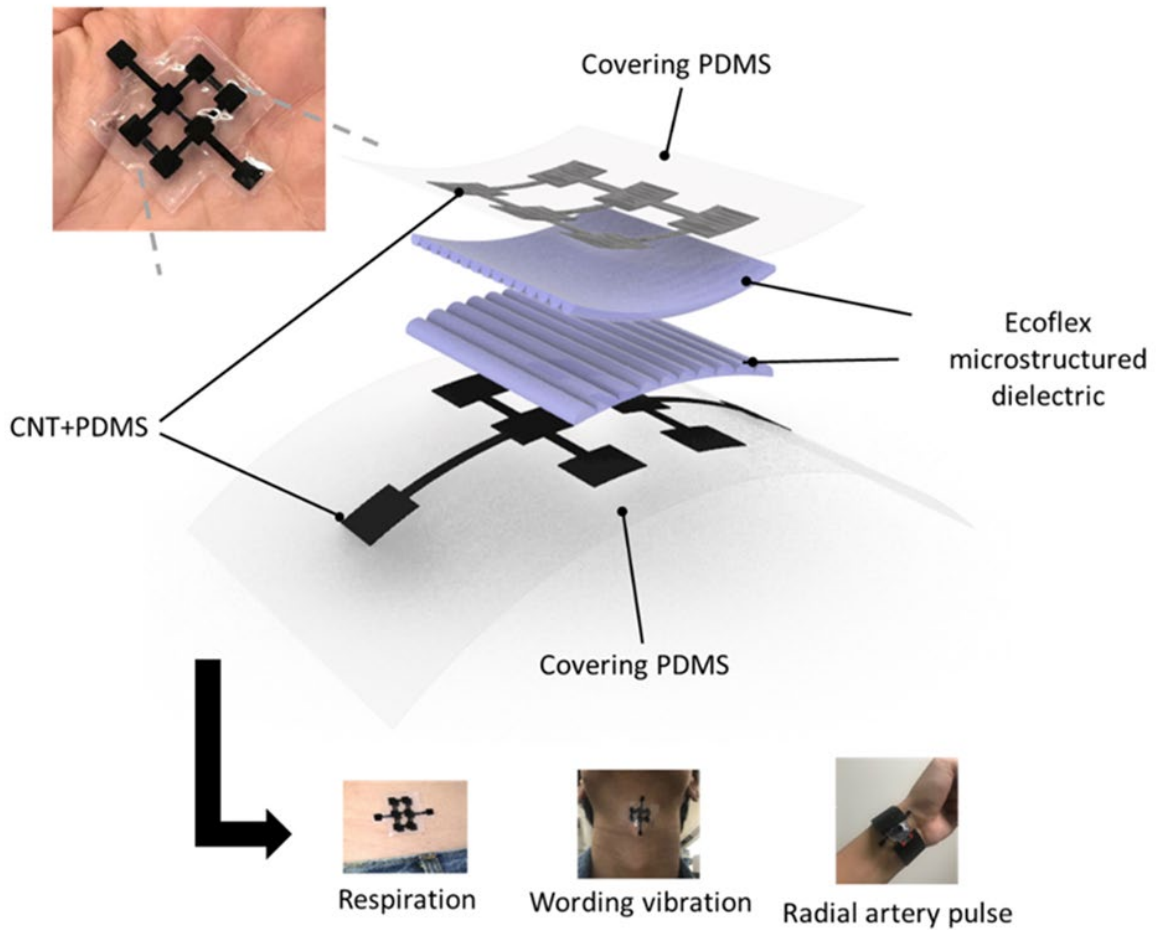


Figure 3-1. Photograph and the schematic of the exploded view of the M2A3DNC pressure sensor for multiple physiological signals monitoring.

3.2 Ink material selection and characterization

The proposed M2A3DNC capacitive pressure sensors are composed of three different materials that are designed sequentially as the support layer, conductive layer, and dielectric layer. During the fabrication of the wearable sensor, strain changes on the human body needed to be taken into consideration. For example, the wrist pulse causes strain change within 2% [83], the human respiration causes a strain range from 0.05%-10% [84], and the bending behaviors of the finger, elbow, and foot cause a strain change achieving >40% [85]. Thus, a material with a wider linear

range is required. PDMS is one of the skin-like materials[86], has a matching modulus (0.57-3.7MPa)[87] with the skin to maintain the intimate skin-sensor contact and good mechanical stretchability (~80%)[88] responding to the strains that occurred on the skin, which is favored for direct contact supporting layer. Carbon nanotubes (CNTs) have great potential for applications in flexible electronics due to their high electrical conductivity, mechanical flexibility, thermal stability, and high aspect ratio.[89] Combining with the flexible PDMS elastomer, the composite material of CNT+PDMS exhibits excellent electromechanical, mechanical, electrical, and biocompatible properties, which are the requirements for the conductive layer in a capacitive pressure sensor. Ecoflex 00-30 was chosen as the dielectric layer material due to its biocompatibility and lower modulus (0.125 MPa)[90] compared to PDMS (0.57-3.7 MPa)[91], thus favored flexibility of the device during application of the external force and enhance the sensitivity of the device.

To test the functionality and capability for extrusion printing, the selected ink materials were first characterized by rheology tests. Viscosity is the most important rheological parameter for defining the flow. It describes the resistance to flow and is given as a relationship of stress to the deformation rate. During the extrusion, the applied deformation is high, approximated shear rate induced by the printing nozzle leads to the order of $10^2 - 10^3 \text{ s}^{-1}$.[92] Within this region, the sample needs very low viscosity to allow the easy flow of the ink. At zero shear rate, the viscosity needs to be high so that the ink maintains the intended print shape after being extruded out from the nozzle. As shown in Figure 3-2 d-f, for the support layer, an optimum mixture of Sylgard 184 and SE 1700 with the respective curing agents was mixed in the ratio of 1:2 to achieve a decrease in viscosity from 10^4 to $10^1 \text{ Pa}\cdot\text{s}$ along with an increase in share rate from 10^{-2} to 10^{-2} s^{-1} (compared to SE1700) (Figure 3-2d). At the same time, the conducting layer of CNT +

PDMS showed a reduction in viscosity from 10^5 to 10^1 Pa·s by the increase in shear rate from 10^2 to 10^3 s⁻¹, as presented in Figure 3-2e. All printing inks exhibited typical shear-thinning behavior with non-Newtonian property, which is beneficial and expected for 3D extrusion printing.

Characterization of the electrical property of the CNT+PDMS composites under different concentrations was also carefully studied for the conducting panel application in the capacitive-based pressure sensors. The electrical conductivity of the composite was calculated by the following formula:

$$\sigma = \frac{l}{S \times R_0} \quad (17)$$

Where S is the sample of the cross-sectional area (m²), l is the length of the sample (m), R_0 is the sample resistance (Ω), and σ is the sample conductivity (S/m). $N=3$ for each patch of the ink, and the averages were shown as the representatives. Figure 3-3 shows the relationship between the electrical conductivity of CNT+PDMS and the weight ratio of CNT in PDMS. Initially, a sharp increase between 0-3 wt%, followed by a gradual increase from 3 to 12 wt% in electrical conductivity was observed with the increase in a weight ratio of CNT to PDMS from 0 – 12 wt%. In this CNT+PDMS composite, made by the dry blending method, the sharp increase corresponded to the percolation threshold, which was 1-3 wt%, and consistent with reported literature (close to 2wt%).[93]

Electric impedance spectroscopy (EIS) was employed to capture the frequency responses of CNT+PDMS in different weight ratios. The Nyquist plot is an important method for extracting impedance elements from the frequency response. Figure 3-4 showed a semicircle curve which is the frequency response of the 3wt% CNT+PDMS composites. This demonstrates that the parallel

of electrical resistance and capacitance can represent the electrical equivalent circuit at the 3 wt% CNT+PDMS composites. With the increase in the weight ratio to 12 wt% CNT in PDMS, as presented in Figure 3-5, the sample frequency response changes from a parabola to a vertical line. These observations indicate that the frequency response can be regarded as electrical resistances the conducting material of the capacitor, poor conductivity, and parasitic capacitance could interfere with the actual signal from the deformation of pressure, which can deteriorate the sensitivity and may cause fluctuation in the baseline. Therefore, it was concluded that for our application, 12wt% CNT+PDMS was the ideal composition and superior to 3wt% CNT+PDMS for fabrication of the conducting layer in the proposed pressure sensor.

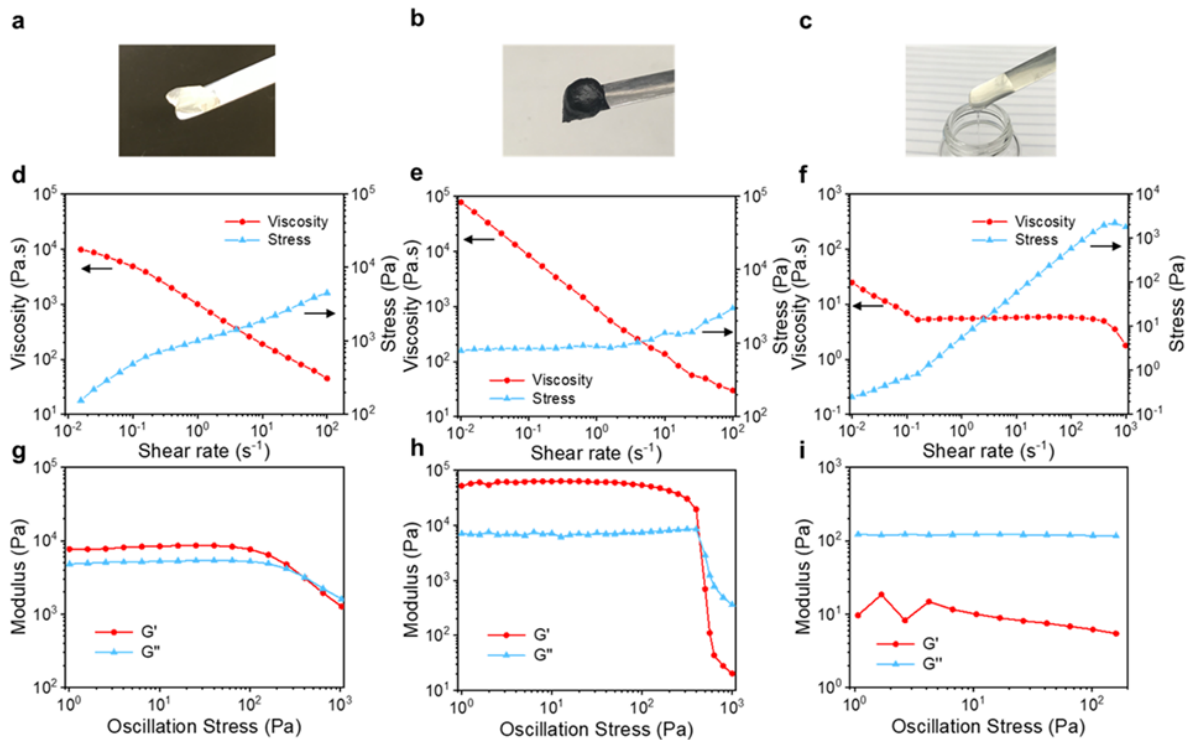


Figure 3-2. Rheology property of ink materials and electrical property of CNT+PDMS. a-c) Optical image of Sylgard184+SE1700 ink, 12wt% CNT+PDMS ink, and Ecoflex 00-30 ink. d-f)

Viscosity plotted as a function of shear rates for Sylgard184+SE1700 ink, 12wt% CNT+PDMS ink, and Ecoflex 00-30 ink. g-i) Viscoelastic properties of Sylgard184+SE1700 ink, 12wt% CNT+PDMS ink, and Ecoflex 00-30 ink.

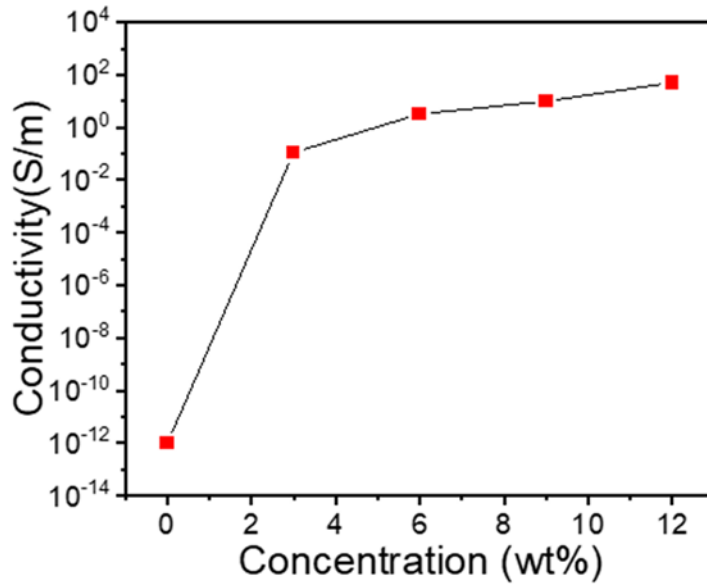


Figure 3-3. Electrical conductivity of CNT+PDMS composite with different CNT content ranging from 0 – 12wt%.

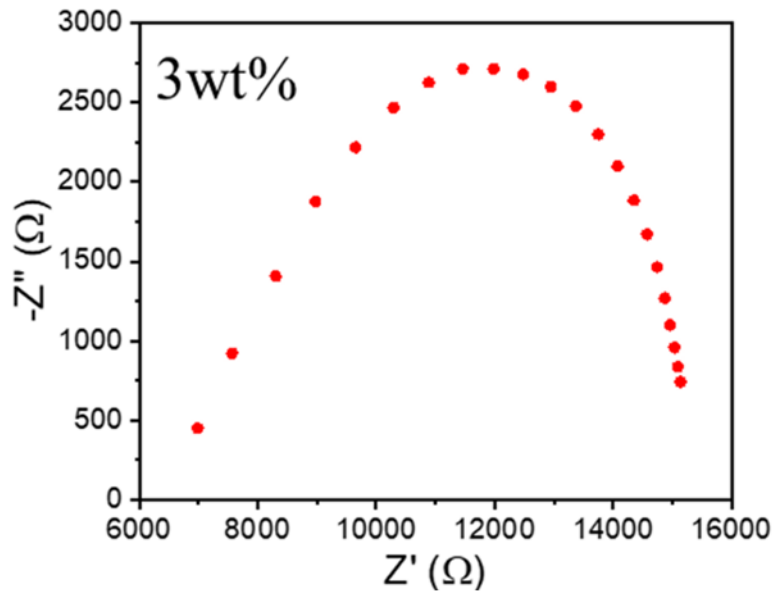


Figure 3-4. Nyquist plot of 3wt% CNT in PDMS composite.

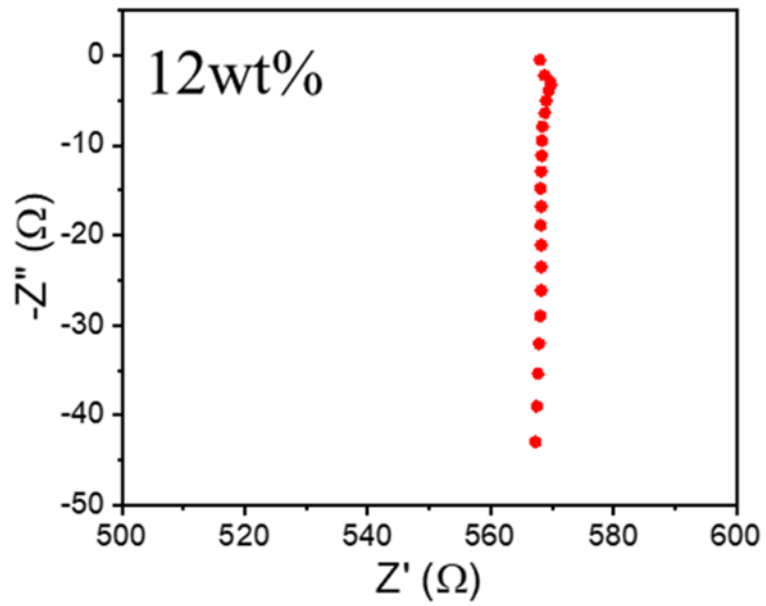


Figure 3-5. Nyquist plot of 12 wt% CNT in PDMS composite.

3.3 Printing parameters optimization

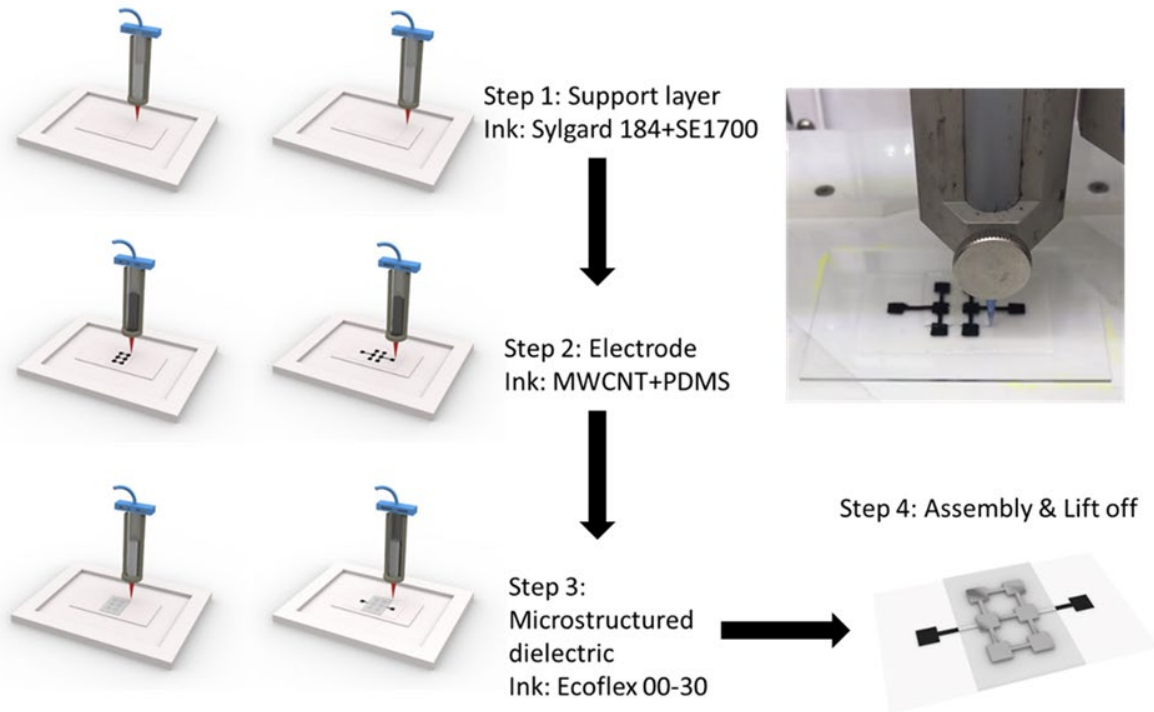


Figure 3-6. A schematic representation of 3D printing of inks (step 1: direct printing of the PDMS Sylgard184+SE1700 supporting layer, step 2: direct printing of the MWCNT+PDMS conductive layer, step 3: direct printing of the Ecoflex 00-30 microstructured dielectric) to construct a multilayered structure of M2A3DNC sensors followed by its assembly (step 4: Assembly of two pieces of the capacitor and detached by the release of the pre-coated PVA in a hot water bath). Inset: Optical image of 3D printing of hemicylinder patterned Ecoflex 00-30 dielectric layer.

The fabrication process was performed by our uniquely optimized multi-material 3D printing approach, as described in Figure 3-6. All layers of the M2A3DNC pressure sensors were fabricated by extrusion 3D printing consecutively. During the extrusion 3D printing process, several printing parameters take important roles in the resolution and quality of the printed

pattern, such as controlled extrusion pressure, print head moving speed, nozzle size, etc. For example, the material extrusion speed is related to the nozzle size and applied pressure, and the deposition is related to the extrusion speed and printing speed. For a low extrusion speed and high printing speed, the material will be stretched, and the width of the deposited line will be lower. But in some cases, the material deposition could be interrupted. Contrariwise, for high extrusion speed and low printing speed, the filament width will be higher.[33] To investigate the influences on resolution and material property by different parameters, we performed the characterization experiments by studying the influences of different extrusion nozzles (inner diameter of 510 μm , 340 μm , and 260 μm), the printing speed (range from 1-7 mm/s) of the tip, and the extrusion pressure (range from 90 to 120 kPa) on the continuity, thickness, width and electrical resistivity of 3D printed conductive lines (n=3) for our homemade 12 wt% CNT+PDMS ink (Figure 3-7). Conditions that failed to generate a continuous filament were not included in the plots, and the standard deviation within the same batch of samples was illustrated in error bars (n=3). As shown in Figure 3-7 a-f, the resolution of the printed features was improved by reducing the diameter of the printing nozzle. For the smallest nozzle with an inner diameter of 0.26 mm, the minimum achievable thickness was reduced from 120 μm to 46 μm by increasing the printing speed from 2 mm/s to 7 mm/s and reducing the extrusion pressure from 120 kPa to 90 kPa (Figure 3-7 c). Similarly, the minimum obtained width was reduced from 407 μm to 106 μm (Figure 3-7 f), and the resistivity decreased from 0.114 Ωm to 0.019 Ωm (Figure 3i). Thus, the optimized printing conditions were obtained for the printing speed of 7 mm/s, and

extrusion pressure of 90 kPa, with the inner nozzle diameter of 0.26 mm, and these parameters were maintained for printing the conductive layers during sensor fabrication.

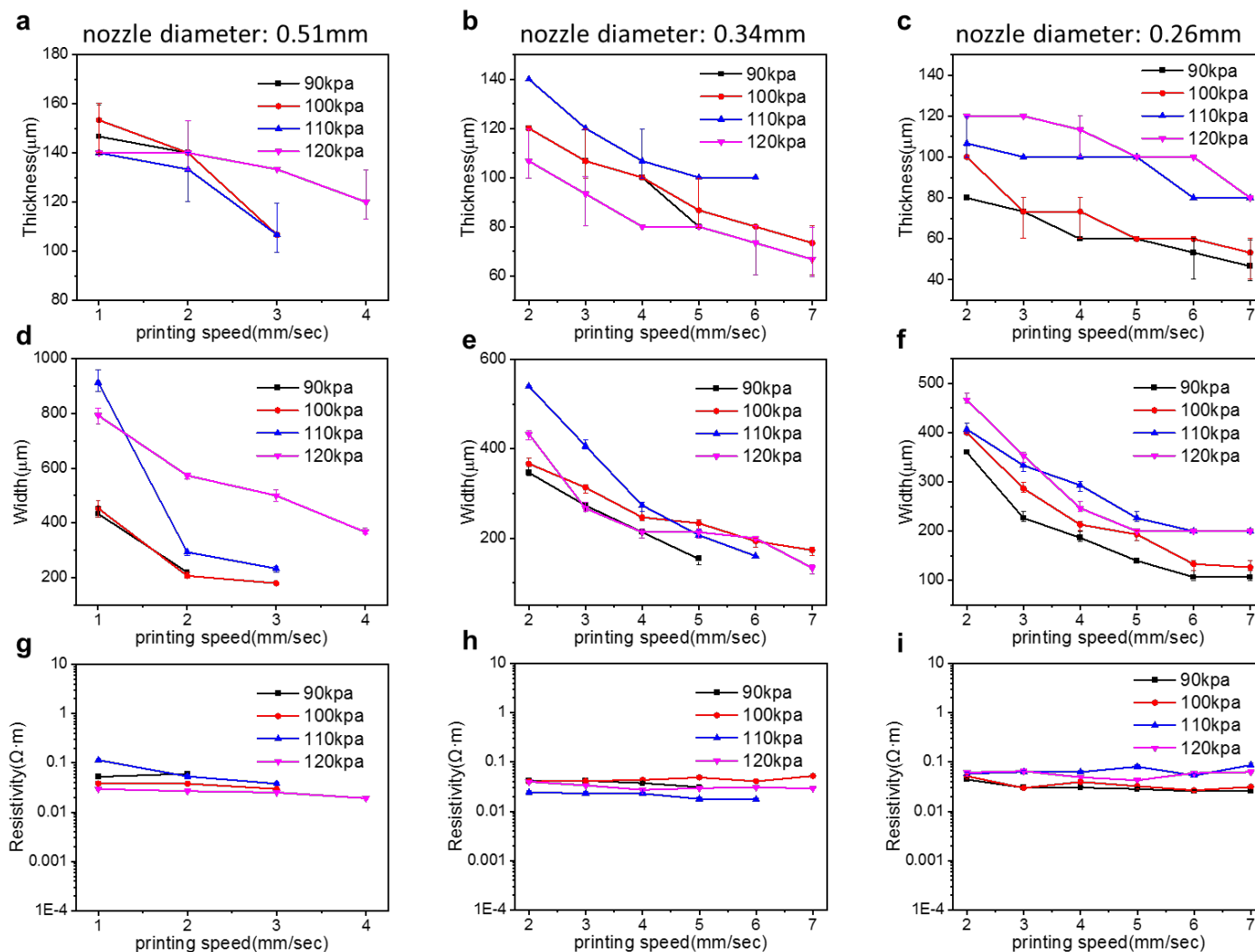


Figure 3-7. Characterization and optimization of 3D printing parameters for homemade 12wt% CNT+PDMS ink (n=3). Error bars represent standard deviation. a-c) The thickness of 3D printed conductive lines as a function of printing speed from 1 mm/s to 7 mm/s with different printing nozzles with an inner diameter of 0.51 mm, 0.34 mm, 0.26 mm at various extrusion pressures of 90 kPa, 100 kPa, 110 kPa, 120 kPa. d-f) The width of 3D printed conductive lines as a function of printing speed from 1 mm/s to 7 mm/s with different printing nozzles with an inner diameter

of 0.51 mm, 0.34 mm, 0.26 mm at various extrusion pressures of 90 kPa, 100 kPa, 110 kPa, 120 kPa. g-i) The resistivity of 3D printed conductive lines as a function of printing speed from 1 mm/s to 7 mm/s at various extrusion pressures of 90 kPa, 100 kPa, 110 kPa, 120 kPa.

3.4 Active micro-structured dielectric layer integration

As mentioned before, for subtle physiological signal collection, it is crucial to enhance wearable sensors' sensitivity for precise signal recognition. Here, a direct 3D printed active micro-structured dielectric layer, a porous grid-shape patterned dielectric, was implemented to enhance the sensor's sensitivity during the consecutive multi-material multilayer printing process. In brief, two hemicylinder shapes patterned Ecoflex layers are 3D printed by the printer setting of rectilinear infill pattern, 50 % infill intensity, and speed of 10 mm/s. The final micro-structured porous grid-shape dielectric layer was then achieved by the assembly of two perpendicularly 3D printed hemicylinder structured layers, Figure 3-8. The 3D printed hemicylinder micro-structured dielectric layer was characterized by the optical microscope and the Scanning Electron Microscopy (SEM) imaging. Figure 3-8 right-top shows the cross-sectional image of a sample prepared for SEM imaging. The layers from top to bottom were (i) hemicylinder structured dielectric (Ecoflex 00-30 with the peak thickness of $\sim 71 \mu\text{m}$ and pitch thickness of $52 \mu\text{m}$, with a pitch gap of $\sim 400 \mu\text{m}$), (ii) CNT+PDMS (sensor's conductive layer), (iii) PDMS (sensor's encapsulating layer), all 3D printed on a double-sided tape attached to a glass substrate to prepare the sample for the cross-sectional SEM imaging. It was clear to notice that the Ecoflex layer showed a repeated semicylinder structure while directly printed by the extrusion 3D printing method. In the optical microscope image of the Ecoflex dielectric layer as presented in Figure 3-8 right-bottom, the air voids were formed between the gaps of the perpendicularly

aligned hemicylinder pattern, which could benefit the structure deformation upon pressure and enhance the sensor's sensitivity as expected.

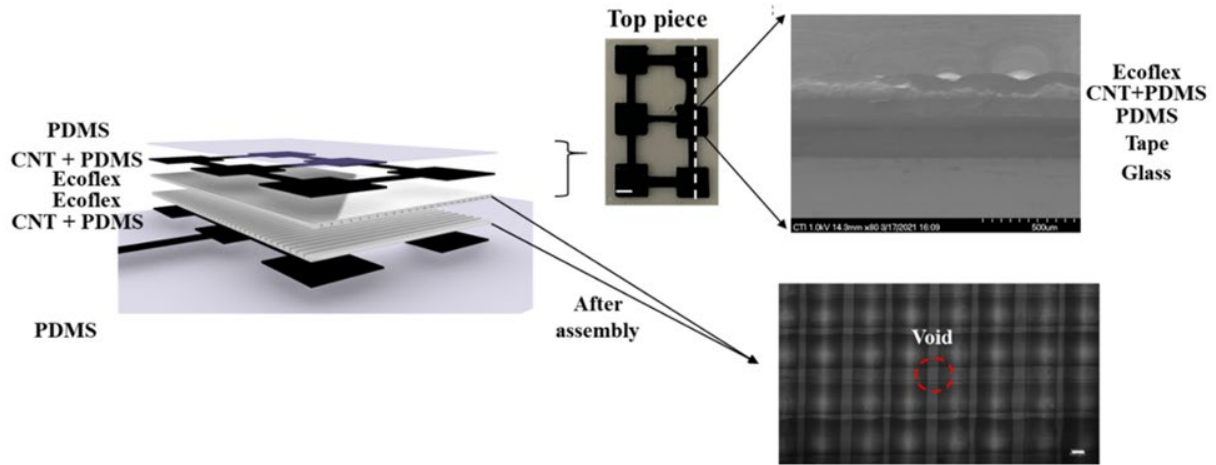


Figure 3-8. Layer schematics, optical microscope image and SEM image of the M2A3DNC sensors.

3.5 Finite-Element Modeling for microcylinder dielectric layer

To theoretically investigate the performance enhancement upon incorporating the 3D printed micro grid pattern, COMSOL finite element modeling (FEM) simulation investigation was conducted (Figure 3-9). The sensing mechanism of parallel plate capacitive pressure sensors can be explained by equation 2 as presented below.

$$C = \epsilon A/d \quad (17)$$

Where " ϵ " is the permittivity, " A " is the area of overlap of the two parallel plates, and " d " is the separation between the plates. The equation indicates that the change in the capacitance is directly related to the deformation in the middle dielectric layer. Therefore, building a solid comprehension of the dielectric layer deformation can help to interpret the sensing performance of the M2A3DNC pressure sensors with and without the micro-structured grid-shape patterned

dielectric layer. Here, the displacement distribution in a planar dielectric layer and a micropatterned dielectric layer under the same constant applied pressure was modeled and examined. The material properties and dimensions in the model were adjusted to be the same as the used materials of the sensors and the obtained geometry from the SEM image (Figure 3-8) of the dielectric layer. In the model, the pressure was uniformly applied in the vertical direction on the top surface for the magnitudes of 0.5, 1, 2, and 4 kPa, respectively, to figure out the deformation of the active layer in the small pressure regime, which is similar to the range of pressure on human skin, as shown in Figure 3-9 & 3-10. By comparing the average Z-axis displacement (Figure 3-11), the planar dielectric layer showed a displacement of $\sim 15 \mu\text{m}$, whereas the micropatterned dielectric layer showed a displacement of $108 \mu\text{m}$ under the same applied pressure of 4 kPa. A 7-fold higher magnitude in the deformation for the microstructured dielectric layer was observed when compared to the planar dielectric layer, thus indicating higher compressibility of the dielectric layer and higher expected sensitivity while applied for fabrication of pressure sensor. It is worth mentioning that in simulations, only the ideal condition was considered, i.e., the initial compression between the different micro-structured layers, implemented from the pressure of the material mass and the assembly process, was not reflected. Yet, it provides significant enhancement in compressibility of the dielectric layer deformation, which subsequently results in high sensitivity of the sensors and confirms the validity of the micro-engineered structure formation during multi-layer 3D printing.

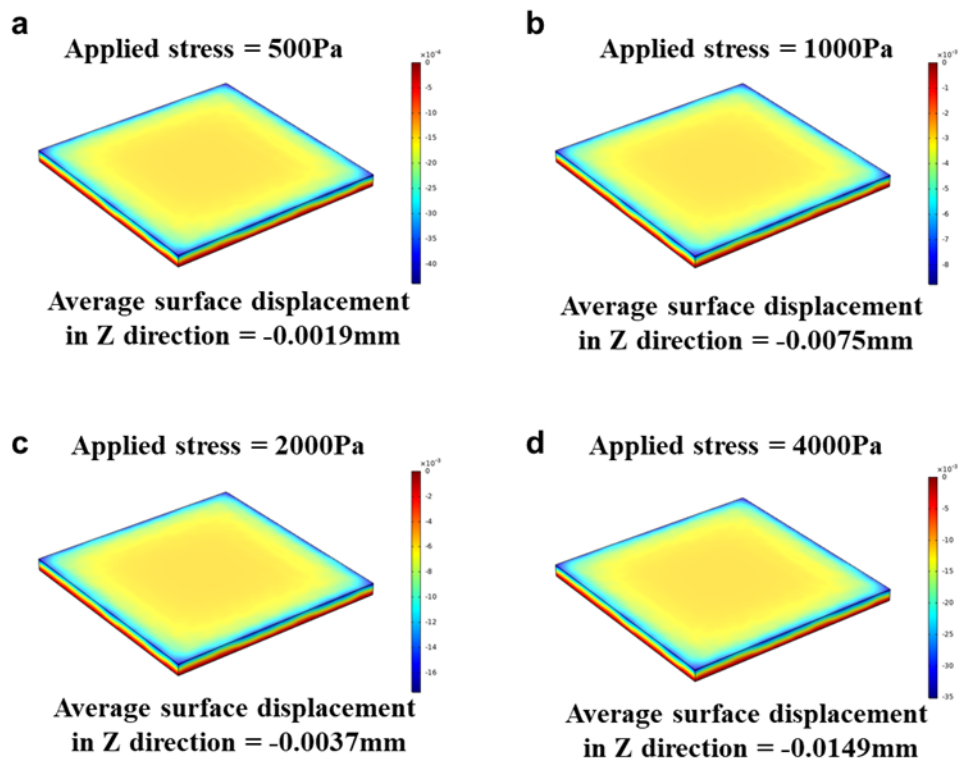


Figure 3-9. The Finite Element Modeling (FEM) Simulation, Z-axis displacement distribution under the applied stress of 0.5, 1, 2, 4 kPa for the planar structure dielectric.

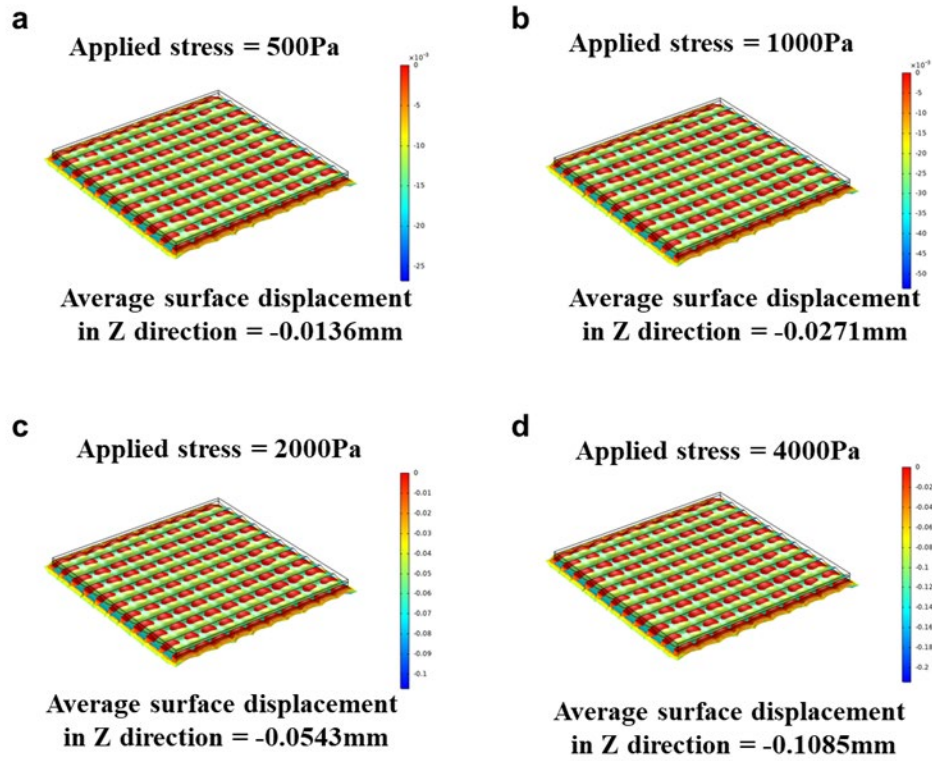


Figure 3-10. The Finite Element Modeling (FEM) Simulation, Z-axis displacement distribution under the same applied stress of 0.5, 1, 2, 4 kPa for the microcylinder structure dielectric

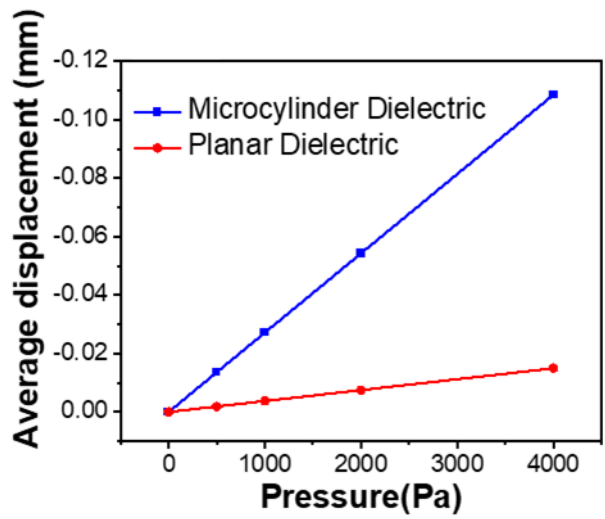


Figure 3-11. Comparison of the average Z-axis displacement of the microcylinder structured dielectric with planar dielectric.

3.6 M2A3DNC pressure sensor characterization

The M2A3DNC pressure sensors' performance metrics were characterized ex-situ. To establish the sensors' calibration curve, the relative change in the capacitance ($\Delta C/C_0$) vs. the loaded pressure (P) was measured, in which the C_0 is the initial capacitance with no pressure loading. The applied pressure was controlled by a pressure gauge, and the capacitance value was recorded with an LCR meter. Since the M2A3DNC pressure sensors particularly target the subtle pressure regime (< 5 kPa) for applications such as monitoring respiratory rate, therefore, the testing pressure load was set within the range up to 4 kPa. The sensitivity (S) of M2A3DNC sensors was experimentally determined as the slope of the calibration curve (equation 3).

$$S = \frac{d(\Delta C/C_0)}{d(\Delta P)} \quad (18)$$

For both M2A3DNC pressure sensor configurations, with a micropatterned dielectric layer and with a planar dielectric layer. Five data points were collected for each pressure load ($n=3$) and presented as an average with standard deviation (Figure 3-12). According to the result, the sensitivity of M2A3DNC sensors with a micro-structured dielectric layer was quantified as 0.512 kPa^{-1} , which was roughly 3.2 times larger than the sensors with a planar dielectric layer ($S = 0.160 \text{ kPa}^{-1}$). As analyzed in the COMSOL simulation (section 2.3), the enhancement can be attributed to the stiffness reduction due to the hemicylinder structure, resulting in a larger deformation of the dielectric layer. Thus, as expected, a more significant capacitance change was obtained under the same applied pressure with the incorporation of the hemicylinder structure, thus showing the effectiveness of the successful formation of the microstructured active layer in multi-layer 3D printing.

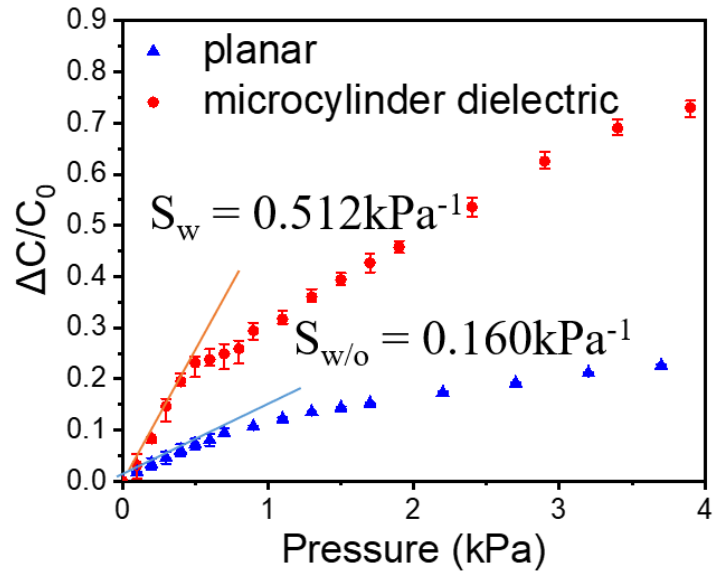
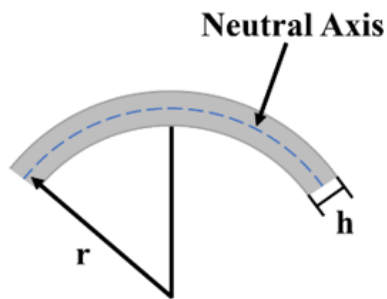


Figure 3-12. Relationship of the capacitance change with the applied pressure from 0 – 4 kPa for the M2A3DNC sensors with and without micro-structure patterned dielectric layer.



$$\epsilon_M = \frac{h}{2r}$$

Figure 3-13. Calculation model for bending strain

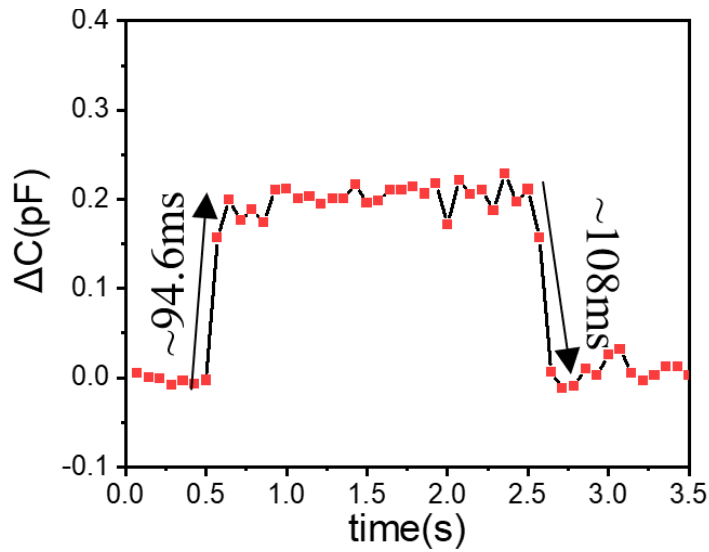


Figure 3-14. The change in capacitance of the M2A3DNC sensors upon applying a 5.4% bending strain followed by the strain release of one representative device.

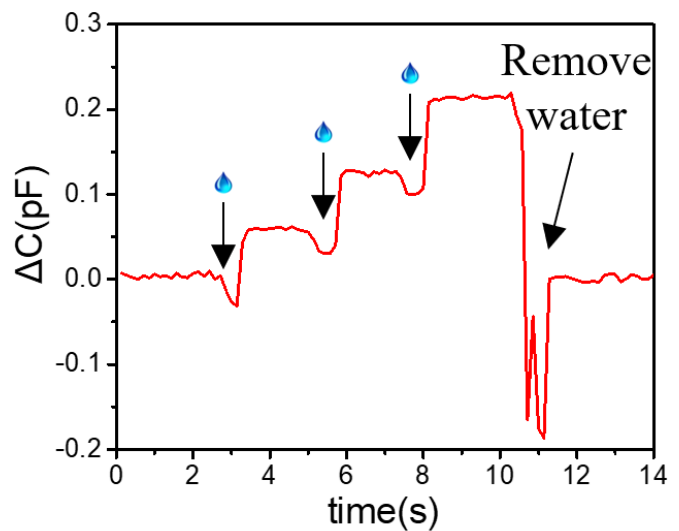
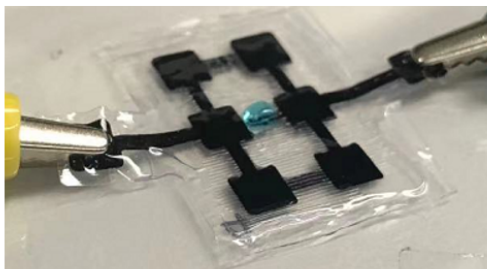


Figure 3-15. The photograph showing the pressure measurement by the application of a water droplet (~ 0.009 kPa), and the M2A3DNC pressure sensor's response to the induced pressure by the addition of three sequentially applied water droplets (~ 0.009 kPa each).

The other key parameters for a pressure sensor are its response time and recovery time. A 5.4% strain bending (6 mm horizontal displacement over the total length of 30 mm, the calculation of the bending strain is explained in Figure 3-13) was applied to the M2A3DNC pressure sensor to find these two parameters. The bending was conducted by a linear motor throughout 6 ms (6 mm displacement in the speed of 1 m/s), held for 2 seconds, and then followed by the strain release at the same speed, and the sensor response was recorded from an LCR meter. As shown in Figure 3-14, the response time and recovery time of our M2A3DNC sensors were recorded as ~ 94.6 ms and 108 ms, respectively, which are in good accordance with other reported carbonate sensors^[66, 94], and it is sufficient to respond for the occurrence of transient physiological signals(e.g., single pulse, 0.6-1.0 s). Next, the detection limit of the M2A3DNC pressure sensors was tested. To be specific, it is determined by investigating the sensors' performance under the applied pressure of a water droplet (12 μ L, ~0.009 kPa), as shown in Figure 3-15. During the test, the sensor was fixed to a stage and connected to the measurement circuit of an LCR meter. After a stable baseline was obtained, single water droplets were sequentially dispensed to the middle of the sensor (3 times), and the sensor response was recorded. As shown in Figure 3-15, the M2A3DNC pressure sensors showed high sensitivity to external ultralow load by detecting the induced pressure of a single water droplet (12 μ L, ~0.009 kPa). The change in capacitance corresponding to the introduction of each droplet was almost identical, indicating a linear behavior of the M2A3DNC pressure sensors in a low-pressure regime. Additionally, when water droplets were removed the sensor's response returns to its initial value, which demonstrates the reusability and reliability of the 3D printed multilayer multi-material active sensors. The achievement of the ultralow limit of detection can also be disclosed from the microstructure creation since the improved compressibility of the dielectric layer enables the sensor to compress

at a smaller external pressure. Water droplet response was also tested on other locations of the sensor, and the results were summarized in Figure 3-16. As expected, the highest sensitivity of the M2A3DNC pressure sensors was recorded when the droplets were dispensed at the center of the sensors.

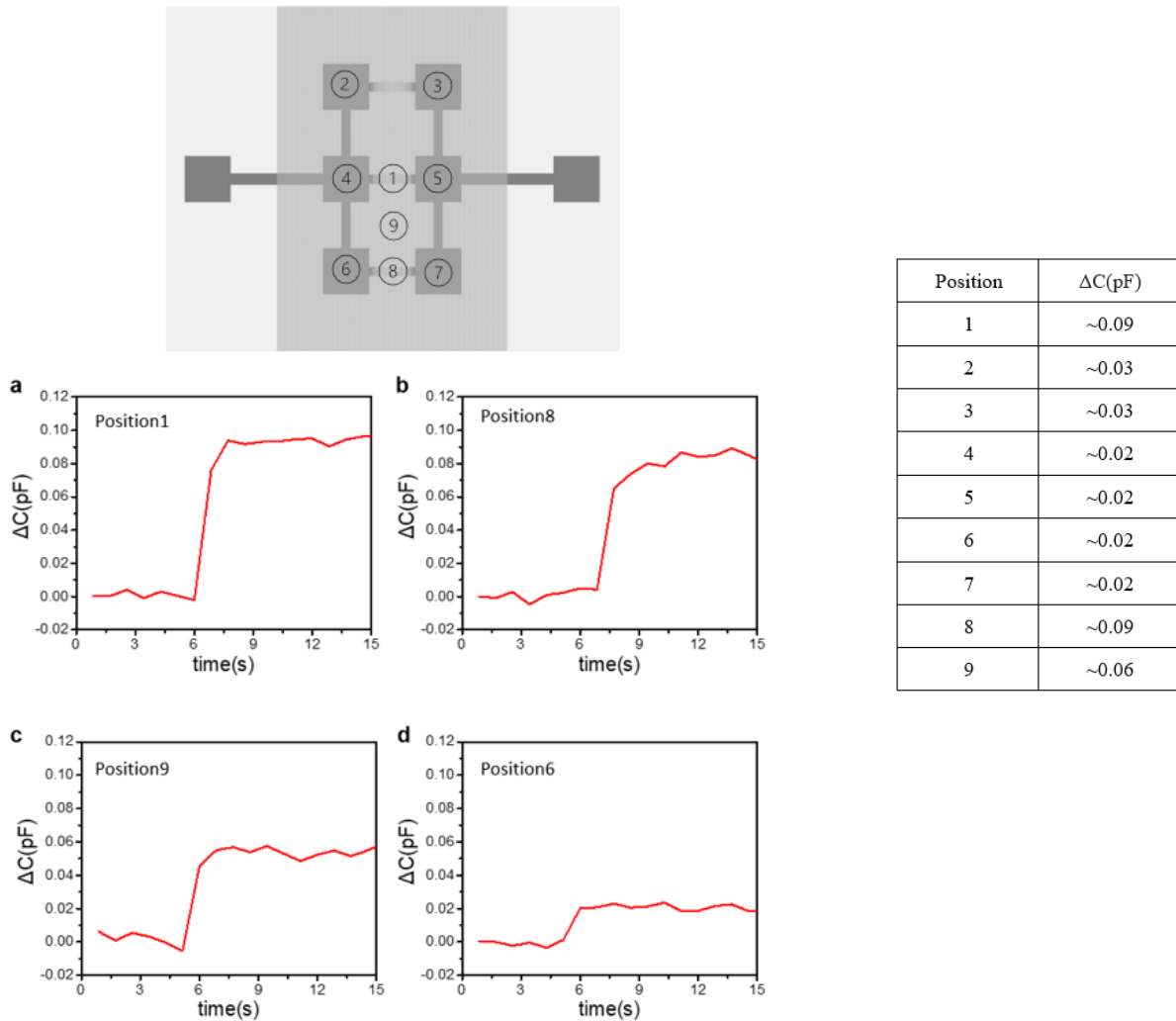


Figure 3-16. Droplet tests on other location. A droplet of 20 μL is applied to different location on the sensor, the change in the capacitance is recorded. a) Drop at the center position 1. b) Drop at the center between 2 bottom capacitor pads, position 8. c) Drop at the center among 4 pads, position 9. d) Drop at the pad, position 6.

Next, the mechanical stability and reliability of the M2A3DNC pressure sensors were examined. Taking the advantages of the elastomer materials for each layer of the sensors, including PDMS, CNT+PDMS, and Ecoflex 00-30, the M2A3DNC pressure sensors were expected to possess distinctive robustness and shape-recovery capability towards different types of relatively harsh distortion (i.e., folding, stretching, twisting). First, the pristine sensor performance under 5.45% bending strain was evaluated. For the 5.45% bending strain experiments, the M2A3DNC pressure sensors were attached to a linear motor for precise control of the bending, and the data was recorded by the Potentiostat. Then, the M2A3DNC sensors were subjected to different types of distortion e.g., 180° folding, hand stretching, and twisting consecutively. After each type of deformation, the sensor was attached back to the same position on the motor, and 5.45% strain bending was applied to it five times repeatedly, and the results were recorded. As shown in Figure 3-17 a-d, the sensors' performance before and after applying distortions showed similar sensing performances with a very slight deviation, which was attributed to all elastomer-based material selection for our sensors. The outstanding mechanical stability had been further authenticated during the loading-unloading and pressing-releasing cyclic tests. The M2A3DNC sensors showed no significant performance change for the full 1,600 loading-unloading cycles (Figure 3-18). In the enlarged view, each cycle had a nearly identical pattern with a slight deviation, which confirms the mechanical robustness of the M2A3DNS sensor over long-time usage as wearables on the human body.

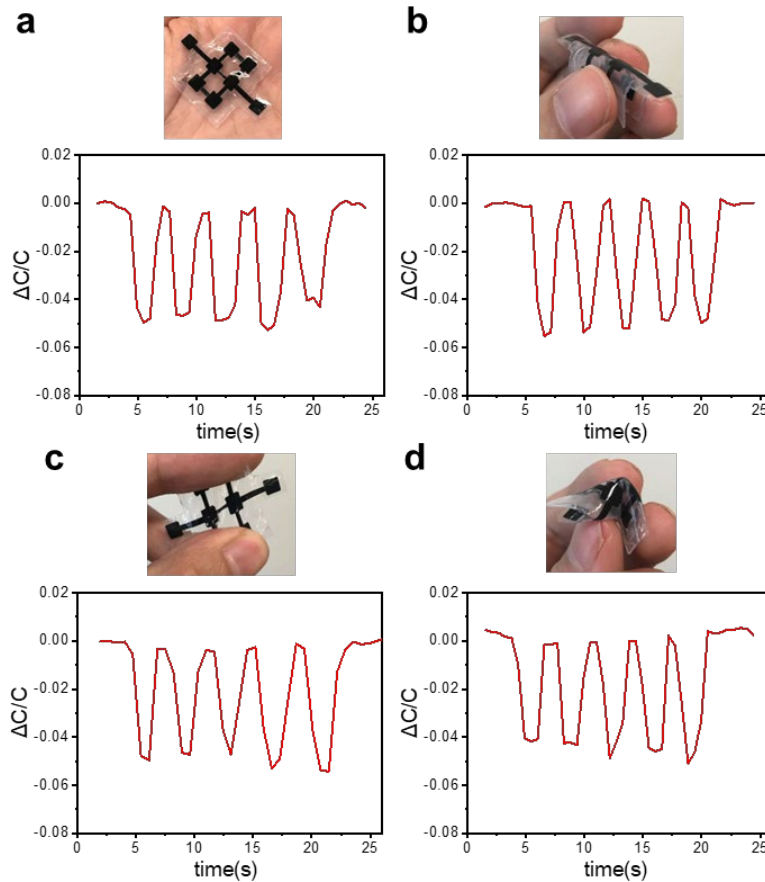


Figure 3-17. Mechanical stability and reliability test of the M2A3DNC pressure sensors. a) Photograph of the M2A3DNC pressure sensor and its performance characteristics under 5 times repeated 5.4% strain bending. b) Photograph of the M2A3DNC pressure sensor subjected to the distortion of 180° outward bending and its performance characteristics under 5 times repeated 5.4% strain bending. c) Photograph of the M2A3DNC pressure sensor subjected to the distortion of hand stretching and its performance characteristics under 5 times repeated 5.4% strain bending. d) Photograph of the M2A3DNC pressure sensor subjected to the distortion of twisting and its performance characteristics under 5 times repeated 5.4% strain bending.

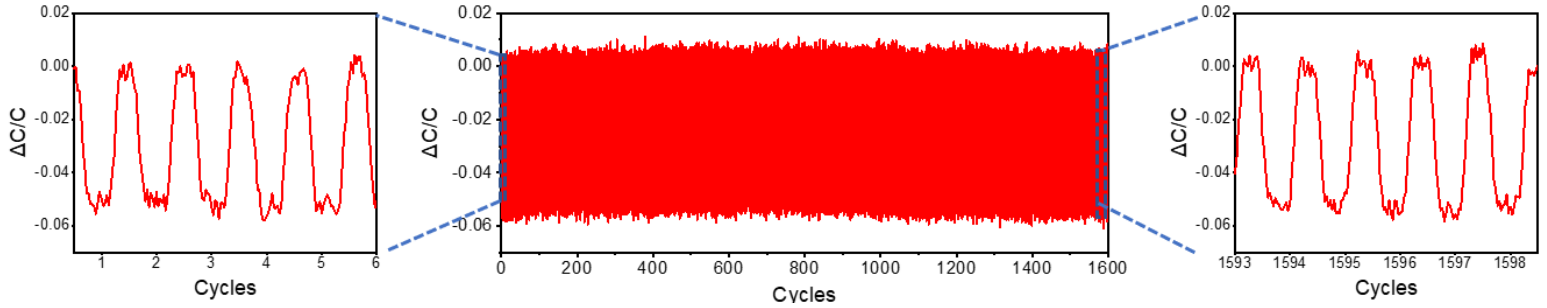


Figure 3-18. Cyclic test of the M2A3DNC pressure sensor with cyclic bending of 5.4% bending strain for 1,600 cycles, and the enlarged view of the marked region.

3.7 In-situ characterization of the sensors

To demonstrate the utility of the M2A3DNC pressure sensors for wearable and health monitoring applications, in-situ experiments were performed by recording diverse physiological biosignals from different mounting locations on the body. All the on-body tests were conducted on a 27-year-old male volunteer. The respiration rate signal was first collected by mounting the M2A3DNC pressure sensor on the belly skin, as shown in Figure 3-19, and different breathing patterns are recorded to mimic the human respiration activity under different conditions. As shown in the figure, the M2A3DNC pressure sensor responds differently to different breathing patterns (i.e., shallow (8 bpm), normal (12 bpm), and deep (20 bpm)) in frequency and magnitude, which are obvious health indicators of the circulatory system and body condition. The measured breathing frequency (i.e., number of peaks) for the normal breathing experiment was within the expected range for a healthy young adult male at the corresponding age range

(12-18 bpm)^[95].

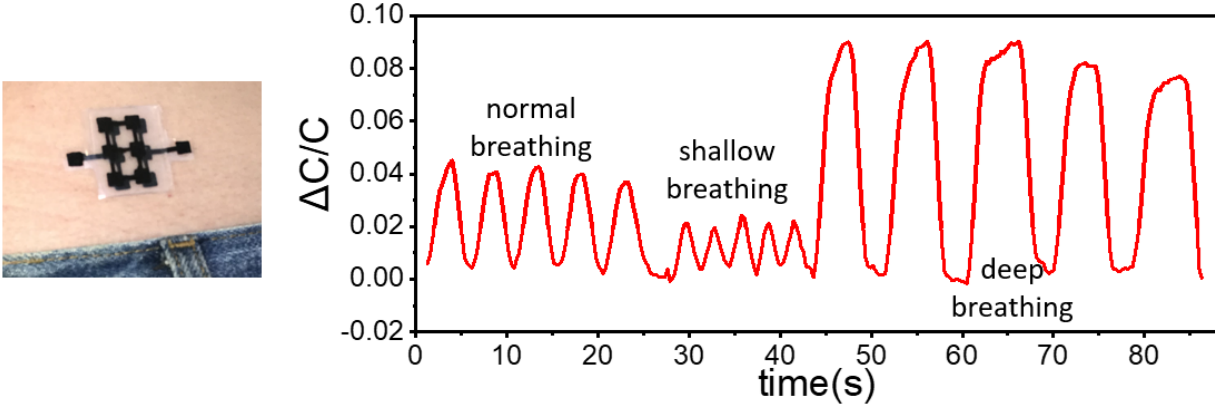


Figure 3-19. Optical image of the M2A3DNC pressure sensor on a human's belly and breathing waves at normal breathing, shallow breathing, and deep breathing states by the M2A3DNC pressure sensor.

Next, the M2A3DNC pressure sensors' utility for the real-time detection of the acoustic vibrations of the larynx when saying different words was demonstrated. For these experiments, the M2A3DNC pressure sensor was attached to the upper throat of a volunteer, as shown in Figure 3-20. Different wording patterns were selected for the test. First, the word "Hi" was repeated by the volunteer several times, resulting in peaks in a similar pattern in the collected output signal. Next, the sentence "How are you!" was repeated by the volunteer to validate the M2A3DNC pressure sensors' utility in detecting the sequential wording patterns. As shown in the figure, a repeatable pattern with 3 peaks was observed, representing the three induced acoustic vibrations while repeating the sentence. However, slight variations between repeated patterns were noticed, which was due to differences in tone and speaking strength.

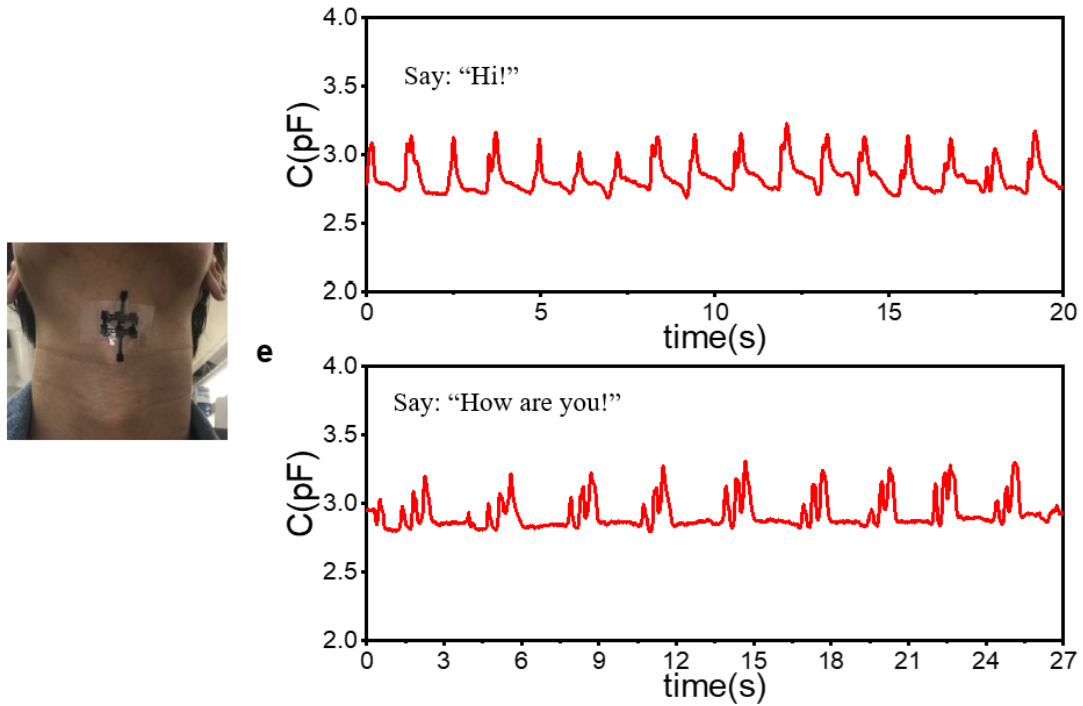


Figure 3-20. Optical image of the M2A3DNC pressure sensor on a human's throat for acoustic vibration measurement (left), and the M2A3DNC pressure sensor attached to the throat detects the acoustic vibrations of the larynx when saying "Hi"(top) and "How are you."(bottom).

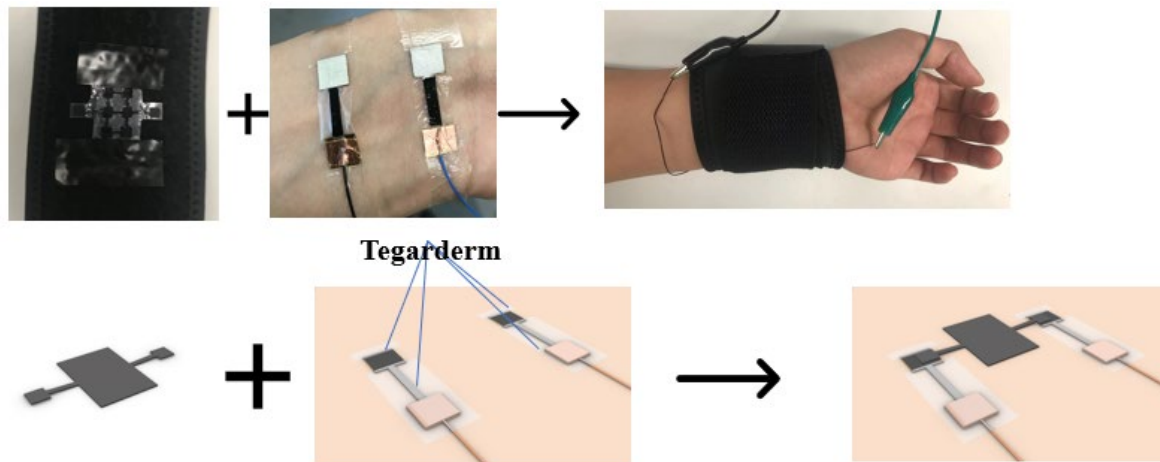


Figure 3-21. Optical image of the M2A3DNC pressure sensor on a human's wrist with an adjustable wrist band, and the schematic showing the conformal contact between the sensor and the epidermal contact on the skin.

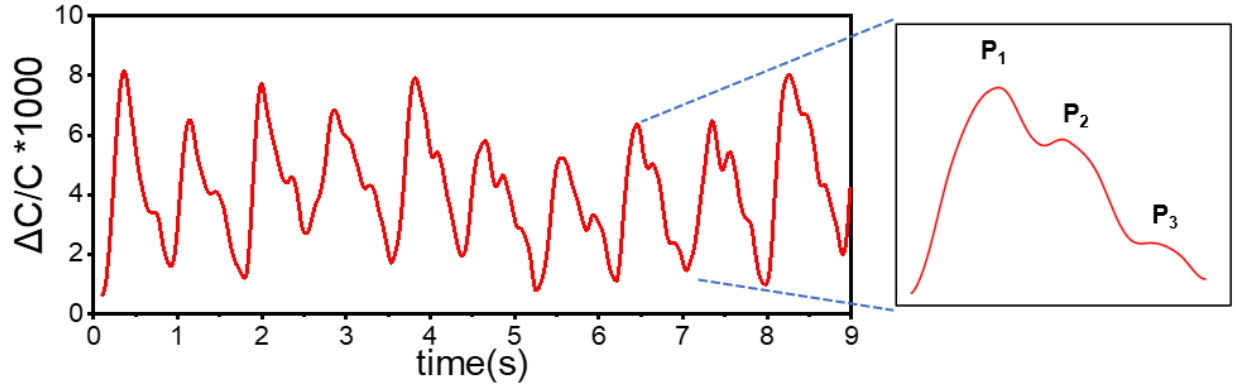


Figure 3-22. The real-time transient pulse signal of the radial artery pulse wave measured with the M2A3DNC pressure sensor. Inset: the enlarged view for one pulse.

In addition, the utility of the M2A3DNC pressure sensors for the wrist radial artery pressure (RAP) waves was demonstrated. For these experiments, the M2A3DNC pressure sensors were attached to a volunteer's wrist by an adjustable wrist band as shown in Figure 3-21. First, the sensor was attached to the inner side of an adjustable wristband. Then the epidermal measuring pads were fixed to the skin surface by a 3M Tegaderm transparent film dressing. Lastly, the wrist band was properly tightened to provide a stable connection between the M2A3DNC pressure sensor pads and the epidermal measuring pads on the skin. Figure 3-22 showed the real-time wrist pulse wave signals measured by an M2A3DNC pressure sensor. In general, the RAP waves were composed of an incident wave (P1), generated by the blood flow, the late systolic shoulder (P2), and another tiny reflection wave (P3) that originated from the lower body. As shown in Figure 3-22 (right), the RAP waves measured by our M2A3DNC pressure sensors showed an average pulse frequency of 68 bpm, which is within the expected range (60 – 100 bpm)[96] for a healthy adult male subject. In the enlarged view of one pulse cycle of the measured real-time RAP signal (the typical peaks of P1, P2, and P3), it exhibits the characteristic peaks of peripheral artery waveforms, which contain important biomedical and physiological information such as

arterial stiffness, coronary artery disease, and myocardial infarction. For instance, arterial stiffness is related to the radial artery augmentation index (AI_r) and the time interval of digital volume pulse (ΔT_{DVP}), defined as $P2/P1$ and the time difference between the P1 and P2 peaks, respectively. By inspecting the read-out signal from the M2A3DNC pressure sensor, the arterial stiffness condition can be continuously recorded.

Thus, the proposed novel multilayer multi-material 3D printed microengineered optimized active sensor showed broad application potentials in real-time health monitoring, which will be the future of non-invasive disease detection at the early stages in the present era.

3.8 Summary

In this chapter, we reported a highly sensitive, robust, flexible, biocompatible, hybrid, and rapidly integrable multi-material all-3D-printed nanocomposite-based (M2A3DNC) wearable pressure sensors. The 3D printing techniques offer a rapid, and cost-effective path to ease the fabrication by the programmable automated layer-by-layer construction and raise the design tolerance for its mask-free prototyping capability. Additionally, by the incorporation of the directly printed micro-hemicylinder structures in the dielectric layer of the M2A3DNC pressure sensors, it offers a low detection limit (~ 0.009 kPa), high-pressure sensitivity (0.512 kPa $^{-1}$), fast response time, distortion resistivity, and high durability (1,600 cycles compression). Notably, the utility of the M2A3DNC pressure sensors for a wide range of applications in wearable personalized health monitoring, including respiratory rate monitoring, artery pulse recording, vocal cord vibration pattern detection, was successfully demonstrated. It is worth noting that the advantages of accomplishment of structural engineering in multilayer 3D printing are not limited to wearable sensors for the healthcare industry. It also paves a new pathway for advances in

robotics tactile sensing, human-machine interface, and more other applications are remained to be explored.

3.9 Materials and Methods

CNT+PDMS ink preparation(12wt%): 360 mg MWCNT (10-20 nm, 10-30 μm , Nanostructured & Amorphous Materials Inc, TX) was mixed with 7200 mg toluene (Certified ACS grade, Fisher Scientific, NH) (1:20 in weight) and magnetic stir at 700 rpm for 2 hours. 2640 mg PDMS (Sylgard 184 Silicone Elastomer Base, Dow Corning, MI) was mixed with 9486 mg toluene (1:4 in volume) for 2 hours. Poured the PDMS mixture in the CNT mixture, baked at 50°C, and stirred at 250 rpm to evaporate the solvent. 264 mg curing agent was added when it was close to the end of the evaporation. The whole mixture was further mixed by a Vortex mixer for another 20 min and could be ready for 3D printing.

PDMS ink: Mixed SE 1700 (Dow Corning, MI) and Sylgard 184 base materials with their curing agents for 10 min in a 10:1 ratio. Both blends were degassed in a vacuum desiccator for 20min. Then, mixed SE 1700 and Sylgard 184 in a 2:1 ratio for 10 min, followed by a 4900 rpm centrifuge for 20 min to remove the bubbles.

Ecoflex ink: Mixed Ecoflex 00-30(Smooth-On Inc) part A with part B in the ratio of 1:1, the mixture was Vortex mixed for 5min and centrifuge at 2000 rpm for 3min. The ink should be used within 40 minutes after mixing to avoid the viscosity change by curing.

Fabrication of multi-material 3D printed sensor: A sacrificial layer of poly(vinyl alcohol) (PVA) layer is prepared by spin coating on a glass slide (7.5 cm long, 5 cm wide, and 1 mm thick). PVA solution with a 1 to 10 weight ratio of PVA to DI water was spincoated on a glass slide at 1000 rpm for 60 s to make a 750 nm thick PVA layer. This PVA layer is dried by heating the glass

slide on a hotplate at 95 °C for 5 min. The printing process of PDMS, CNT+PDMS, starts with the 3D patterns, which were developed using Solidworks (Solidworks Corp) and then slicing and generating g-code by Heartware (Cellink, MA). After that, the designed patterns were printed by the Incredible+ 3D extrusion bioprinter (Cellink, MA). For PDMS ink extrusion, a 200 µm inner diameter conical nozzle was used and extruded at the speed of 10 mm/s under 80 kPa. For CNT ink extrusion, a 260 µm inner diameter stainless steel nozzle was used and extruded at the speed of 7 mm/s under 120 kPa pressure. For Ecoflex 00-30 (Smooth-On, PA), a 100 µm inner diameter nozzle was used and extruded at the speed of 10 mm/s under 4 kPa pressure. The curing conditions of PDMS/CNT+PDMS/Ecoflex 00-30 were 100 °C for 60 min / 100 °C for 60 min / 80 °C for 30 min, respectively. The sensor was assembled by the stick adhesive-like property of partially cured Ecoflex 00-30, and the resulting sample was freed from the substrate in a 90 °C water bath for 2 hours and dried in the air before use.

Printing Optimization: To test the influence of the printing resolution, 4 pressures (90kPa, 100kPa, 110kPa, 120kPa), 7 speeds (from 1mm/s to 7mm/s) and 3 different nozzle sizes (0.51mm, 0.34mm, 0.26mm) had been studied. At each condition, 5 repeated lines were printed, the average and the standard deviation were recorded for the printing result under this condition. The width and the thickness were measured by Vernier Caliper, and the resistance was measured by the LCR meter (GW Instek LCR-819), and the resistivity was calculated from the resistance and the printed line geometry.

Characterization: The bending test was conducted by using the Linmot motor. Both ends of the sensor were fixed to the arms of the motor by Scotch tape. Bending was performed under the pattern of 3 seconds bending and 3 seconds releasing 5 times for the setting condition, which is 5.4% bending strain. After obtaining the bending performance of the as-fabricated sensor, the

sensor was subjected to folding, stretching, and twisting. And the same experiment was performed after each distortion. The pressure test was conducted in two parts. The pressure control was performed by TA Q-800 Dynamic Mechanical Analyzer, and the data was collected by LCR meter and plotted by Origin software.

On-body test: The sensor was attached to different body locations. For the breathing test, the sensor was taped to the side belly by using scotch tape, and the data was collected by LCR meter. For the vibration test, the sensor was taped to the upper throat. For the heart pulse test, the sensor was first fixed to an adjustable wrist band, and an epidermal contact for the circuit connection was adhered firmly on the skin by the Tegaderm (3M, MN). Then the wristband was properly fastened to make sure the contact and fix the sensor. Zurich Impedance spectroscopy was used to measure the data, the frequency was set to 300 kHz under the voltage of 0.1 V, and the sampling rate was 175 samples per second. The collected data were processed by MATLAB to calculate the capacitance value.

Institutional Review Board Approval: The conducted human subject experiments were performed in compliance with the protocols. Exempt Self-Determination Tool that has been provided by the Institutional Review Board, Human Research Protections at the University of California, Irvine. All subjects gave written informed consent before participation in the study.

Chapter IV. A Self-powered Triboelectric MXene-based 3D-printed Wearable Physiological Biosignal Sensing System for On-demand, Wireless, and Real-time Health Monitoring

4.1 Overview

The development of wearable and flexible sensing devices has dramatically broadened the scope of personalized health monitoring [97-99]. They offer a facile non-invasive approach to extracting real-time physiological data essential for health monitoring [7-9]. Over the past decade, extensive studies have been carried out to fabricate wearable sensing devices with high sensitivity for the precise and accessible collection of vital signals. For instance, recently a stretchable vertical graphene network for respiration monitoring [100], a multifunctional 3D printed CNT based pressure sensor to record pulses and vocal vibration [25], a wearable sensor patch to monitor electrocardiography, glucose, and temperature [101], an affordable sensor for pH monitoring [102], and an ultrasensitive aptamer-antibody cortisol sensor to monitor the stress state [103] have been developed by different groups. However, most of such devices rely on rigid battery packs. Although flexible batteries enable conformal contact with the skin, limitations include charging requirements, replacement issues, and potential security risks [104-106]. Thus, integrated sensing systems with sustainable power remain to be achieved. Though energy harvesting approaches such as photovoltaics [107, 108], thermoelectric generators [109, 110], and biofuel cells [111] enable direct electricity acquisition from surroundings, their operation is restricted by external conditions, including temperature, light, and auxiliary catalysts [112]. Therefore, more active and less environmentally dependent acquisition approaches could satisfy the requirements of mobility, wearability, and integrability.

Triboelectricity refers to the electrification of materials due to friction or frequent contact with another material [112]. By collecting charges generated on material surfaces, triboelectric nanogenerators (TENGs) convert mechanical energy from human motion into electricity without previously mentioned restrictions (e.g., temperature, light) [113-115]. Due to their simple structure, low cost, universal availability, and high conversion efficiency [116-118], TENGs have broad applications and potential [119, 120]. For instance, in 2019, Bhaskar et al. introduced a polyaniline-based wearable TENG-based sensing system [121], which took advantage of the generated triboelectric output variation caused by external stimulus and used TENG directly as a pressure sensor. However, such sensors showed limited sensitivity without a micro-engineered active sensing layer or a portable data acquisition unit. In 2020, Gao et al. developed a triboelectrically driven system powering sweat biosensors for biomarker monitoring [98]. However, their system was limited to recording discrete data points, minutes apart, and incapable of continuous monitoring of transient physiological biosignals. Thus, accurate, efficient, continuous, and real-time recording of transient physiological signals remains to be achieved.

Considering all the needs mentioned above, in this chapter, we have proposed, developed, fully characterized, and validated a novel, self-powered, "all-in-one", MXene-based, 3D-printed, and integrated wearable sensing system for on-demand, continuous, and real-time vital signal monitoring. The system includes highly efficient TENGs, highly sensitive pressure sensors, and multifunctional circuitry. MXene, a two-dimensional (2D) transition material with distinctive triboelectric properties [122], outstanding conductivity [123], and mechanical flexibility [124] has been applied to the triboelectrification layers for the TENG and the conducting layers for the pressure sensors. Moreover, its shear-thinning viscoelastic property provides opportunities for additive 3D manufacturing in various devices. Our 3D-printed, wearable, MXene-based, self-

powered physiological signal sensing system (MSP²S³) exhibits an output power of $\sim 816.6 \text{ mW m}^{-2}$ for its TENGs, the sensitivity of 6.03 kPa^{-1} , a low detection limit of 9 Pa , and a fast response time of 80 ms for its pressure sensors (Figure 4-2). This enables continuous, real-time, and on-demand radial artery pressure (RAP) waveform monitoring without any external power supply.

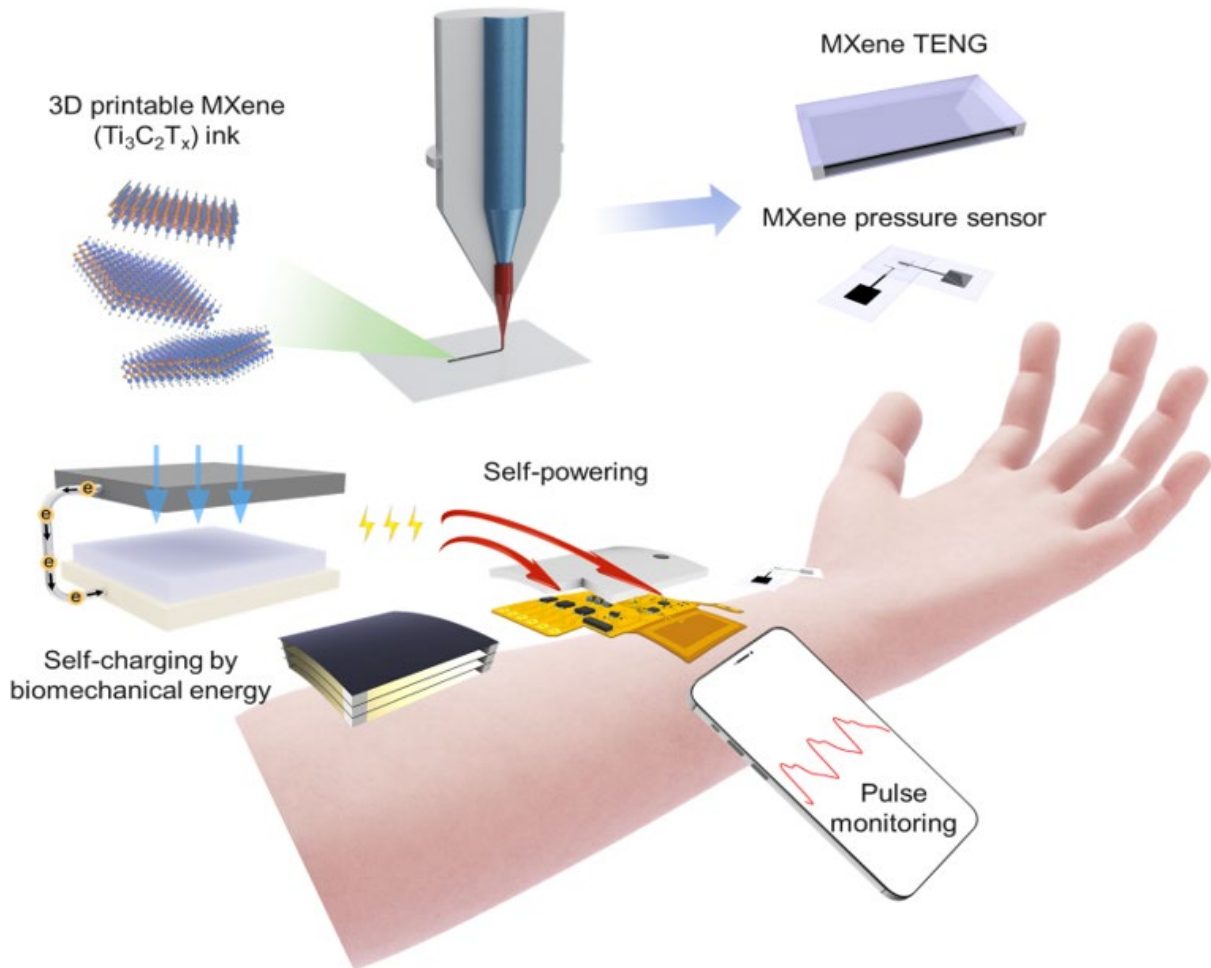


Figure 4-2. Schematic of the MXene-based self-powered physiological sensing system (MSP²S³), which comprises a MXene-based TENG (M-TENG); a MXene-based pressure sensor (M-PS), both fabricated via additive manufacturing (3D printing) using home-modified MXene ink; a

power-management circuitry; an energy-storing circuitry; and data collecting, and wireless data/power transmitting modules.

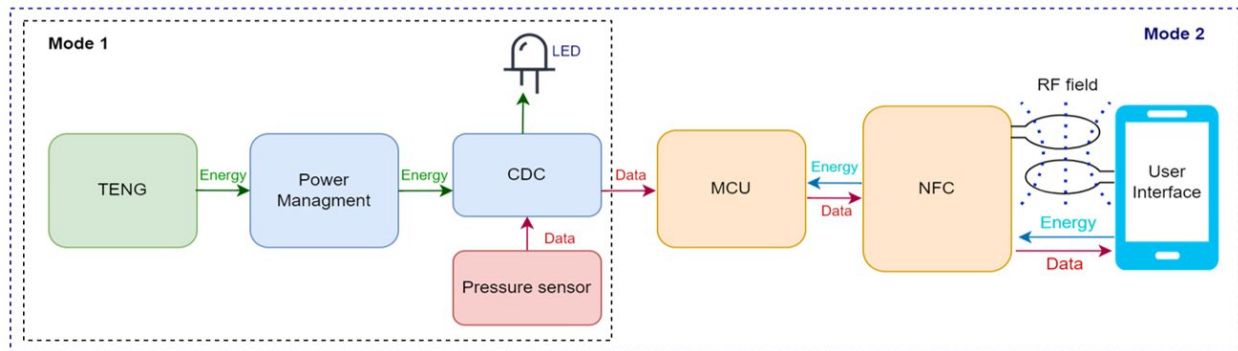


Figure 4-3. System-level block diagram illustrating the MSP²S³ different modules in modes one and two.

The MSP²S³ is a two-mode system (Figure 4-3). In mode one, the system is entirely self-powered by the TENG units, measuring RAP peaks from the wrist continuously in real-time. Specifically, the MXene-based TENG units harvest the mechanical energy from the user's finger tapping, powering an embedded capacitance-to-digital-converter (CDC) chip, the MXene-based pressure sensors, and LEDs. The CDC chip communicates with pressure sensors and the LEDs to visualize the valleys and peaks of the measured RAP waveforms with the "on" and "off" states, respectively (one flash per pulse).

In mode two, the TENGs still power the CDC chip and pressure sensors, while a smartphone wirelessly powers a near field communication (NFC) chip and a microcontroller unit (MCU), enabling wireless power and data transmission. The MCU extracts the measured RAP data directly from the CDC chip, and the NFC chip transmits it to the phone for display and storage. A custom Android App decodes the data and plots the RAP waveforms in real-time. To the best of our knowledge, this is the first fully integrated, triboelectrically-driven-self-powered, battery-free,

wireless, and MXene-based wearable sensing system for continuous real-time physiological signal monitoring.

4.2 High-performance MXene ink for additive manufacturing

MXene, a recently emerging 2D material, has received extensive interest for its excellent electrical characteristics and mechanical stability [125-127]. Its carbon backbone enables electricity passage and out-plane flexibility (Figure 4-4). In addition, its abundant surficial termination groups (hydroxyl, oxygen, and fluorine) make MXene triboelectric similar or even more negative than the commonly used triboelectrically negative material- polytetrafluoroethylene (PTFE) in triboelectric series (figure 4-5) [128-130]. As a result, MXene is an ideal material for flexible triboelectric layers and conductive electrodes.

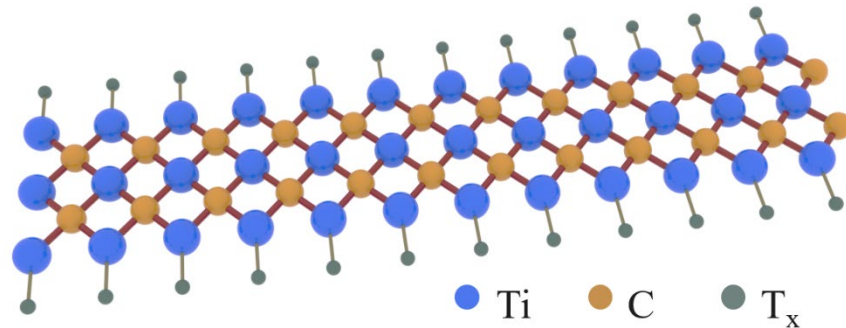


Figure 4-4. Schematic of chemical structure of 2D Ti₃C₂T_x MXene.

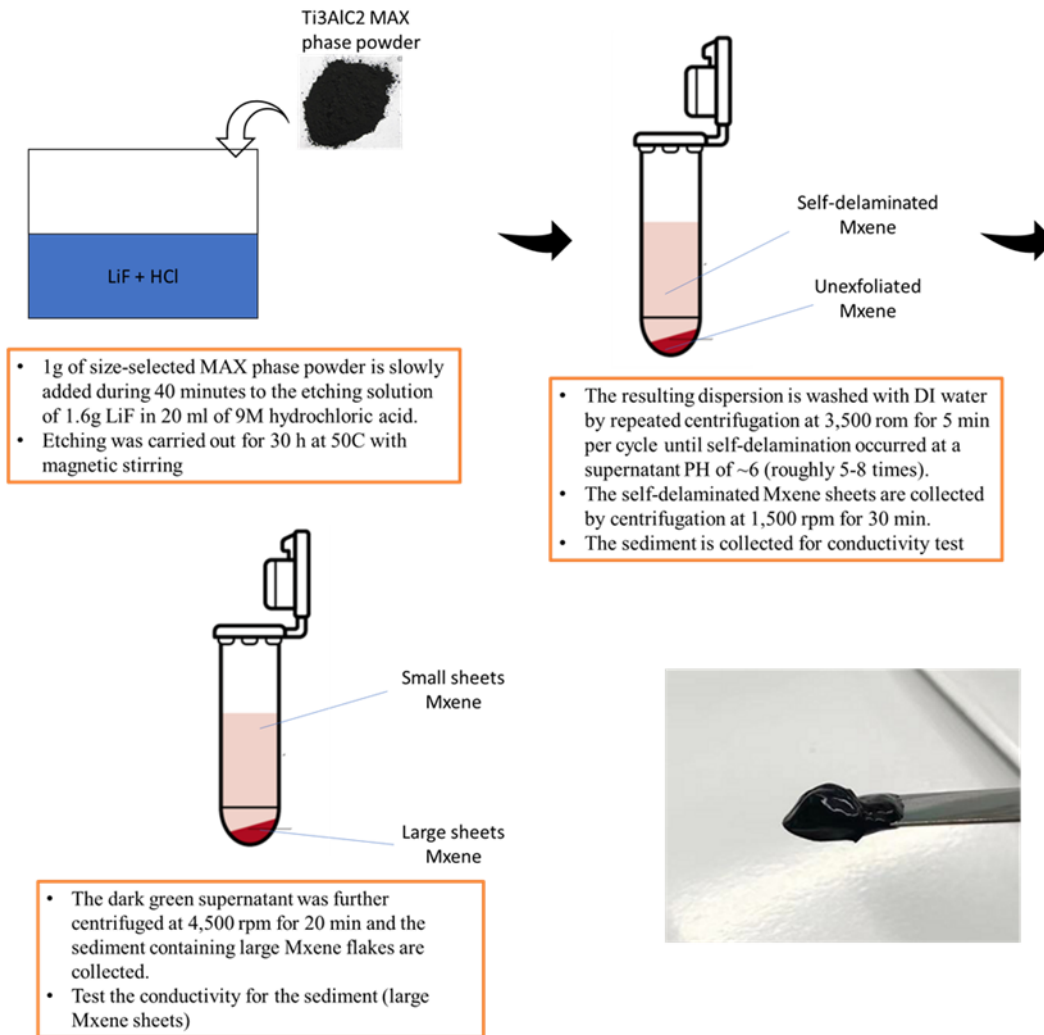


Figure 4-7. Illustration schematic for the home-modified large flake MXene ink for 3D printing

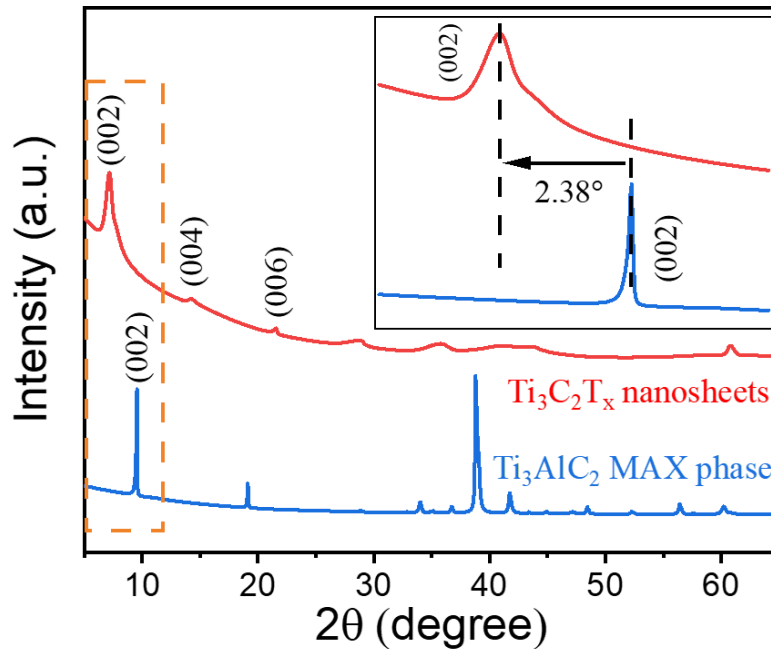


Figure 4-8. XRD patterns of the synthesized MXene ($\text{Ti}_3\text{C}_2\text{T}_x$) and MAX phase (Ti_3AlC_2) powder; the inset shows the 2.38° downshift of the (002) peak, indicating the intercalation of ions into the interlayer.

$\text{Ti}_3\text{C}_2\text{T}_x$ MXene ink was synthesized using the minimally intensive layer delamination (MILD) method by selective etching of the aluminum layers from the Ti_3AlC_2 MAX phase and delaminated into 2D monolayer sheets using intercalation agents such as metal ions or organic molecules. A viscoelastic gel-like black sediment was obtained after synthesis and purification, with several material characterizations. First, the phase composition and crystal structure analyses were conducted using an X-ray diffractometer (XRD), and Ti_3AlC_2 and the synthesized $\text{Ti}_3\text{C}_2\text{T}_x$ patterns were compared. As illustrated in Figure 4-8, the characteristic peaks of Ti_3AlC_2 in the range of 33° - 43° of Ti_3AlC_2 eventually disappeared, indicating completed etching. In addition, the (002) peak of the synthesized $\text{Ti}_3\text{C}_2\text{T}_x$ MXene shifted toward a smaller 2θ angle by 2.38° , indicating the expansion of the c-lattice parameter. This downshift was because of the intercalation of ions and/or small molecules into the interlayer of MXene [134-136], indicating delamination of the 2D sheets.

Next, Fourier transform infrared spectroscopy (FTIR) was performed for chemical bonding identification. The spectrum of synthesized $\text{Ti}_3\text{C}_2\text{T}_x$ reflecting the chemical composition of MXene is shown in Figure 4-9. Peaks at 3301 and 1631 cm^{-1} indicated the presence of strong hydrogen bonding ($-\text{OH}$), and the peak at 583 cm^{-1} was attributed to the deformation vibration of the $\text{Ti}-\text{O}$ bond [137]. In addition, the morphology of the extrusion-based 3D-printed MXene film was measured by cross-sectional SEM imaging. A well-percolated nanosheet network was obtained, showing the 2D sheet delamination and the natural flake alignment via the 3D extrusion printing process (Figure 4-10).

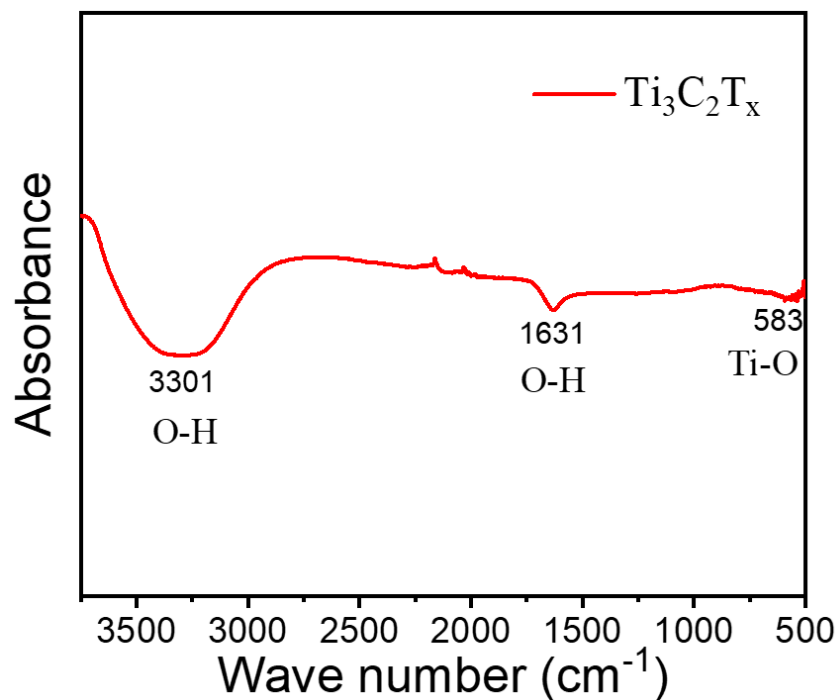


Figure 4-9. FTIR pattern of the synthesized MXene.

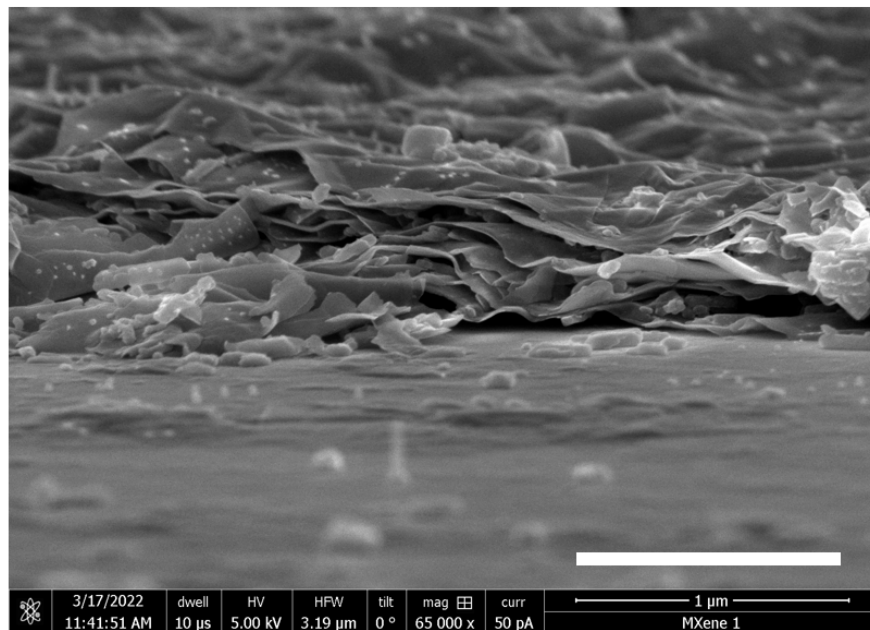


Figure 4-10. Side-view SEM image of a MXene film showing the stack layers of nanosheets.

Various factors affecting the electrical and mechanical properties of MXene include particle flake size, defects on the MXene flakes due to sonication, voids in the film due to the irregular stacking of the flake, and flake alignment [124, 138, 139]. Generally, the larger the MXene flakes, the greater the electrical conductivity. To maximize the electrical performance of the 3D-printable MXene ink, two refinements were made: i) the size of the raw MAX phase powers was selected to relate directly to the flake size after etching; and ii) vigorous sonication was avoided to ensure minimal damage to the $Ti_3C_2T_x$ flakes, instead of employing metal ion intercalation and moderate magnetic bar stirring. Flake morphology and size distribution for the refined large flakes (Figure 4-11 and 4-12) and broken small flakes were characterized by top-view SEM (Figure 4-13 and Figure 4-14). The electrical conductivity performance was also measured under different refinement processes. As shown in Figure 4-15, the refined large flakes and broken small flakes exhibited a mean lateral size ($\langle l \rangle$) of 4.12 μm and 0.29 μm , respectively, indicating flake

elimination in the submicron scale. The electrical conductivity performance enhancement under different refinement stages was achieved. As shown in Figure 4-16, MILD synthesis without flake size modification yielded ink conductivity of 1535 ± 396 S/cm. With the selection of MAX phase particles $>10 \mu\text{m}$, higher conductivity of 3616 ± 598 S/cm was obtained. The elimination of broken flakes under the micro-scale during purification further increased the ink conductivity to 5096 ± 332 S/cm. The lower conductivity noted in unmodified ink is attributed to the presence of more inter-particle contacts in conductive paths resulting in a higher scattering rate of electrons at boundaries with the presence of small particles [140]. Thus, flake size refinement remarkably enhanced the electrical performance of the 3D-printable MXene ink, compared to previous reports [141].

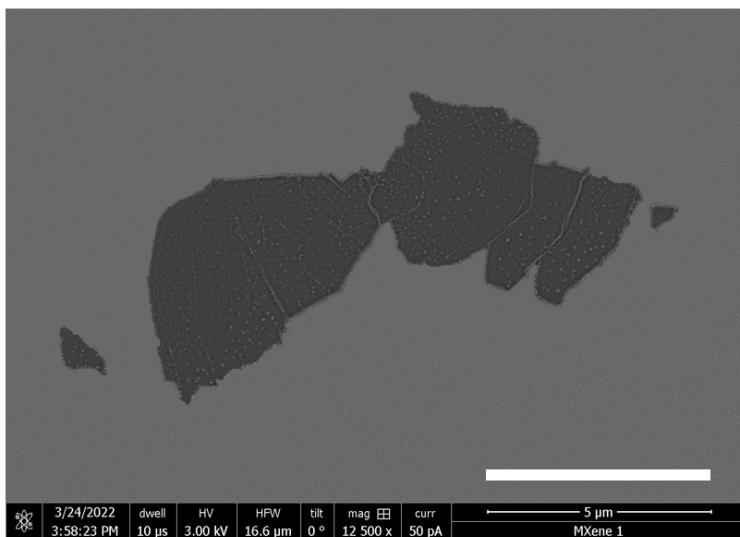


Figure 4-11. Top-view SEM image of the large flake MXene of the 3D printable ink showing surface morphology and typical flake sizes.

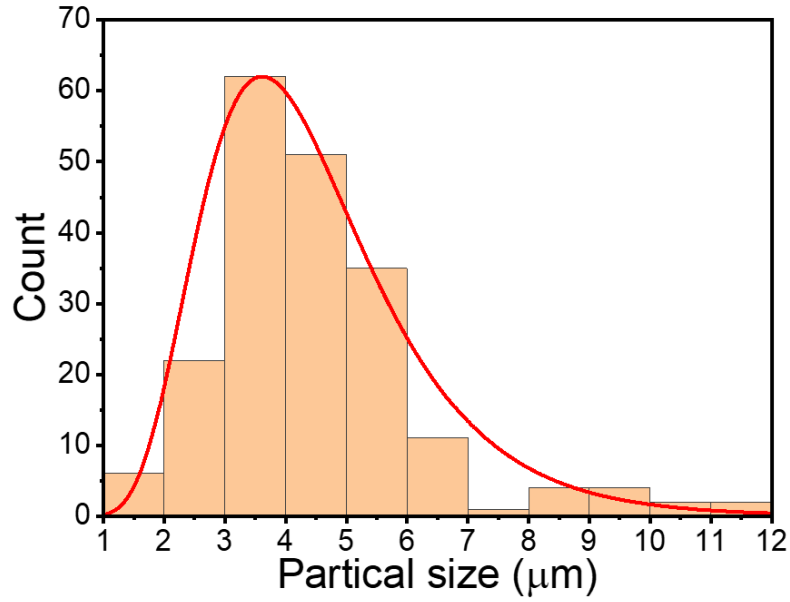


Figure 4-12. Lateral size distribution of large MXene flakes. The sizes of 200 flakes are counting from 5 different $150 \mu\text{m} \times 100 \mu\text{m}$ rectangles of a silicon wafer deposited with diluted MXene dispersion of large flakes.

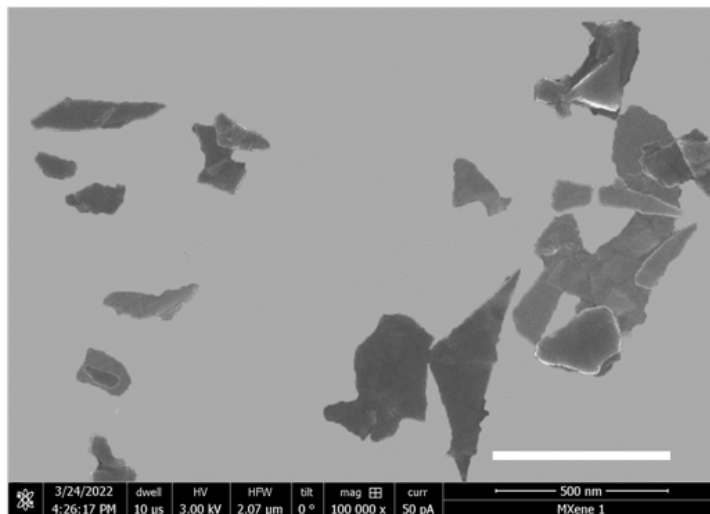


Figure 4-13. Top-view SEM image (scale bar: 500 nm) of the small MXene flake. The sizes of 200 flakes were counted from 5 different $1.8 \mu\text{m} \times 1.2 \mu\text{m}$ rectangles of a silicon wafer deposited with diluted MXene dispersion of small flakes.

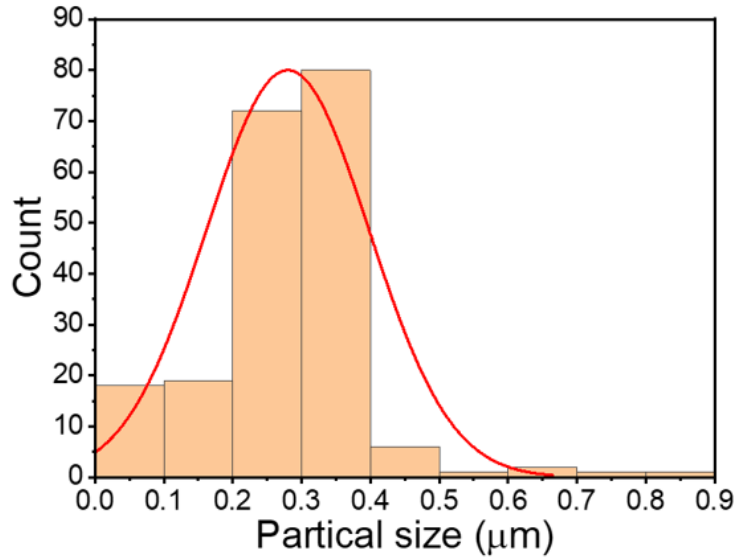


Figure 4-14. Lateral size distribution of small MXene flakes.

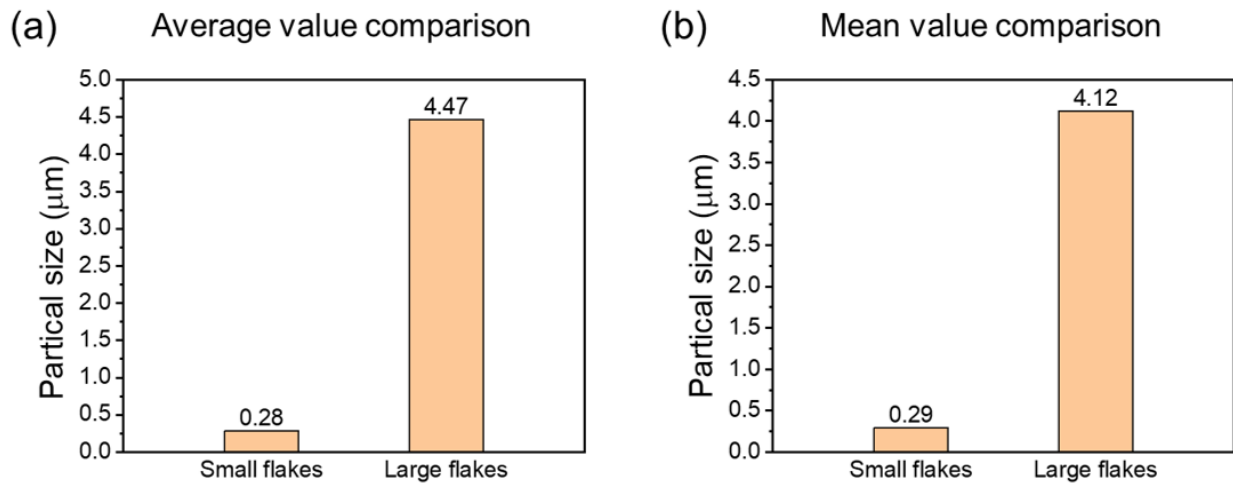


Figure 4-15. The average (a) and mean (b) particle size values between small and large flakes.

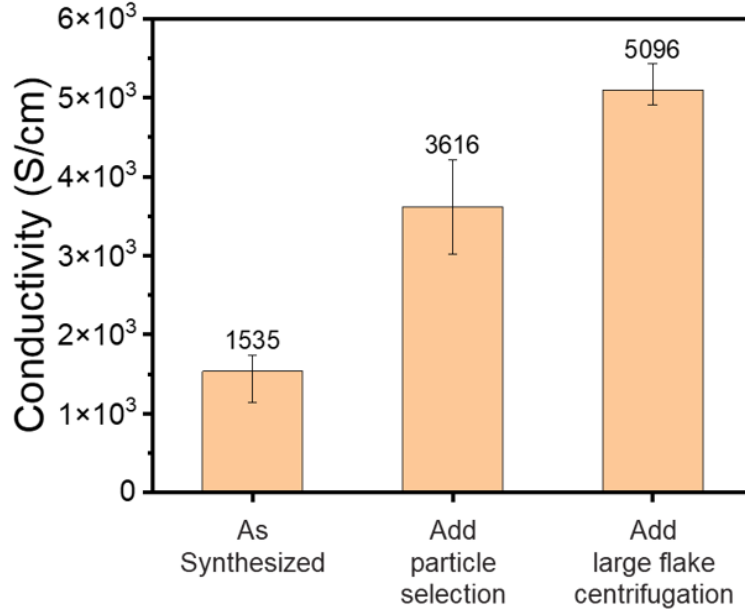


Figure 4-16. The Ink conductivity during different preparation processes.

To determine the suitability of MXene ink for additive manufacturing, viscosity must first be characterized. It describes the resistance to flow as a relationship between stress and deformation rate. Though extrusion at a high shear rate requires low viscosity, high viscosity is necessary to retain the printed shape. This material performance characteristic, called shear-thinning behavior, can be characterized using the Ostwald-de Waele power-law viscoelastic model [142], with the power index n between 0 and 1 ($0 < n < 1$):

$$\mu = k\gamma^{n-1} \quad (19)$$

where μ is the viscosity, γ is the shear rate, n is the power index, and k is the flow index.

As shown in Figure 2-3 from previous section, after fitting the experimental data, MXene ink at 4 wt% exhibited a typical shear-thinning behavior with $n = 0.07$. Additionally, as shown in Figure 4-17, by increasing the shear rate, the dominant modulus of the ink changes from storage modulus to loss modulus that is favored for the extrusion process. Viscosity can be further modified by

tuning the ink concentration. The presence of the hydroxyl functional group in the MXene flakes favors mixing with water. Homogeneous mixtures with different viscosities can be obtained by managing the solvent ratio (i.e., 4 wt%, 4.5 wt%, and 5 wt%, Figure 2-3). The power index (n) and flow index (k) followed the governing equation of $n = 1 - 0.57594(C)^{0.3156}$ and $k = -172C^2 + 1980C - 5010$, respectively, depending on the ink concentration, allowing adjustment of viscosity to different extrusion systems to achieve a high printing resolution of $\sim 100 \mu\text{m}$ (Figure 4-18).

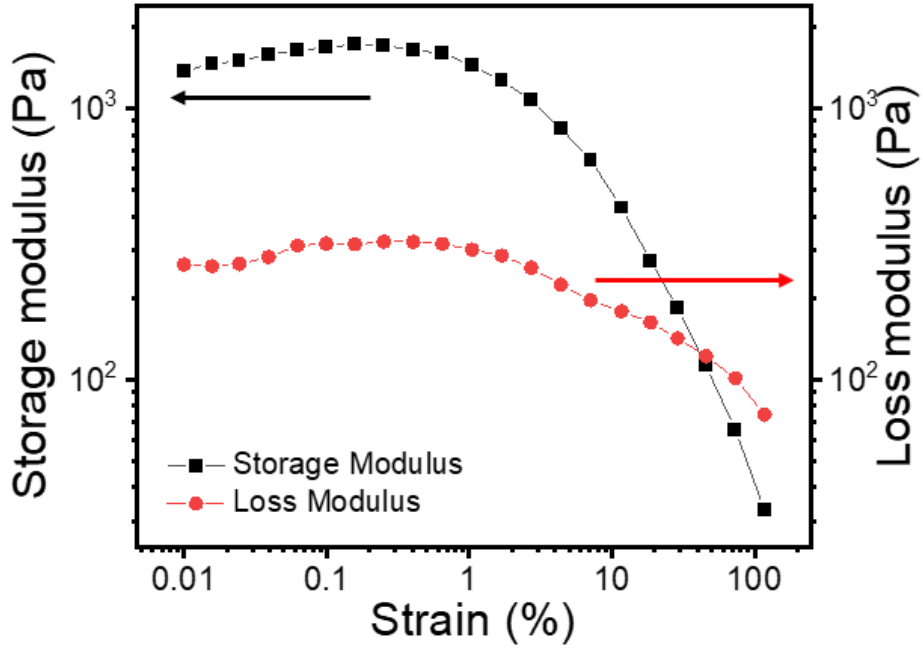


Figure 4-17. Rheological properties of 3D printable MXene ink with the storage and loss modulus plotted as a function of strain.

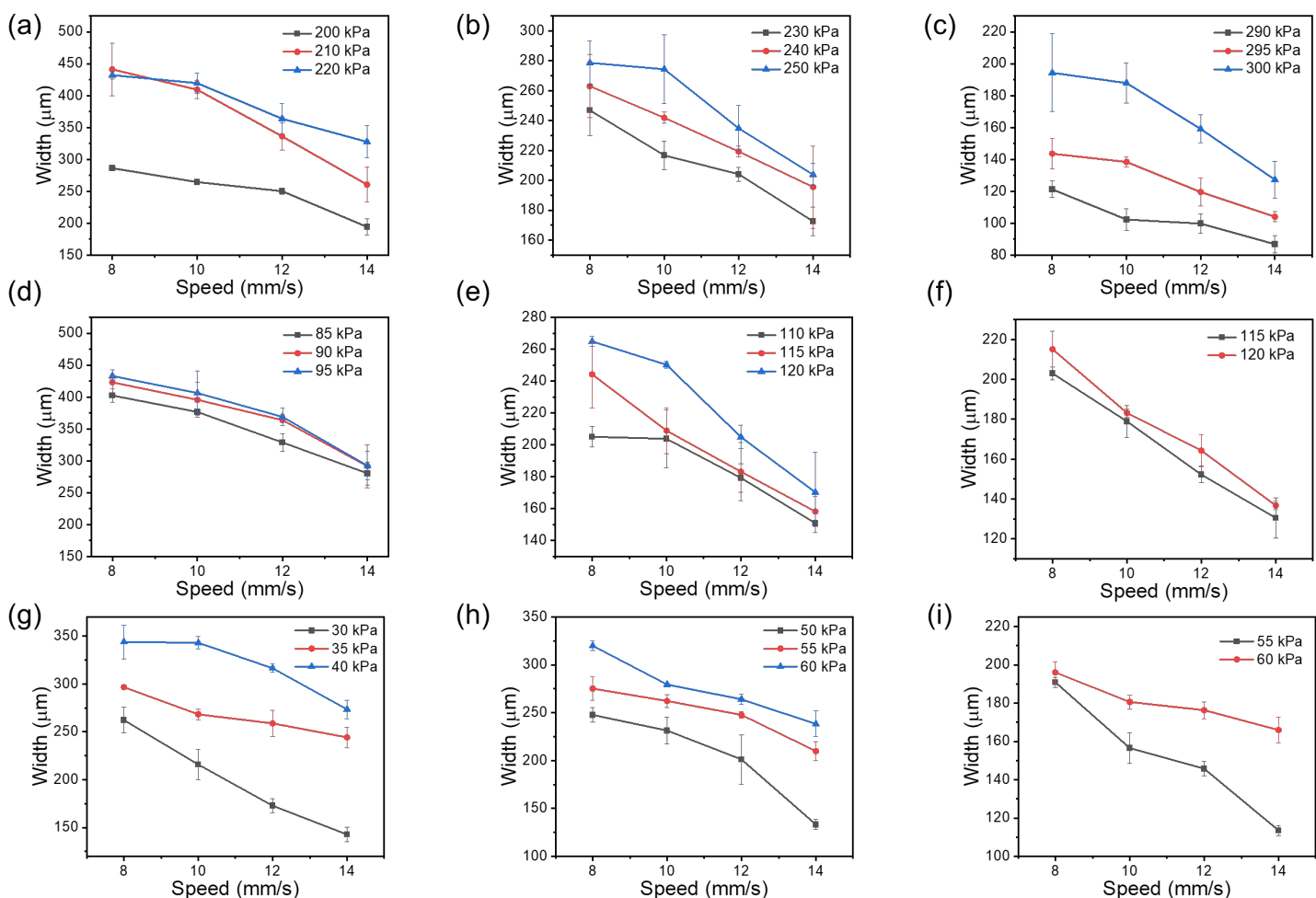


Figure 4-18. Printing optimization for the 3D printed MXene. a-c) The optimized resolution from 5 wt% concentration MXene with a nozzle size of 210 μm , 159 μm , and 108 μm . d-e) The optimized resolution from 4.5 wt% concentration MXene with a nozzle size of 210 μm , 159 μm , and 108 μm . g-i) The optimized resolution from 4 wt% concentration MXene with a nozzle size of 210 μm , 159 μm , and 108 μm .

4.3 Wearable MXene-based triboelectric nanogenerator (M-TENG)

As described in the previous section, MXene has a highly triboelectric negative surface due to the presence of fluorine and oxygen-containing terminal functional groups. When MXene couples

with materials with opposing triboelectric surfaces, triboelectric charges are generated from the contact and separation cycles. For wearable devices, a skin-like flexible substrate that can accommodate deformation during body movement should be used. Styrene-ethylene-butylene-styrene (SEBS) is ideal for the electric-skin, because it has a high stretching limit of up to 400% [143], accommodating many different deformations, and its triboelectric positive property allows electricity generation upon pairing with MXene (triboelectric negative).

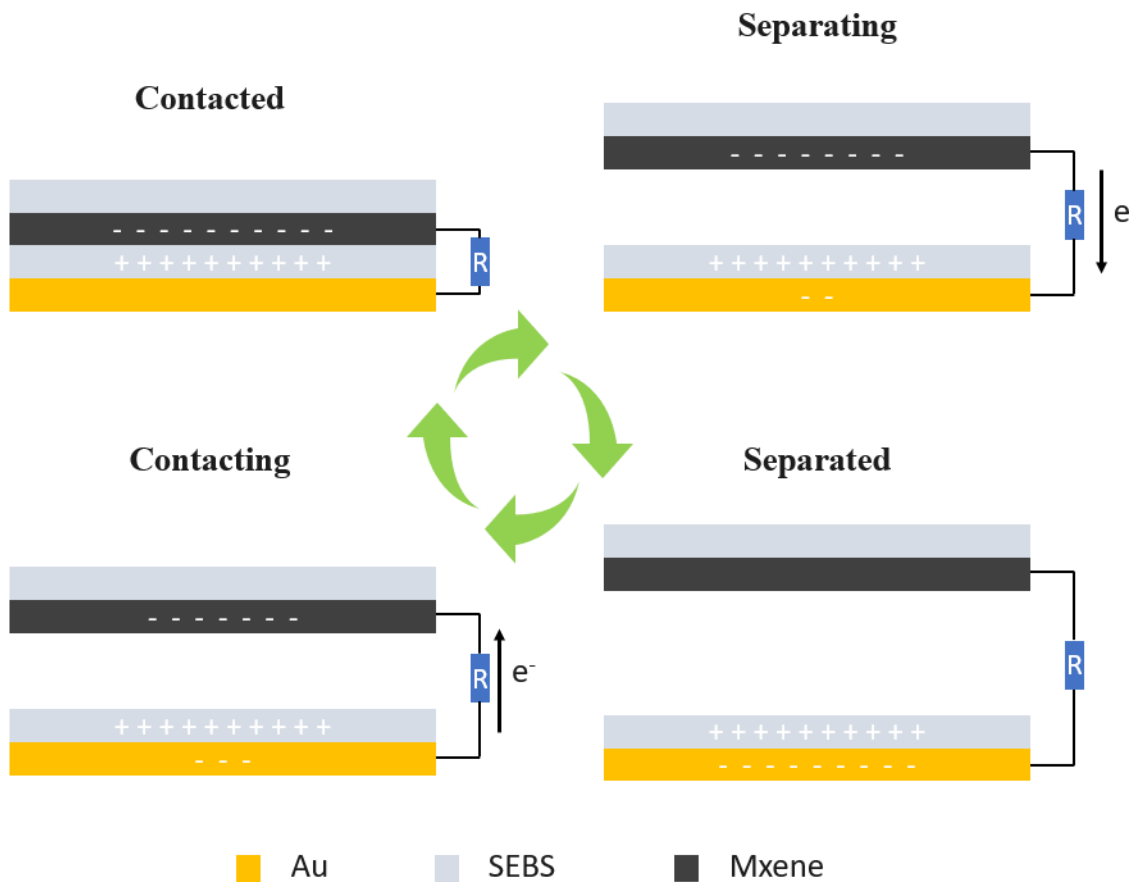


Figure 4-19. Working mechanism of power generation from M-TENG in contact-separation mode.

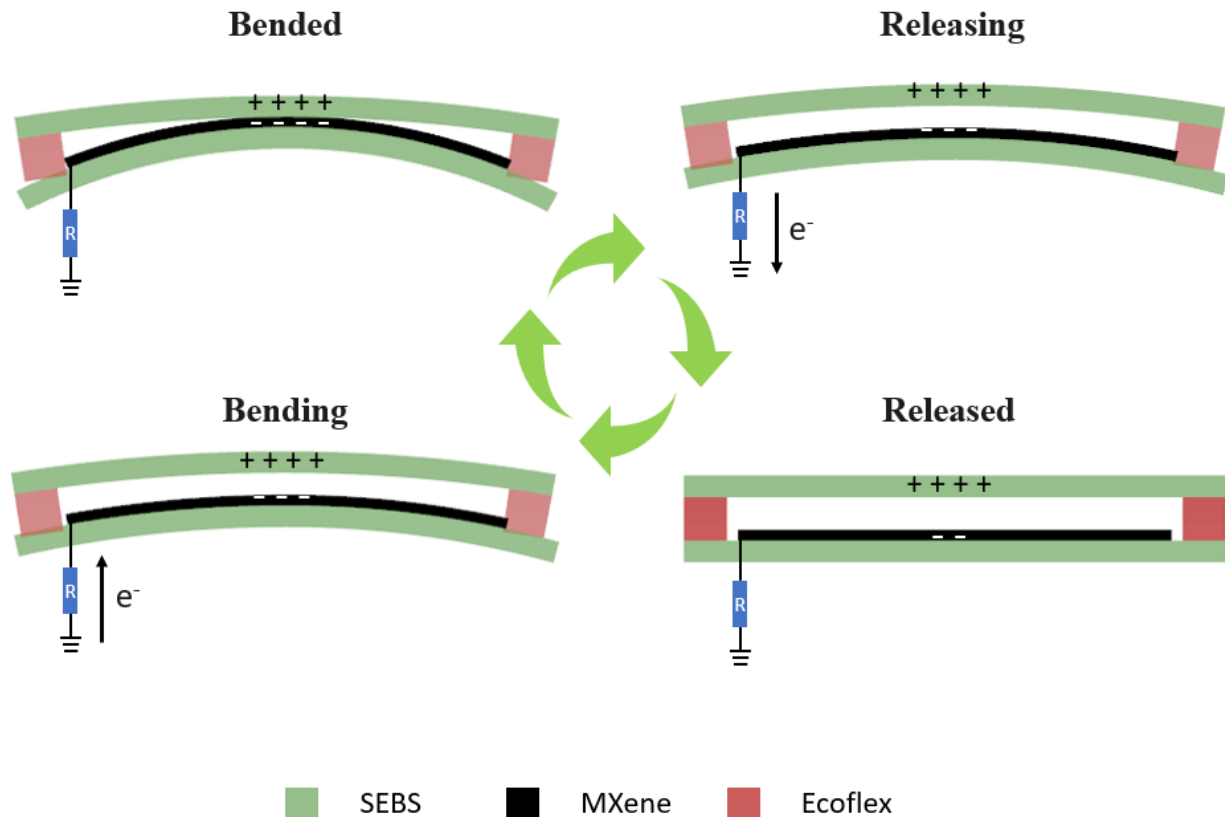


Figure 4-20. Working mechanism of power generation from the single-electrode M-TENG in bend-release mode

The working mechanism of the M-TENG in contact-separation mode and the single electrode M-TENG in bend-release mode are illustrated in Figure 4-19 and 4-20, respectively. In the initial stage, the triboelectric pair layers are separated and maintained in a neutral condition with no additional charges, in the contact-separation mode. When an external force is applied, triboelectric negative MXene is brought into contact with the triboelectric-positive SEBS, and electrons are transferred from SEBS to MXene. Upon separation, electrons on the conductive MXene film flow to the other electrode due to the edge electric field leakage effect, with the positive charges remaining on the surface of SEBS [144]. Electrons then flow back to the MXene film to balance the positive triboelectric charges on SEBS as the two films are brought into contact again.

Therefore, in the case of continuous contact and separation, alternating electrical signals are generated. The finite element method simulation (COMSOL Multiphysics) presented in Figure 4-21 & 4-22 further confirms the operation principle. The electrostatic potential distribution increases according to the separation distance.

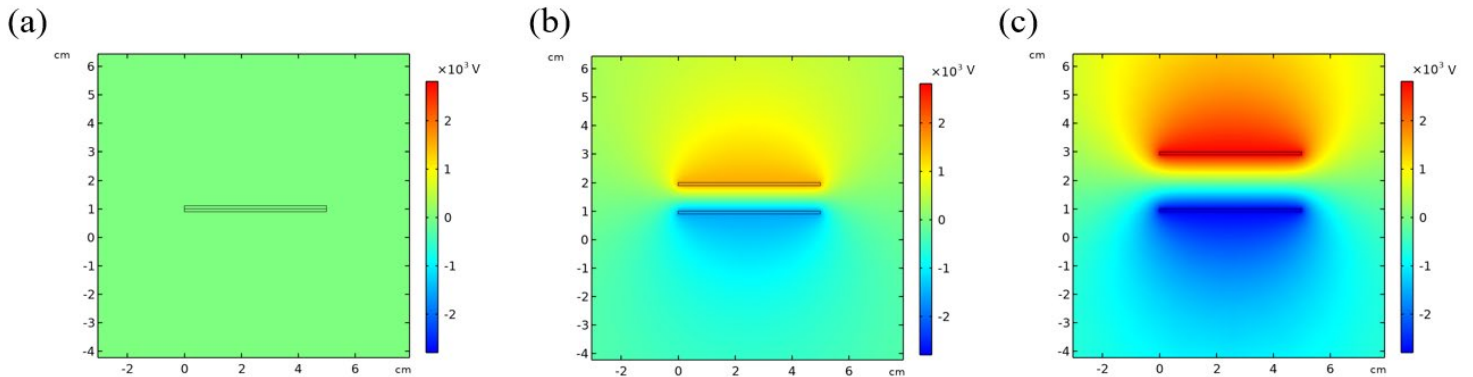


Figure 4-21. Finite-element simulation of the potential distribution between the electrodes in the TENG under the initial, separation, and separated conditions, respectively, performed using COMSOL Multiphysics.

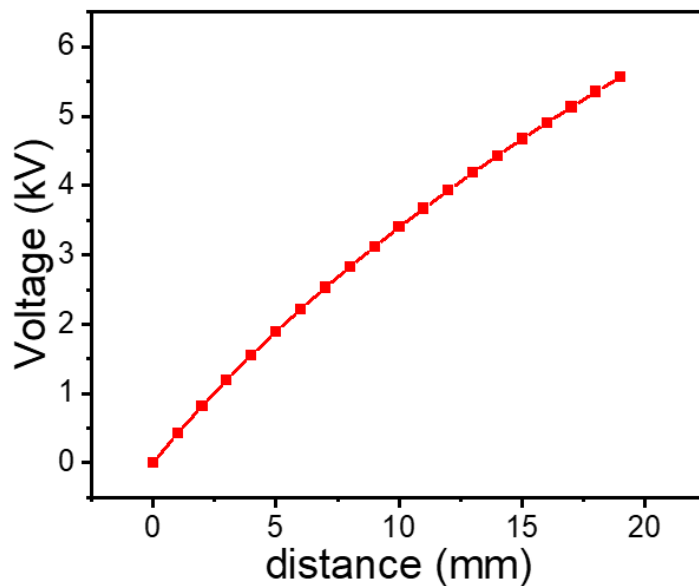


Figure 4-22. Simulation result for the potential difference over the change in the separation distance.

The power conversion performance of the energy harvester was evaluated. The contact-separation movement was controlled using a linear motor, and the open-circuit voltage (V_{oc}) profiles of the M-TENG at different working frequencies and applied forces were examined. As shown in Figure 4-23, the operation frequency gradually increased from 1 Hz to 12.5 Hz at a controlled applied force of 19.9 N. The output performance of the M-TENG first increased, and then settled at the frequency of 8 Hz, which can be attributed to surface charge accumulation on the triboelectric layer surface. However, increasing the frequency above 8 Hz prohibited neutralization of the accumulated charges. Similarly, as shown in Figure 4-24, the effect of the applied force was studied by gradually increasing the applied force from 5.2 N to 25.0 N at an operational frequency of 8 Hz. Greater force (i.e., 19.9 N) increased the output power, which was attributed to maximizing frictional contact on the MXene and SEBS surfaces. The optimum working conditions of 8 Hz and 19.9 N were maintained in subsequent experiments to determine the maximum output power for the fabricated M-TENG device.

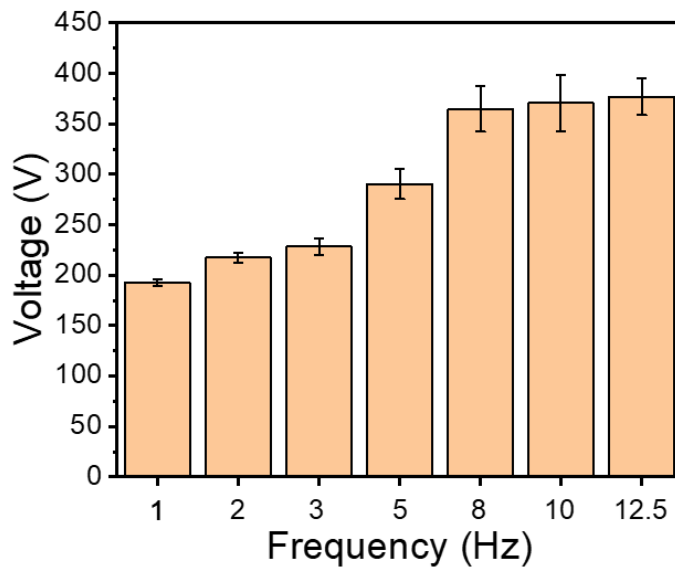


Figure 4-23. Output open circuit voltage of the M-TENG on various contact-separation frequencies when subjected to 19.9N.

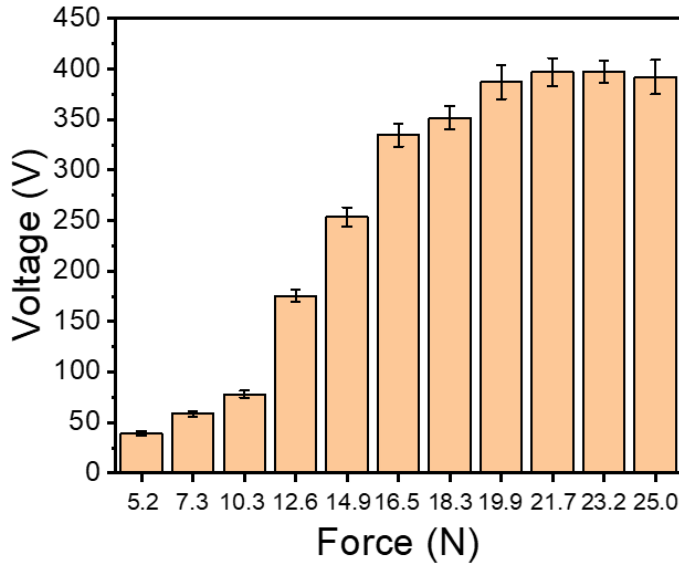


Figure 4-24. Output open circuit voltage of the M-TENG on various applied force when subjected to the operation frequency of $f = 8\text{Hz}$.

To investigate the M-TENG's maximum power output, its voltage, current, peak power, and peak power density performances were measured under a series of external loads. The output voltage increased with increasing external load, whereas the current followed a decreasing trend (Figure 4-25). The instantaneous power density of the M-TENG reached a maximum of 816.6 mW m^{-2} under a load resistance of $10^8 \Omega$ (Figure 4-26). Next, the charging efficiency performance for different energy-storage capacitance values was characterized. As shown in Figure 4-27, a full-wave rectifier was added to the circuit to convert the alternating current generated from the mechanical energy by M-TENG into direct current, which was stored in the capacitor. Charging efficiency was examined by quantifying the charging time of different capacitors. Capacitors of 1.0, 2.2, 4.7, and $10 \mu\text{F}$ were charged by finger tapping at the frequency of 3 Hz (convenient for one to perform). As seen in Figure 4-28, the storage voltage reached 3 V within 5 s for the $1 \mu\text{F}$

capacitor, and the 10 μF capacitor was charged to the same voltage within 50 s, indicating the reasonable charging capability of the M-TENG.

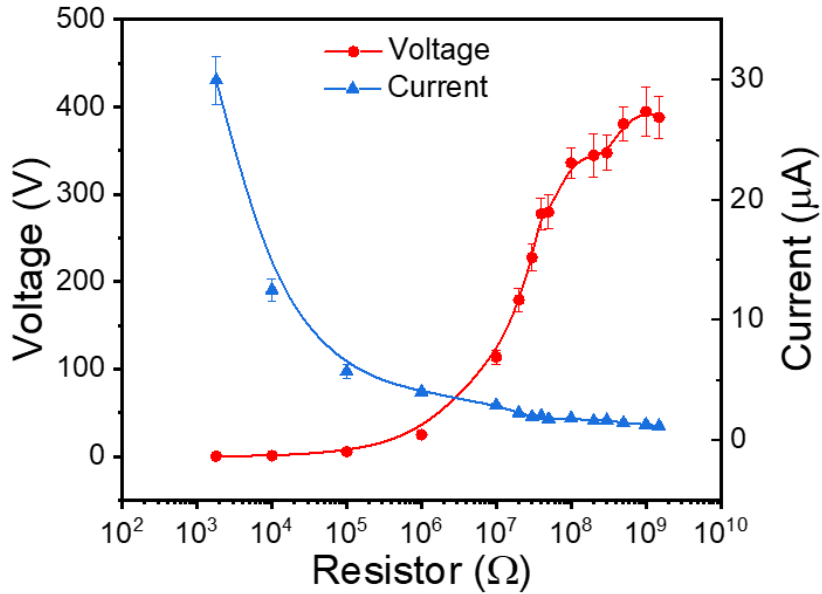


Figure 4-25. Output voltage and current of the M-TENG generated on contact-separation frequency of $f=8$ Hz with 19.9 N vertical force as a function of the load resistance.

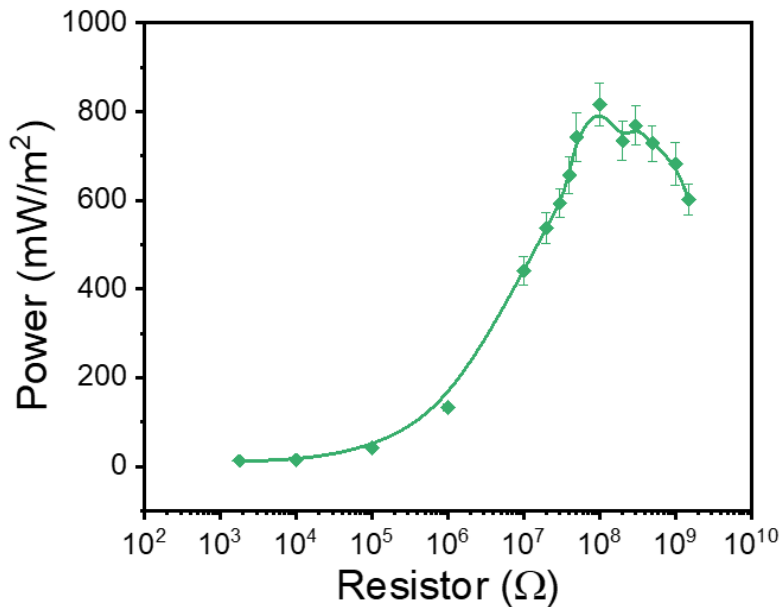


Figure 4-26. Instantiated output power of the M-TENG as a function of the load resistance.

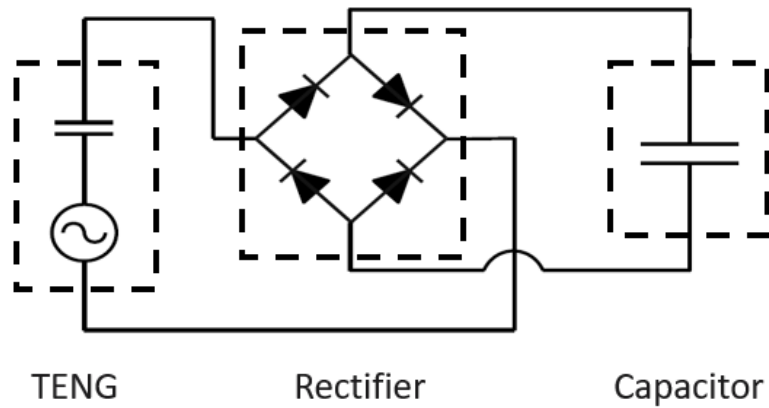


Figure 4-27. Schematic of the M-TENG with a rectifier circuit.

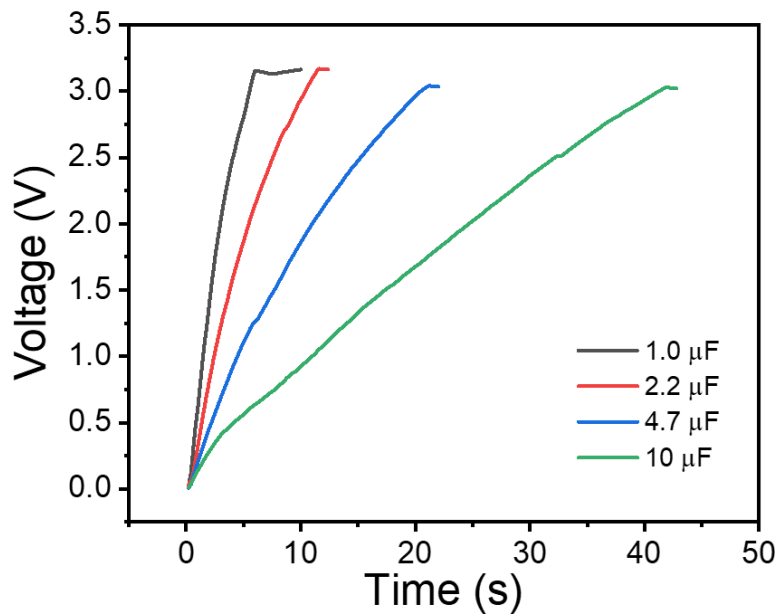


Figure 4-28. The capacitor voltage characteristic curves for various capacitors charged through the M-TENG

Additionally, the single electrode M-TENG is characterized. Given its thinness, the single-electrode M-TENG can be placed at locations with more significant curvature changes and thus harvest energy. As shown in Figure 4-29, with the increasing bending angle (30° , 60° , and 90°), the voltage output of the M-TENG increased gradually. This phenomenon may be the product of

the expanded contact area between the MXene and the SEBS, further promoting triboelectric charge generation. When attached to fingers or the inner elbow, as shown in Figure 4-30, the single electrode M-TENG harvested electricity from the bending of the arms and figures, and the energy increased with larger bending angles. Similar observations were reported by others [145]. However, according to our characterization experiments, the M-TENG in contact-separation mode produces a higher power intensity compared to the single-electrode M-TENG in bend-release mode. Subsequently, we implemented the M-TENG in the contact-separation mode in our MSP²S³.

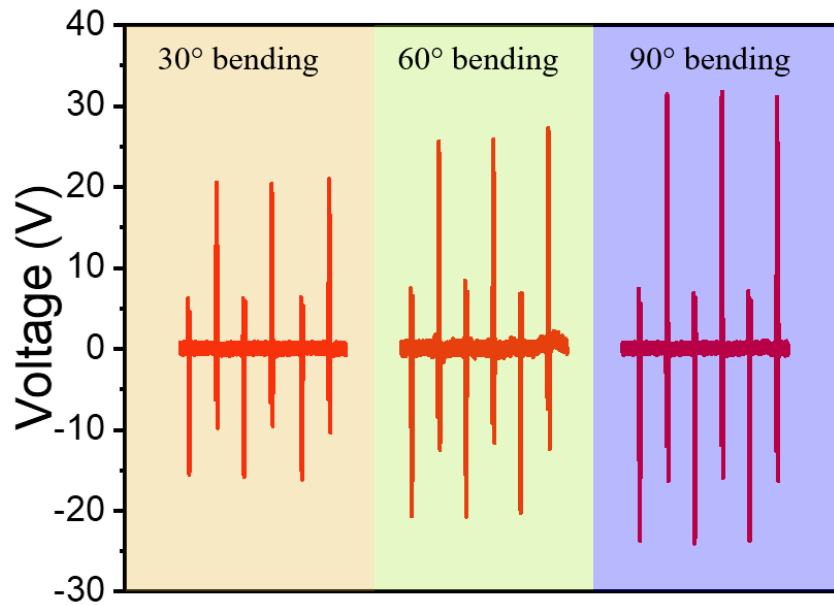


Figure 4-29. The voltage output characteristics of the single electrode M-TENG in response to bending at different bending angles of 30°, 60°, and 90° using a linear motor.

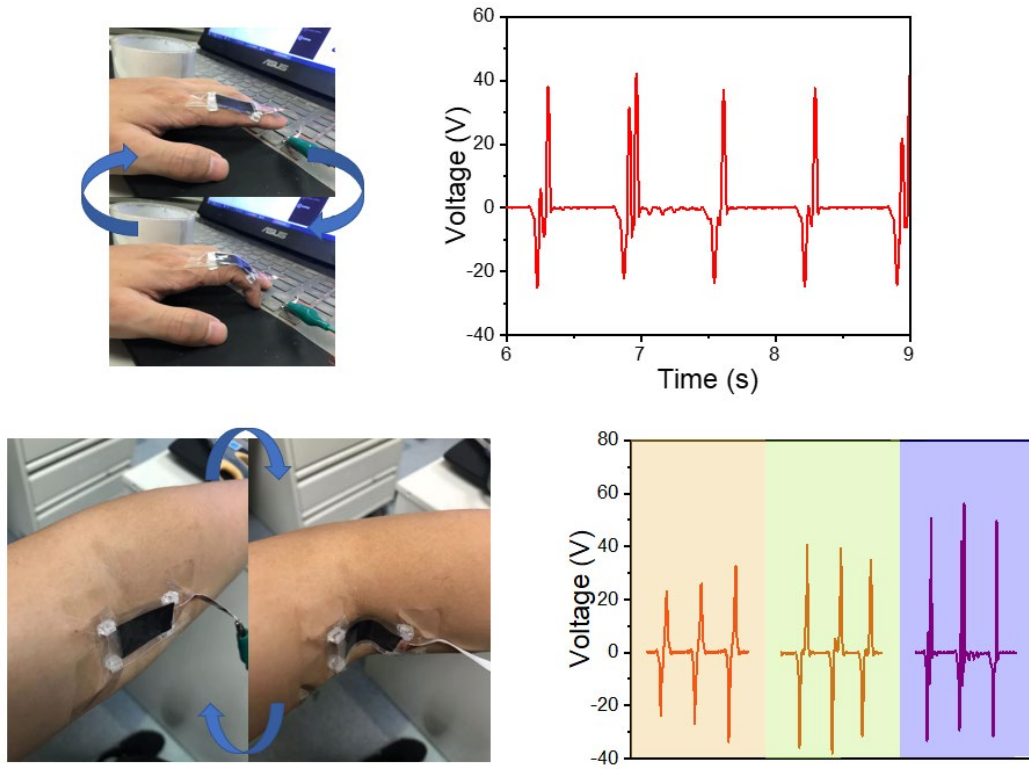


Figure 4-30. Voltage signal of the M-TENG in response to the continuous bend of the finger, and elbow.

4.4 Wearable MXene-based pressure sensor (M-PS)

Although the TENGs can be used as motion detection sensors [146], their lack of sensitivity hinders the detection of subtle physiological signals such as wrist pulses, which contain a wealth of health information. Therefore, highly sensitive sensors must be integrated into the self-powering systems. Among sensors developed to date, the capacitive-based pressure sensor offers high sensitivity [59], low power consumption [61], simple design [62], high immunity to environmental noise [63], and relatively fast response time [64] to external stimuli.

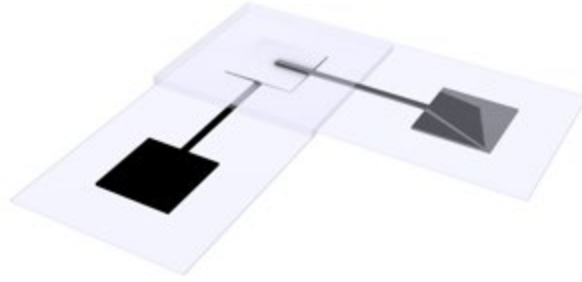


Figure 4-31. Schematic of the M-PS.

The structure of our MXene-based capacitive pressure sensor is illustrated in Figure 4-31. Epidermal SEBS was chosen as the sensor substrate for providing conformal contact to human skin, thus ensuring minimum signal attenuation and avoiding discomfort due to modulus mismatch with the skin. Conductive electrodes were fabricated via 3D-extrusion printing using MXene ink. The sandpaper-molded dielectric [EMI][TFSA]:PVDF layer was sandwiched between the two conducting MXene layers to enhance deformation under external pressure and further increase sensitivity. The sensitivity of the M-PS was characterized using a force gauge (applying external pressure) and an LCR meter (for reading capacitance changes) and quantified as the slope of its calibration curve .

$$S = \frac{d(\Delta C/C_0)}{d(\Delta P)} \quad (20)$$

As shown in Figure 4-32, the sensitivity of the M-PS was measured in two regions: S1 (6.03 kPa⁻¹) in the low-pressure region (0 – 4 kPa) and S2 (1.06 kPa⁻¹) in the high-pressure region (4 – 100 kPa). In the low-pressure region, even slight applied pressure induces a large deformation in the

dielectric material due to the highly porous sandpaper-imprinted structure, and the soft material property of [EMI][TFSA]: PVDF, which increases capacitance, yielding very high sensitivity. In the high-pressure region, the deformation of the micro-structured layer is almost saturated because of the reduction in porosity, increasing the stiffness of the polymer, thus sensitivity was compromised compared with the low-pressure region.

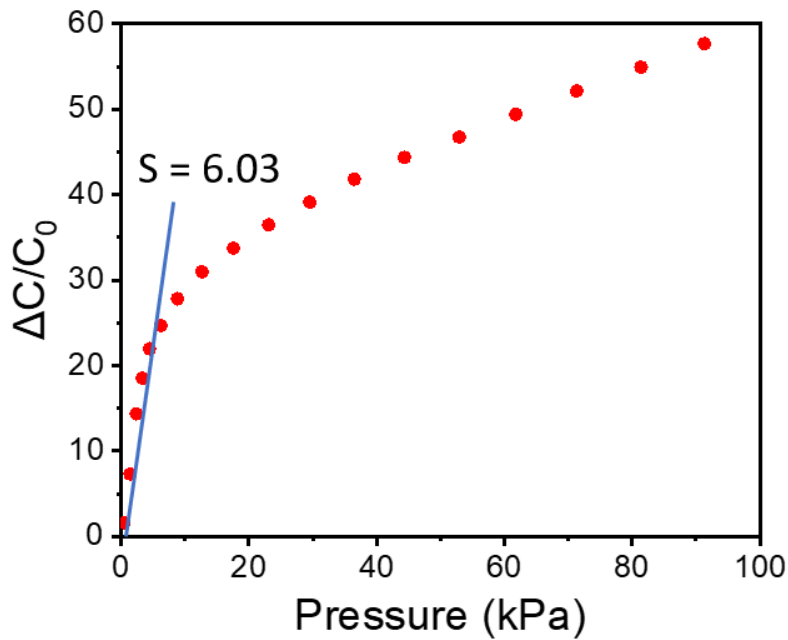


Figure 4-32. Characteristic curve for the M-pressure sensor, showing the relative change in capacitance with respect to different external pressures.

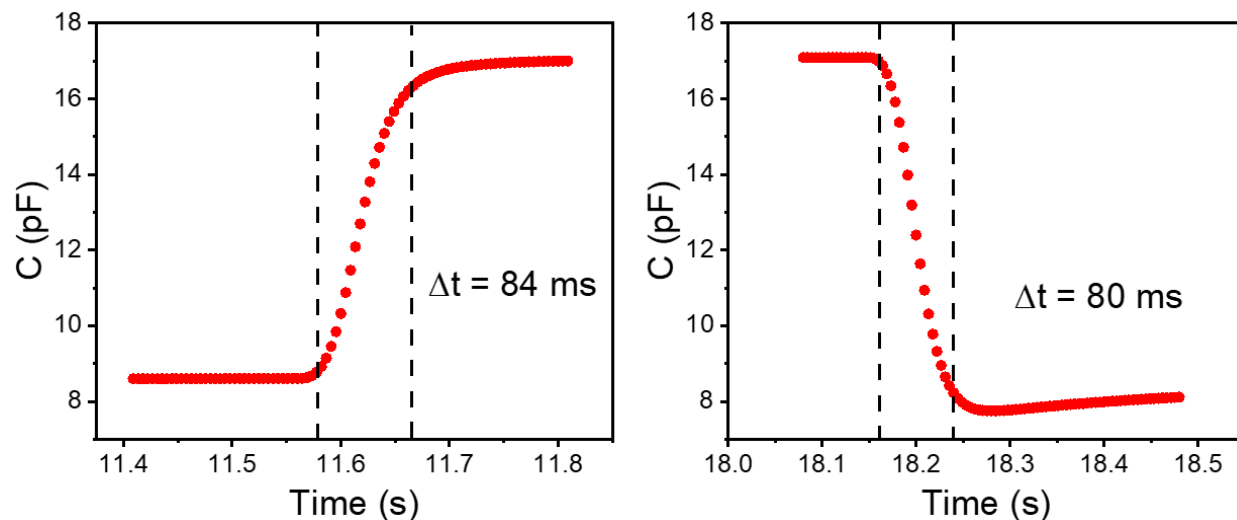


Figure 4-33. The response time and relaxation time of the M-PS.

The response and relaxation times of the fabricated sensor were evaluated under the pressure of ~ 1 kPa (Figure 4-33). A dynamic response time of 84 ms and a relaxation time of 80 ms were achieved; this suggests that the time for elastic recovery for [EMI][TFSA]: PVDF polymer is the same as that for compression, indicating negligible hysteresis. Moreover, the limit of detection (LOD) for minute pressure was characterized by investigating the sensor's response under the applied pressure of a water droplet ($12 \mu\text{L}$, ~ 0.009 kPa). The sensor was fixed to a stage and connected to the measurement circuit of an LCR meter. After obtaining a stable baseline, water droplets were dispensed onto M-PS. As shown in Figure 4-34, M-PS exhibited high sensitivity to external ultra-low load by detecting a single water droplet ($12 \mu\text{L}$, ~ 0.009 kPa). The change in the capacitance corresponding to the introduction of each droplet was identical, indicating the linear behavior of the M-PS in a low-pressure regime.

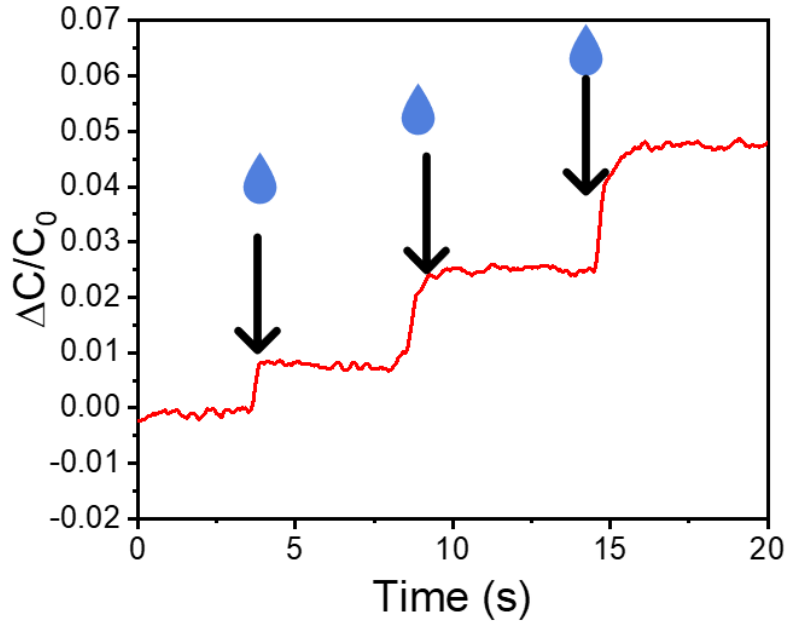


Figure 4-34. The minute pressure response from applying droplets of water.

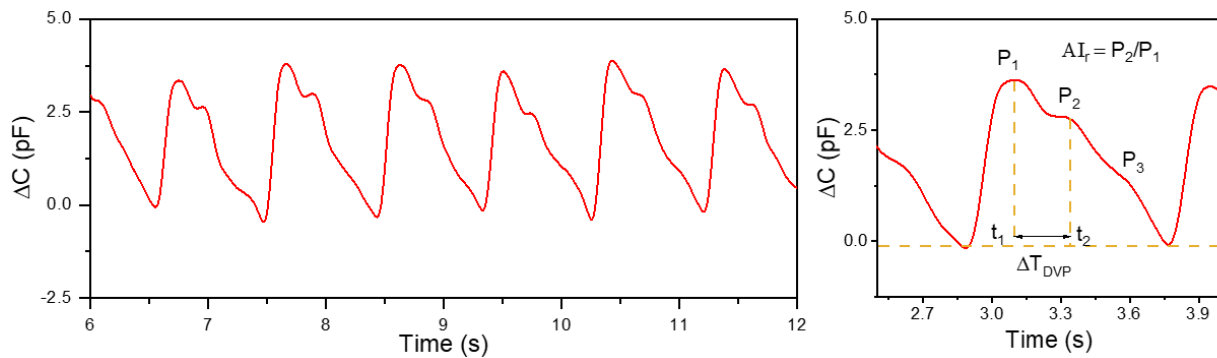


Figure 4-35. Left: The actual pulse signal collected from the M-pressure sensor. Right: The enlarged view for one specific pulse shows the three typical peaks of the wrist pulse.

Besides its outstanding performance in the detection of minute pressure, the sensor's application in real-time pulse monitoring was also demonstrated. The sensor was attached to the wrist of a 28-year-old healthy male volunteer using double-sided medical tape, and the pulse signal was continuously recorded for 45 seconds. The real-time wrist pulse signal results obtained by the M-PS are shown in Figure 4-35. In the detailed characteristics of a single RAP waveform, an incident

wave generated by blood flow (P_1), the late systolic shoulder (P_2), and another tiny reflection wave (P_3) originating from the lower body were clearly visible, demonstrating precise signal monitoring. Radial artery augmentation index and the associated time delay defined as $AI_r = P_2/P_1$ and $\Delta T_{DVP} = t_2 - t_1$, respectively, are commonly employed for estimating the physiological condition of the human cardiovascular system. The results revealed the two parameters AI_r and ΔT_{DVP} as 0.761 and 0.235 s, respectively, which were representative values for a healthy young man (0.695 ± 0.163) [147]. The long-time monitoring result shown in Figure 4-36 indicated that the pulse rate was 70, which is also within the expected range for a healthy young man (60 – 100 bpm) [96]. The results confirm that the proposed M-PS can identify subtle differences in the wrist pulse, provide useful information regarding the cardiovascular system, and affirm the potential in practical applications.

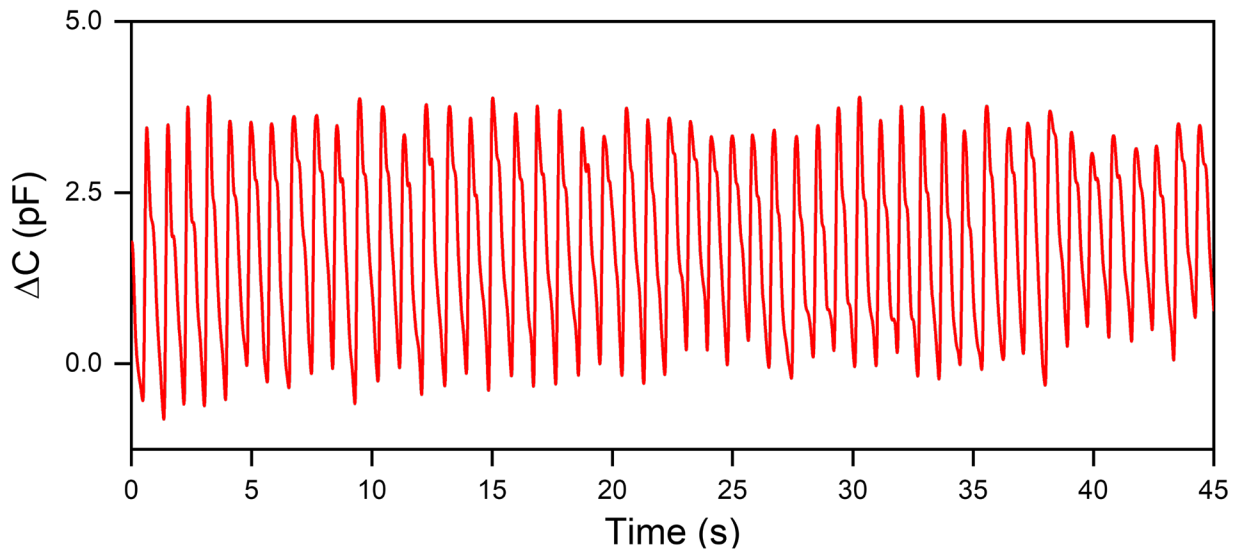


Figure 4-36. The entire radial artery pressure waveform over the recording period of 45 seconds.

4.5 *In-situ* demonstration of the wearable MXene-based self-powered physiological signal sensing system (MSP²S³)

For the practical application of real-time and continuous physiological signal monitoring powered by biomechanical energy, the utility of the MSP²S³ was demonstrated. In terms of design, the structure of the self-powered MSP²S³ consists of i) three M-TENGs to produce power, ii) custom-designed circuitry on a flexible printed circuit board (FPCB) for power management, energy storage, and data collection, visualization, and wireless data transmission, iii) an M-PS for RAP measurements. As shown in the circuit diagram in Figure 4-37, biomechanical energy from finger tapping is first converted to electricity by the M-TENG. Next, the generated AC current is rectified to DC using full-wave rectifiers and stored in the capacitors on the FPCB. As described above, the MSP²S³ is designed to work in two modes. In mode one, the stored energy powers the CDC chip which communicates with the M-PS to measure RAPs in real-time and controls an LED to flash at a rate indicating the measured pulse rate during the active data recording. In mode two, the detailed measured RAP waveforms are wirelessly transmitted to a smartphone through the NFC technology for further analysis and possible detection of abnormalities.

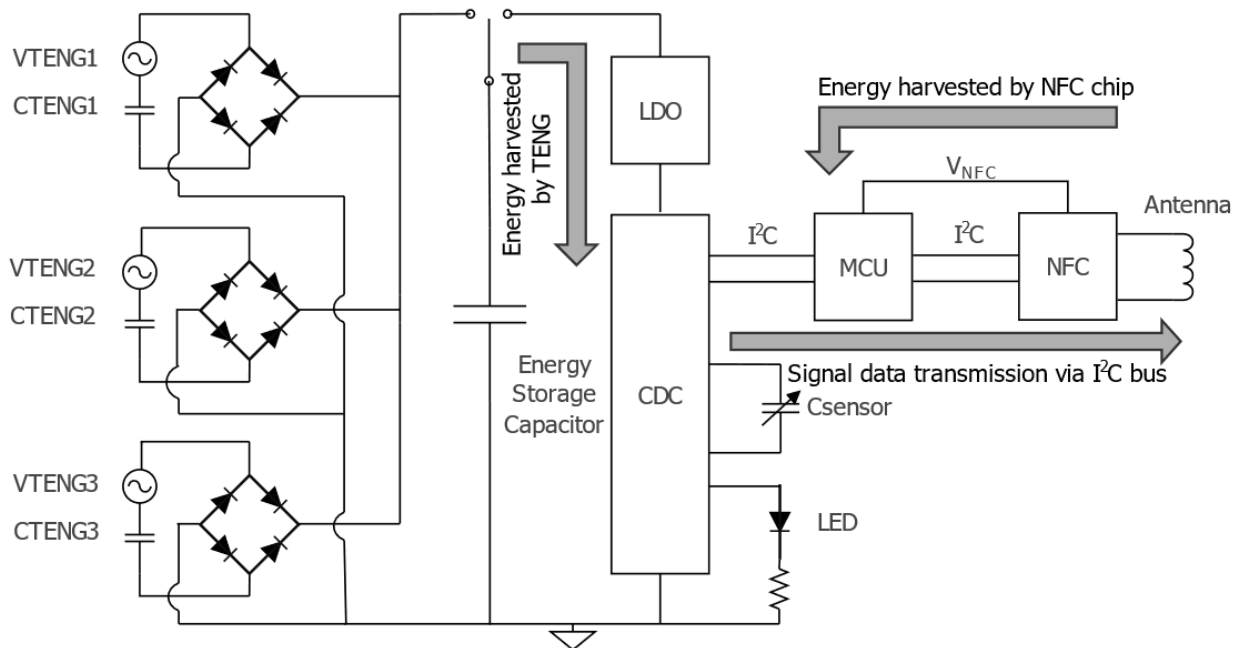


Figure 4-37. Circuit diagram for the MSP²S³ including the M-TENGs, power management circuitry, energy storing circuitry, data collection, and wireless data/power transmission modules.

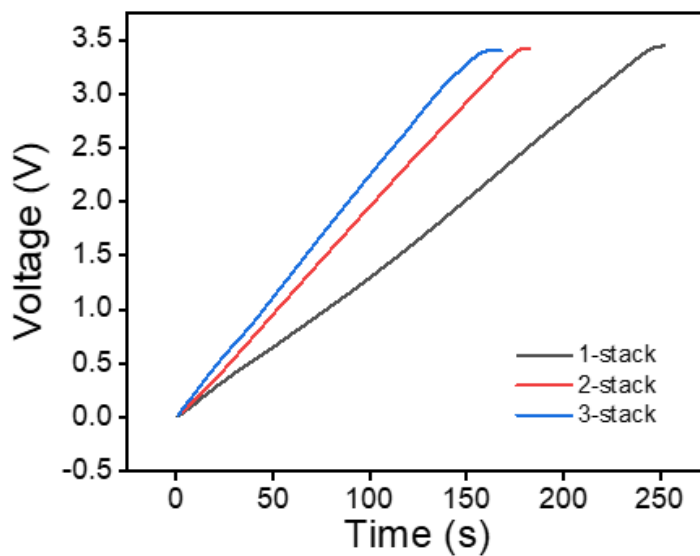


Figure 4-38. The charging capability with different stacks of the M-TENG.

Here, to enhance the MSP²S³ performance, two main parameters needed to be considered: increasing the power generation efficiency and minimizing power consumption. For the first

parameter, we employed a more extensive panel area and multiple stacks of M-TENGs. The charging performance of the M-TENGs at the frequency of ~3 Hz with various numbers of parallel stacks was recorded (Figure 4-38). While for a single stack M-TENG, ~252 seconds was needed to charge a capacitor at 3.4 V, this time was reduced to ~ 180 seconds and 154 seconds in two-stack and three-stack M-TENGs, respectively. However, as more stacks of M-TENGs are incorporated, more MXene layers are necessary to attenuate under the same applied force, which did not lead to a linear improvement of the charging rate. For the second consideration, we reduced the power consumption at the system design level by adding a low-dropout regulator (LDO) to control power consumption and extend operation time per charging phase. This LDO maintains the operating current <math><50 \mu\text{A}</math> to allow the CDC chip and LED to operate while avoiding power wastage.

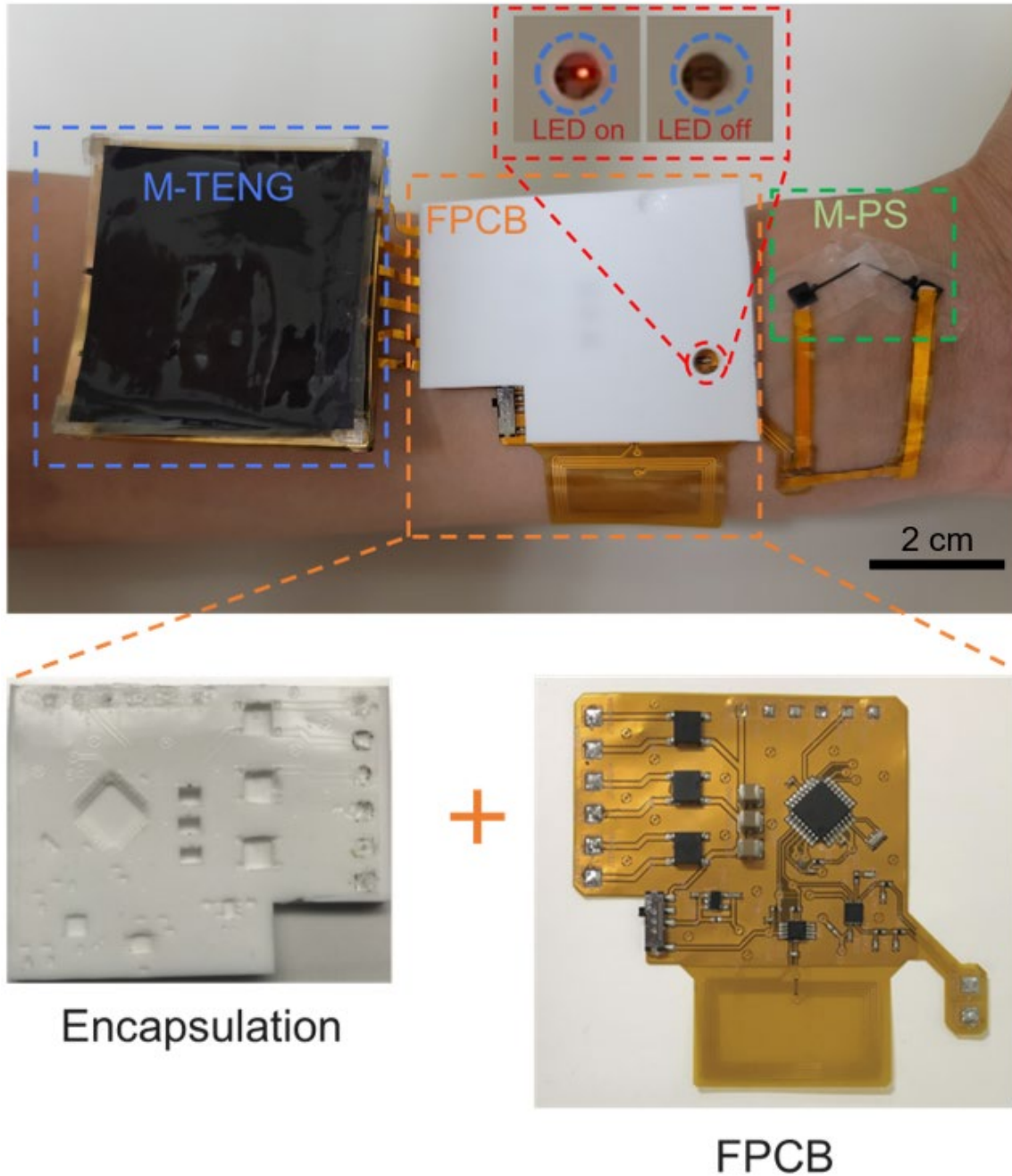


Figure 4-39. Optical image of the wearable MSP²S³. The inset “on” and “off” status of the LED, respectively, represent the valley and peak of the pulse signal detected by the MSP²S³ in mode one.

Next, we demonstrated the utility of MSP²S³ for *in-situ* and the real-time RAP monitoring in mode one to show the RAP peak rates with the LED. The MSP²S³ was first attached to a volunteer’s arm

and set to the charging phase (Figure 4-39). The user was asked to start finger tapping the M-TENGs to charge the storage capacitor, then switch the device to powering phase to power the CDC chip, M-PS sensor, and the LED. Subsequently, the LED began to flash, with “on” and “off” states representing the valleys and peaks of the RAP waveform, respectively.

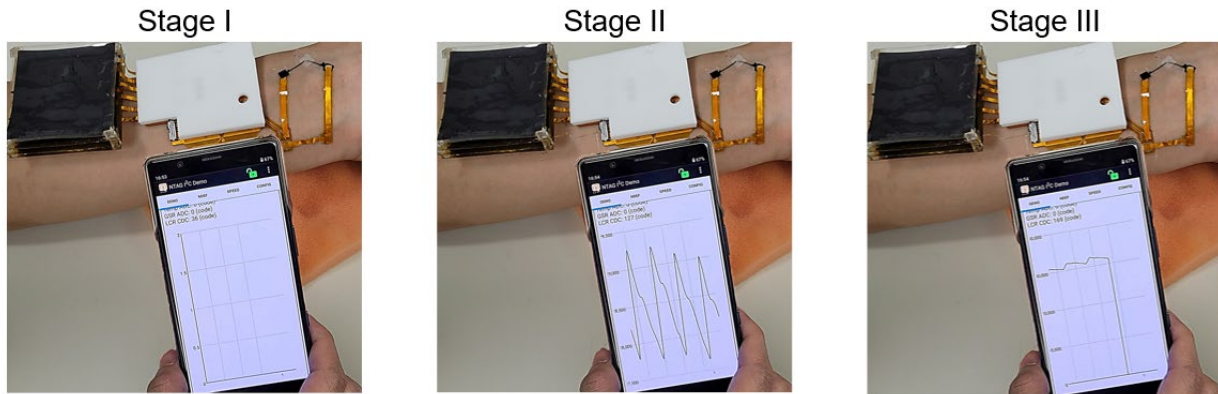


Figure 4-40. The real-time pulse data monitored using MSP²S³ in mode two, displayed in the customized App.

The utility of MSP²S³ in mode two was also demonstrated. As explained before, the M-TENG still powers the CDC chip, M-PS sensor, and LED in this mode. However, the NFC chip and MCU are now wirelessly powered by a phone to extract the measured RAP data directly from the CDC chip and wirelessly transmit the data to the phone for analysis and real-time plotting on a custom-made Android App. As shown in Figure 4-40, after the charging phase and making sure the phone is near to the NFC antenna for power and data transmission, a line with a value of zero first appears on the App, because the CDC chip is not still powered. By switching the MSP²S³ from the charging phase to the powering phase, it starts to power the CDC chip and M-PS sensor to collect the RAP waves, while the NFC chip wirelessly transmits the data to the phone for display. Eventually, the

storage capacitors run out of power, stopping power flow to the CDC chip and M-PS sensor. The NFC chip reads and transmits the null value again, as shown in Figure 4-40 (right). One should note that recharging (tapping) and powering phases can be repeated to measure RAP waves over any period of time. In addition, wirelessly transmitted RAP data can be further analyzed to extract more details about the waveforms. For instance, in RAP waves P_1 , P_2 , and P_3 in Figure 4-41, the two principal parameters of AI_r and ΔT_{DVP} can be extracted as 0.725 and 0.20s, respectively. Throughout this work, the RAP data collected by the MSP²S³ were always cross-validated with commercially available tools (e.g., an impedance spectroscope). One should note all sets of data were collected from healthy volunteers with no known cardiovascular disease problems in this work. Additionally, as a possible future development of the work, implementation of a fully automated MSP²S³ can be considered in which the devices can automatically switch between two different modes, leading to minimizing user involvement and potentially enabling continuous and real-time biosignals collection without interruptions.

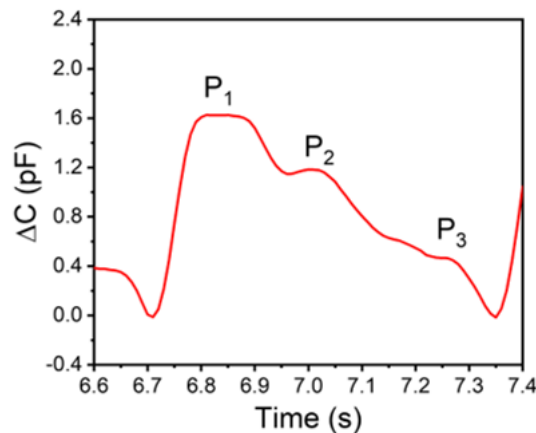


Figure 4-41. The enlarged view for one specific pulse, showing the typical three peaks of a single wrist RAP pulse.

4.6 Summary

In summary, a novel, flexible, wearable 3D-printed MXene-based self-powered and wireless sensing system has been developed for physiological signal monitoring. With seamless integration of M-TENG, M-PS, and multifunctional circuitry, power is generated from mechanical motion and efficiently applied for continuous and real-time RAP wave monitoring. MXene has a high triboelectric negative property and exhibits a high output power of 816.6 mW m^{-2} when coupled with the SEBS in the M-TENG. Moreover, with modifications, the MXene demonstrated a threefold improvement in conductivity and tunable viscoelastic property favored for 3D printing. The M-PS of the proposed MSP²S³ system showed a high sensitivity of 6.03 kPa^{-1} and a fast response time of 80 ms, enabling the capture of subtle changes in transient biosignals.

The utility of the MSP²S³ for on-demand, continuous, real-time, and self-powered RAP monitoring was demonstrated, as was the implementation of wireless power and RAP waveform transmission via NFC technology. To the best of our knowledge, this is the first fully integrated, triboelectrically-driven, self-powered, battery-free, wireless, MXene-based wearable sensing system for continuous and real-time physiological signal monitoring powered by human motion. Such devices represent an exciting potential for the future of wearable health monitoring devices.

4.7 Materials and methods

3D printable MXene ink preparation: MAX phase particle selection: Ti₃AlC₂ MAX phase powder (2 g, <40 μm particle size, NANOCHEMAZONE) was dispersed in 40 ml of water by magnetic stirring for 10 min. The mixture was left to stand for 3.5 minutes to separate MAX phase particles with a diameter larger than 10 μm by sedimentation. The relationship between the practical size and the sedimentation time is governed by the equation below:

$$v = \frac{2(\rho_p - \rho_f)gR^2}{9\mu} \quad (21)$$

Where v is the sedimentation speed, g is the gravitational acceleration, R is the radius of the spherical particle, ρ_p is the mass density of the MAX phase particles, ρ_f is the mass density of water, and μ is the dynamic viscosity of water. After the sedimentation process, the top supernatant containing suspended small MAX phase particles was decanted from the sediment, and the sediment was dispersed in 40 ml deionized (DI) water again for another cycle. The entire process was repeated three times with the same conditions to thoroughly remove small particles. The collected sediment was dried under vacuum at room temperature (25 °C) for 12 h before being used for synthesis.

Material synthesis: 1.6 g lithium fluoride (LiF, 99%, Sigma Aldrich) was dissolved in 20 ml of 9 M hydrochloric acid (HCl) by magnetic stirring for 10 min. 1 g of size-selected MAX phase powder was then gradually added to the pre-mixed etching solution over 10 minutes. The MAX phase etching process was carried out at 50 °C for 30 h. After the reaction was completed, the resulting dispersion was washed with DI water by repeated centrifugation at 2,700 rpm (1,345 rcf) for 5 min per cycle until self-delamination occurred at a supernatant pH of ~6. The self-delaminated MXene flakes were then collected by centrifugation at 1,180 rpm (247 rcf) for 30 min. The dark green supernatant was collected and further centrifuged at 3,500 rpm (2,223 rcf) for 20 min; the sediment containing large MXene flakes was collected for use as ink for extrusion 3D printing without any other process.

Preparation and optimization of $Ti_3C_2T_x$ MXene 3D extrusion printing: Viscosity-tunable ink was achieved by adding and evaporating the water content in the ink mixture, and the weight was

measured at each stage to achieve different ink concentrations (4, 4.5, and 5 wt%). The flexible MXene film was directly printed using a commercial 3D extrusion printer (Incredible+, Cellink Inc.) on the styrene-ethylene-butylene-styrene (SEBS) substrate. The as-printed film was further annealed at 80 °C for 30 min.

M-TENG fabrication: MXene film was printed on the flexible SEBS substrate. The conductive (copper foil/gold-coated film) trace was connected to the MXene film with silver epoxy, then encapsulated and protected by the Ecoflex 00-30 (Smooth-On, PA). 4 PDMS spacers (2 mm × 2 mm × 4 mm) were attached to the corners of the SEBS substrate with adhesive gels, and the other piece of the SEBS layer was attached to the top of the spacer with the same gel, and the gel was cured at room temperature for 24 hours.

M-PS fabrication: Wearable M-PS was made starting from the MXene printing on the SEBS substrate. The dielectric layer was formed by spin coating intronic material [EMI][TFSA]: PVDF onto 200-grit sandpaper and annealing at 100 °C for 30 minutes. The structured dielectric was peeled away from the sandpaper mold and sandwiched between the MXene/SEBS conducting panel, forming the capacitive pressure sensor.

FPCB design and fabrication: The FPCB consists of a microcontroller (ATmega328P, Microchip), an NFC transducer (NT3H2111, NXP), an CDC chip (AD7156, Analog Devices), and some passive components. All the Integrated Circuits (ICs) and passive components are in small packages and sizes to increase compactness. A low-temperature solder paste (SMDLTLFPT5, CHIPQUIK) was brushed onto the pads using a stencil. ICs and components were placed on the solder paste by hand and soldered by the reflow process. A customized Android app was developed to wirelessly communicate with the FPCB and analyze the data.

Characterization: A field emission electron microscope (SEM, Hitachi 4700) was used to study the powder morphology and flake size distribution. MXene powder samples were prepared by vacuum filtration, and the flake samples were prepared by ink dilution and drop cast onto the silicon wafer. The flake size distribution was measured in 200 flakes out of 5 different SEM images ($150\ \mu\text{m} \times 100\ \mu\text{m}$ for the large flake samples, and $1.8\ \mu\text{m} \times 1.2\ \mu\text{m}$ for the small flake samples) from the four corners and the center of the wafer. X-ray diffraction (XRD) patterns of the MAX phase and synthesized MXene were obtained using an X-ray Diffractometer (Rigaku Smartlab), equipped with Cu K α radiation (40 kV, 44 mA) with an X-ray wavelength (λ) of 1.54 Å. Fourier transform infrared (FTIR) spectroscopy was used to characterize the functional groups on the surface of the synthesized MXene. Electrical conductivity measurements of the MXene ink during different treatments were conducted by using an LCR meter (GW Instek LCR-819), and the value was calculated from the obtained resistance and the filament geometry from the 3D printed patterns (n=5).

$$\sigma = \frac{l}{w \times t \times R_0} \quad (22)$$

Where w and t are the width and thickness of the printed line structure, respectively, l is the length, R_0 is the sample resistance, and σ is the sample conductivity. A linear motor (PS01-23X80R, Linmot) was used for frequency and force control during the M-TENG characterization. The open-circuit voltage and short-circuit current were recorded by using a potentiostat (Versastat 3). The output power under different external loads was calculated from the corresponding voltage and resistance. The M-PS sensitivity characterization was performed using a force gauge connected to the LCR meter, the force was applied from 0 N to 22.4 N, and the force was further converted to pressure ($P = F/A$). The response time, relaxation time, and *in-situ* characterization of the pressure sensor were measured by an impedance spectroscopy (HF2IS, Zurich instrument) under

the operation frequency of 100 kHz, and voltage of 1 V with the sampling rate of 225 samples/sec. A custom-made MATLAB code was used to process the impedance data obtained to the capacitance value. COMSOL Multiphysics software was used for the simulation of the TENG performance.

Chapter V. Conclusion

In this dissertation, different nano materials have been developed for different functional devices in the application for the wearable healthcare industry. A physics-based model was developed first to understand printing behavior of the material, to get a precise control of printing filament in terms of the various printing parameters, including the printing pressure, print head moving speed, material viscosity, dispensing needle size, etc. The entire printing section has been separated into two part, the material extrusion from the dispensing needle, and the material deposition onto the print bed. In the material extrusion part, the material flow inside the dispensing needle is the dominant factor, the flow behavior of the material plays a critical role. The Reynold number, which is the gold standard for classification of the flow behavior has been applied in this scenario. Random printing parameters have been generated, and the line filament has been printed to check the printing quality and resolution. As a result, a distribution of different Reynold number with their printing results has been collected. It is clear to see that within the low Reynold number region, a controllable and uniform printing was obtained. As the Reynold number increased, the probability of the occurrence of the uniform or uncontrollable printing was getting increased, and finally reached to 100% after certain threshold. This observation is in accordance with the description of Reynold number. In the second part, the material deposition, the competing mechanism becomes the average extrusion velocity and the print bed moving velocity. While the extrusion speed was larger than the moving speed, materials will pile up, and an overflow or over-stacked filament was observed. While the extrusion speed was smaller than the moving speed, filament stretching was occurred and result in a non-uniform filament. Only when the extrusion speed was similar to the moving speed, a uniform result was obtained. Even though the physics have been well studied for the pneumatic printing process. However, there are some non-idealities

exist during the entire process, such as the gap between the nozzle and the substrate, the pure equation can not fully predict the resolution of the printed filament. To solve this problem, we are going to incorporate the concept of physic-guided machine learning. Training the physics derivative mathematical model and the boundary conditions with the mass printed data, the actual hidden relationship between the printing parameters to the printing resolution can be discovered without the mandatory requirement of a massive amount of data.

Next, the RAP signal collection was studied. In order to collect such subtle signal, a high sensitivity is needed for the sensing devices. By well control of the printing path by the knowledge of the printing behavior from different printing parameters, a microcylinder structure was successfully developed from 3D printing, instead of the widely used method by nanofabrication. In addition, a 3D printable supporting PDMS material and conductive 3D printable CNT+PDMS material were also developed. As a result, a highly sensitive, robust, flexible, biocompatible, hybrid, and rapidly integrable multi-material all-3D-printed nanocomposite-based (M2A3DNC) wearable pressure sensors were successfully demonstrated. It offers a low detection limit (~ 0.009 kPa), high-pressure sensitivity (0.512 kPa⁻¹), fast response time, distortion resistivity, and high durability (1,600 cycles compression). Notably, the utility of the M2A3DNC pressure sensors for a wide range of applications in wearable personalized health monitoring, including respiratory rate monitoring, artery pulse recording, vocal cord vibration pattern detection. It is worth noting that the advantages of accomplishment of structural engineering in multilayer 3D printing are not limited to wearable sensors for the healthcare industry. It also paves a new pathway for advances in robotics tactile sensing, human-machine interface, and more other applications are remained to be explored.

At last, another key consideration in the wearable electronics industry has been taken into account, the power supply. Traditional method for the power supply is the batteries. However, it has a series

of disadvantages for the future generation of wearable sensors for on-demand, continuous, real-time recording of the transient physiological biosignal. Triboelectric nanogenerator was our solution. However, the TENG itself does not possess enough sensitivity, and the other reported TENG powering system was limited to recording discrete data points, minutes apart, and incapable of continuous monitoring of transient physiological biosignals. In our innovation, a novel, self-powered, "all-in-one", MXene-based, 3D-printed, and integrated wearable sensing system for on-demand, continuous, and real-time vital signal monitoring. 2D MXene is one of the promising materials with a good triboelectric property. By the modification of the preparation process, a 3D printable MXene ink was developed for the TENG powering system. With seamless integration of M-TENG, M-PS, and multifunctional circuitry, power is generated from mechanical motion and efficiently applied for continuous and real-time RAP wave monitoring. MXene has a high triboelectric negative property and exhibits a high output power of 816.6 mW m^{-2} when coupled with the SEBS in the M-TENG. Moreover, with modifications, the MXene demonstrated a threefold improvement in conductivity and tunable viscoelastic property favored for 3D printing. The M-PS of the proposed MSP^2S^3 system showed a high sensitivity of 6.03 kPa^{-1} and a fast response time of 80 ms, enabling the capture of subtle changes in transient biosignals.

The utility of the MSP^2S^3 for on-demand, continuous, real-time, and self-powered RAP monitoring was demonstrated, as was the implementation of wireless power and RAP waveform transmission via NFC technology. To the best of our knowledge, this is the first fully integrated, triboelectrically-driven, self-powered, battery-free, wireless, MXene-based wearable sensing system for continuous and real-time physiological signal monitoring powered by human motion. Such devices represent an exciting potential for the future of wearable health monitoring devices.

This dissertation demonstrates the potential of applying different nanomaterials in 3D printing, by using the simple material and a simpler method, cheap, reliable, multi-functional wearable sensor and wearable sensing platform can be easily fabricated for human health monitoring.

Bibliography

1. Bandonkar, A.J., I. Jeerapan, and J.J.A.S. Wang, *Wearable chemical sensors: Present challenges and future prospects*. 2016. **1**(5): p. 464-482.
2. Xu, S., et al., *Soft microfluidic assemblies of sensors, circuits, and radios for the skin*. 2014. **344**(6179): p. 70-74.
3. Huang, X., et al., *Stretchable, wireless sensors and functional substrates for epidermal characterization of sweat*. 2014. **10**(15): p. 3083-3090.
4. Chen, K., et al., *Printed carbon nanotube electronics and sensor systems*. 2016. **28**(22): p. 4397-4414.
5. Tee, B.C.-K., et al., *A skin-inspired organic digital mechanoreceptor*. 2015. **350**(6258): p. 313-316.
6. Nag, A., S.C. Mukhopadhyay, and J.J.I.S.J. Kosel, *Wearable flexible sensors: A review*. 2017. **17**(13): p. 3949-3960.
7. Mathew, A.A., A. Chandrasekhar, and S.J.N.E. Vivekanandan, *A review on real-time implantable and wearable health monitoring sensors based on triboelectric nanogenerator approach*. 2021. **80**: p. 105566.
8. Nasiri, S., M.R.J.S. Khosravani, and A.A. Physical, *Progress and challenges in fabrication of wearable sensors for health monitoring*. 2020. **312**: p. 112105.
9. Guo, J., et al., *Stretchable and temperature - sensitive polymer optical fibers for wearable health monitoring*. 2019. **29**(33): p. 1902898.
10. Yang, J., et al., *Flexible, tunable, and ultrasensitive capacitive pressure sensor with microconformal graphene electrodes*. 2019. **11**(16): p. 14997-15006.
11. Curto, V.F., et al., *Real-time sweat pH monitoring based on a wearable chemical barcode microfluidic platform incorporating ionic liquids*. 2012. **171**: p. 1327-1334.

12. Gao, W., et al., *Wearable microsensor array for multiplexed heavy metal monitoring of body fluids*. 2016. **1**(7): p. 866-874.
13. Miller, D.J., et al., *Analyzing changes in respiratory rate to predict the risk of COVID-19 infection*. 2020. **15**(12): p. e0243693.
14. Zhou, Y., et al., *Delivery of miR-424-5p via Extracellular vesicles promotes the apoptosis of MDA-MB-231 TNBC cells in the tumor microenvironment*. 2021. **22**(2): p. 844.
15. Ligon, S.C., et al., *Polymers for 3D printing and customized additive manufacturing*. 2017. **117**(15): p. 10212-10290.
16. Peng, X., et al., *Integrating digital light processing with direct ink writing for hybrid 3D printing of functional structures and devices*. 2021. **40**: p. 101911.
17. Zhang, B., et al., *Mechanically robust and UV - curable shape - memory polymers for digital light processing based 4D printing*. 2021. **33**(27): p. 2101298.
18. Zhu, G., et al., *Digital light processing 3D printing of healable and recyclable polymers with tailorable mechanical properties*. 2021. **13**(29): p. 34954-34961.
19. Zhang, Y., et al., *Predictive manufacturability assessment system for laser powder bed fusion based on a hybrid machine learning model*. 2021. **41**: p. 101946.
20. Anelli, S., et al., *Hybrid-3D printing of symmetric solid oxide cells by inkjet printing and robocasting*. 2022: p. 102636.
21. Dumpa, N., et al., *3D printing in personalized drug delivery: An overview of hot-melt extrusion-based fused deposition modeling*. 2021. **600**: p. 120501.
22. Placone, J.K. and A.J.J.A.h.m. Engler, *Recent advances in extrusion - based 3D printing for biomedical applications*. 2018. **7**(8): p. 1701161.
23. Zhang, S., et al., *3D - printed wearable electrochemical energy devices*. 2022. **32**(3): p. 2103092.

24. Jammalamadaka, U. and K.J.J.o.f.b. Tappa, *Recent advances in biomaterials for 3D printing and tissue engineering*. 2018. **9**(1): p. 22.
25. Yi, Q., et al., *All - 3D - Printed, Flexible, and Hybrid Wearable Bioelectronic Tactile Sensors Using Biocompatible Nanocomposites for Health Monitoring*. 2021: p. 2101034.
26. Mousavi, S., et al., *Direct 3D printing of highly anisotropic, flexible, constriction-resistive sensors for multidirectional proprioception in soft robots*. 2020. **12**(13): p. 15631-15643.
27. Seol, M.-L., et al., *All 3D printed energy harvester for autonomous and sustainable resource utilization*. 2018. **52**: p. 271-278.
28. Bruneaux, J., et al., *Micro-extrusion of organic inks for direct-write assembly*. 2008. **18**(11): p. 115020.
29. Cheng, J., et al., *Rheological properties of cell-hydrogel composites extruding through small-diameter tips*. 2008. **130**(2).
30. Lee, J.M., W.Y.J.V. Yeong, and P. Prototyping, *A preliminary model of time-pressure dispensing system for bioprinting based on printing and material parameters: This paper reports a method to predict and control the width of hydrogel filament for bioprinting applications*. 2015. **10**(1): p. 3-8.
31. Suntornnond, R., et al., *A mathematical model on the resolution of extrusion bioprinting for the development of new bioinks*. 2016. **9**(9): p. 756.
32. Khalil, S., W.J.M.S. Sun, and E. C, *Biopolymer deposition for freeform fabrication of hydrogel tissue constructs*. 2007. **27**(3): p. 469-478.
33. Amorim, P.A., et al., *Insights on shear rheology of inks for extrusion-based 3D bioprinting*. Bioprinting, 2021: p. e00129.
34. Abdel-Hamid, S.M., et al., *Formulation of an antispasmodic drug as a topical local anesthetic*. 2006. **326**(1-2): p. 107-118.

35. Chhabra, R.P. and J.F. Richardson, *Non-Newtonian flow and applied rheology: engineering applications*. 2011: Butterworth-Heinemann.
36. Sukindar, N.A., et al., *Analyzing the effect of nozzle diameter in fused deposition modeling for extruding polylactic acid using open source 3D printing*. 2016. **78**(10).
37. Fieselmann, J.F., et al., *Respiratory rate predicts cardiopulmonary arrest for internal medicine inpatients*. *Journal of general internal medicine*, 1993. **8**(7): p. 354-360.
38. Cretikos, M., et al., *The objective medical emergency team activation criteria: a case-control study*. *Resuscitation*, 2007. **73**(1): p. 62-72.
39. Yang, J., et al., *Flexible, tunable, and ultrasensitive capacitive pressure sensor with microconformal graphene electrodes*. *ACS applied materials & interfaces*, 2019. **11**(16): p. 14997-15006.
40. Chen, S., et al., *Multi-sized Planar Capacitive Pressure Sensor with Ultra-high Sensitivity*. *Nano Energy*, 2021: p. 106178.
41. Li, T., et al., *Flexible capacitive tactile sensor based on micropatterned dielectric layer*. *Small*, 2016. **12**(36): p. 5042-5048.
42. Nie, B., et al., *Flexible transparent iontronic film for interfacial capacitive pressure sensing*. *Advanced Materials*, 2015. **27**(39): p. 6055-6062.
43. Pang, C., et al., *Highly skin - conformal microhairy sensor for pulse signal amplification*. *Advanced materials*, 2015. **27**(4): p. 634-640.
44. Hwang, J., et al., *Fabrication of hierarchically porous structured PDMS composites and their application as a flexible capacitive pressure sensor*. *Composites Part B: Engineering*, 2021. **211**: p. 108607.

45. Park, J., et al., *Giant tunneling piezoresistance of composite elastomers with interlocked microdome arrays for ultrasensitive and multimodal electronic skins*. ACS nano, 2014. **8**(5): p. 4689-4697.
46. Sheng, L., et al., *Bubble - decorated honeycomb - like graphene film as ultrahigh sensitivity pressure sensors*. Advanced Functional Materials, 2015. **25**(41): p. 6545-6551.
47. Bae, G.Y., et al., *Linearly and highly pressure - sensitive electronic skin based on a bioinspired hierarchical structural array*. Advanced Materials, 2016. **28**(26): p. 5300-5306.
48. Marlinda, A.R., et al., *Simple dispersion of graphene incorporated rubber composite for resistive pressure sensor application*. Polymer Engineering & Science, 2021. **61**(5): p. 1476-1484.
49. Atitallah, B.B., et al., *Piezo-Resistive Pressure and Strain Sensors for Biomedical and Tele-Manipulation Applications*. Advanced Sensors for Biomedical Applications, 2021: p. 47-65.
50. Wu, W., X. Wen, and Z.L.J.S. Wang, *Taxel-addressable matrix of vertical-nanowire piezotronic transistors for active and adaptive tactile imaging*. Science, 2013. **340**(6135): p. 952-957.
51. Ha, M., et al., *Bioinspired interlocked and hierarchical design of ZnO nanowire arrays for static and dynamic pressure - sensitive electronic skins*. Advanced Functional Materials, 2015. **25**(19): p. 2841-2849.
52. Zhong, Q., et al., *Paper - Based Active Tactile Sensor Array*. Advanced Materials, 2015. **27**(44): p. 7130-7136.
53. Tan, Y., et al., *High-performance textile piezoelectric pressure sensor with novel structural hierarchy based on ZnO nanorods array for wearable application*. Nano Research, 2021: p. 1-8.
54. Wang, S., et al., *Boosting piezoelectric response of PVDF-TrFE via MXene for self-powered linear pressure sensor*. Composites Science and Technology, 2021. **202**: p. 108600.
55. Fan, F.-R., et al., *Transparent triboelectric nanogenerators and self-powered pressure sensors based on micropatterned plastic films*. Nano letters, 2012. **12**(6): p. 3109-3114.

56. Lin, L., et al., *Triboelectric active sensor array for self-powered static and dynamic pressure detection and tactile imaging*. ACS nano, 2013. **7**(9): p. 8266-8274.
57. Goh, Q.L., et al., *Self-powered pressure sensor based on microfluidic triboelectric principle for human-machine interface applications*. Smart Materials, 2021. **30**(7): p. 075012.
58. Lei, H., et al., *Advances in self-powered triboelectric pressure sensors*. Journal of Materials Chemistry A, 2021.
59. Qiu, J., et al., *Rapid-response, low detection limit, and high-sensitivity capacitive flexible tactile sensor based on three-dimensional porous dielectric layer for wearable electronic skin*. ACS applied materials & interfaces, 2019. **11**(43): p. 40716-40725.
60. Gao, L., et al., *Highly Sensitive Pseudocapacitive Iontronic Pressure Sensor with Broad Sensing Range*. Nano-micro letters, 2021. **13**(1): p. 1-14.
61. Yamazaki, H., et al., *A review of capacitive MEMS hydrogen sensor using Pd - based metallic glass with fast response and low power consumption*. Electronics Communications in Japan, 2019. **102**(3): p. 70-77.
62. Ruth, S.R.A., et al., *Rational design of capacitive pressure sensors based on pyramidal microstructures for specialized monitoring of biosignals*. Advanced Functional Materials, 2020. **30**(29): p. 1903100.
63. Iqbal, J., et al. *Long range, high sensitivity, low noise capacitive sensor for tagless indoor human localization*. in *2017 7th IEEE International Workshop on Advances in Sensors and Interfaces (IWASI)*. 2017. IEEE.
64. He, Z., et al., *Capacitive pressure sensor with high sensitivity and fast response to dynamic interaction based on graphene and porous nylon networks*. ACS applied materials & interfaces, 2018. **10**(15): p. 12816-12823.

65. Kim, K., et al., *Highly Sensitive and Wearable Liquid Metal - Based Pressure Sensor for Health Monitoring Applications: Integration of a 3D - Printed Microbump Array with the Microchannel*. *Advanced healthcare materials*, 2019. **8**(22): p. 1900978.
66. Samad, Y.A., et al., *Novel graphene foam composite with adjustable sensitivity for sensor applications*. *ACS applied materials & interfaces*, 2015. **7**(17): p. 9195-9202.
67. Zhu, G.-J., et al., *A highly sensitive and broad-range pressure sensor based on polyurethane mesodome arrays embedded with silver nanowires*. *ACS applied materials & interfaces*, 2020. **12**(17): p. 19988-19999.
68. Liang, Y., et al., *PEDOT: PSS - Based Bioelectronic Devices for Recording and Modulation of Electrophysiological and Biochemical Cell Signals*. *Advanced Healthcare Materials*, 2021: p. 2100061.
69. Gao, M., L. Li, and Y.J.J.o.M.C.C. Song, *Inkjet printing wearable electronic devices*. *Journal of Materials Chemistry C*, 2017. **5**(12): p. 2971-2993.
70. Yang, W., et al., *A breathable and screen - printed pressure sensor based on nanofiber membranes for electronic skins*. *Advanced Materials Technologies*, 2018. **3**(2): p. 1700241.
71. Jang, S., et al., *Printable wet-resistive textile strain sensors using bead-blended composite ink for robustly integrative wearable electronics*. *Composites Part B: Engineering*, 2021. **210**: p. 108674.
72. Zhang, D., et al., *Fabrication of highly conductive graphene flexible circuits by 3D printing*. *Synthetic Metals*, 2016. **217**: p. 79-86.
73. Zhu, Z., H.S. Park, and M.C.J.S.a. McAlpine, *3D printed deformable sensors*. *Science advances*, 2020. **6**(25): p. eaba5575.
74. Gao, Y., et al., *Laser micro-structured pressure sensor with modulated sensitivity for electronic skins*. *Nanotechnology* 2019. **30**(32): p. 325502.

75. Peng, S., et al., *Rational design of ultrasensitive pressure sensors by tailoring microscopic features*. *Advanced Materials Interfaces*, 2018. **5**(18): p. 1800403.
76. Wei, Y., et al., *Cu–Ag core–shell nanowires for electronic skin with a petal molded microstructure*. *Journal of Materials Chemistry*, 2015. **3**(37): p. 9594-9602.
77. Xu, M., et al., *Flexible pressure sensor using carbon nanotube-wrapped polydimethylsiloxane microspheres for tactile sensing*. *Sensors and Actuators A: Physical*, 2018. **284**: p. 260-265.
78. Kim, J.-O., et al., *Highly ordered 3d microstructure-based electronic skin capable of differentiating pressure, temperature, and proximity*. *ACS applied materials & interfaces*, 2018. **11**(1): p. 1503-1511.
79. Tee, B.C.K., et al., *Tunable flexible pressure sensors using microstructured elastomer geometries for intuitive electronics*. *Advanced Functional Materials*, 2014. **24**(34): p. 5427-5434.
80. Emon, M.O.F., et al., *Multi-material 3D printing of a soft pressure sensor*. *Additive Manufacturing*, 2019. **28**: p. 629-638.
81. Tang, Z., et al., *3D printing of highly sensitive and large-measurement-range flexible pressure sensors with a positive piezoresistive effect*. *ACS applied materials & interfaces*, 2020. **12**(25): p. 28669-28680.
82. Xia, T., et al., *Ultrahigh Sensitivity Flexible Pressure Sensors Based on 3D - Printed Hollow Microstructures for Electronic Skins*. *Advanced Materials Technologies*, 2021. **6**(3): p. 2000984.
83. Lind, J.U., et al., *Instrumented cardiac microphysiological devices via multimaterial three-dimensional printing*. *Nature materials*, 2017. **16**(3): p. 303-308.
84. Chu, M., et al., *Respiration rate and volume measurements using wearable strain sensors*. 2019. **2**(1): p. 1-9.

85. Ren, M., et al., *Highly stretchable and durable strain sensor based on carbon nanotubes decorated thermoplastic polyurethane fibrous network with aligned wave-like structure*. 2019. **360**: p. 762-777.
86. Dąbrowska, A., et al., *Materials used to simulate physical properties of human skin*. 2016. **22**(1): p. 3-14.
87. Wang, Z., A.A. Volinsky, and N.D.J.J.o.A.P.S. Gallant, *Crosslinking effect on polydimethylsiloxane elastic modulus measured by custom - built compression instrument*. 2014. **131**(22).
88. Park, S., et al., *Silicones for stretchable and durable soft devices: Beyond Sylgard-184*. 2018. **10**(13): p. 11261-11268.
89. Cai, L. and C.J.N.r.l. Wang, *Carbon nanotube flexible and stretchable electronics*. 2015. **10**(1): p. 1-21.
90. Park, Y.-L., et al., *Hyperelastic pressure sensing with a liquid-embedded elastomer*. 2010. **20**(12): p. 125029.
91. Wang, Z., A.A. Volinsky, and N.D. Gallant, *Crosslinking effect on polydimethylsiloxane elastic modulus measured by custom-built compression instrument*. *Journal of Applied Polymer Science*, 2014. **131**(22).
92. O'Mahony, C., et al., *Determination of thermal and thermomechanical properties of biodegradable PLA blends: for additive manufacturing process*. *Journal of Thermal Analysis*, 2020. **142**: p. 715-722.
93. Du, J., et al., *Optimized CNT-PDMS flexible composite for attachable health-care device*. 2020. **20**(16): p. 4523.
94. Pang, Y., et al., *Flexible, highly sensitive, and wearable pressure and strain sensors with graphene porous network structure*. *ACS applied materials & interfaces* 2016. **8**(40): p. 26458-26462.

95. LoMauro, A. and A.J.B. Aliverti, *Sex differences in respiratory function*. *Breathe*, 2018. **14**(2): p. 131-140.
96. *Vital Signs (Body Temperature, Pulse Rate, Respiration Rate, Blood Pressure)*. 2021 [cited 2021 July]; Available from: <https://www.hopkinsmedicine.org/health/conditions-and-diseases/vital-signs-body-temperature-pulse-rate-respiration-rate-blood-pressure>.
97. Kim, J., et al., *Wearable biosensors for healthcare monitoring*. 2019. **37**(4): p. 389-406.
98. Song, Y., et al., *Wireless battery-free wearable sweat sensor powered by human motion*. 2020. **6**(40): p. eaay9842.
99. Ray, T.R., et al., *Bio-integrated wearable systems: a comprehensive review*. 2019. **119**(8): p. 5461-5533.
100. Yang, C., et al., *Integrated Strain Sensors with Stretchable Vertical Graphene Networks for Non-invasive Physiological Assessment*. 2022. **4**(3): p. 964-973.
101. Hozumi, S., et al., *Multimodal wearable sensor sheet for health-related chemical and physical monitoring*. 2021. **6**(5): p. 1918-1924.
102. Mazzaracchio, V., et al., *Medium-distance affordable, flexible and wireless epidermal sensor for pH monitoring in sweat*. 2021. **222**: p. 121502.
103. Huang, Z., et al., *An ultrasensitive aptamer-antibody sandwich cortisol sensor for the noninvasive monitoring of stress state*. 2021. **190**: p. 113451.
104. Zou, Y., et al., *A hand-driven portable triboelectric nanogenerator using whirligig spinning dynamics*. 2021. **83**: p. 105845.
105. Xu, S.-M., et al., *Multistaged discharge constructing heterostructure with enhanced solid-solution behavior for long-life lithium-oxygen batteries*. 2019. **10**(1): p. 1-10.
106. Wan, J., et al., *Ultrathin, flexible, solid polymer composite electrolyte enabled with aligned nanoporous host for lithium batteries*. 2019. **14**(7): p. 705-711.

107. Nayak, P.K., et al., *Photovoltaic solar cell technologies: analysing the state of the art*. 2019. **4**(4): p. 269-285.
108. Wang, G., et al., *All - polymer solar cells: recent progress, challenges, and prospects*. 2019. **58**(13): p. 4129-4142.
109. Haras, M. and T.J.N.E. Skotnicki, *Thermoelectricity for IoT—A review*. 2018. **54**: p. 461-476.
110. Hong, S., et al., *Wearable thermoelectrics for personalized thermoregulation*. 2019. **5**(5): p. eaaw0536.
111. Zhao, C.-e., et al., *Nanostructured material-based biofuel cells: recent advances and future prospects*. 2017. **46**(5): p. 1545-1564.
112. Dong, K., et al., *Shape adaptable and highly resilient 3D braided triboelectric nanogenerators as e-textiles for power and sensing*. 2020. **11**(1): p. 1-11.
113. Kwak, S.S., et al., *Butylated melamine formaldehyde as a durable and highly positive friction layer for stable, high output triboelectric nanogenerators*. 2019. **12**(10): p. 3156-3163.
114. Yoon, H.J., et al., *Microdischarge - Based Direct Current Triboelectric Nanogenerator via Accumulation of Triboelectric Charge in Atmospheric Condition*. 2020. **10**(25): p. 2000730.
115. Kim, J., et al., *High permittivity CaCu₃Ti₄O₁₂ particle - induced internal polarization amplification for high performance triboelectric nanogenerators*. 2020. **10**(9): p. 1903524.
116. Zhou, Y., et al., *Engineering materials at the nanoscale for triboelectric nanogenerators*. 2020: p. 100142.
117. Deng, W., et al., *Ternary electrification layered architecture for high-performance triboelectric nanogenerators*. 2020. **14**(7): p. 9050-9058.
118. Zou, Y., et al., *Advances in Nanostructures for High - Performance Triboelectric Nanogenerators*. 2021. **6**(3): p. 2000916.

119. Hinchet, R., et al., *Transcutaneous ultrasound energy harvesting using capacitive triboelectric technology*. 2019. **365**(6452): p. 491-494.
120. Seung, W., et al., *Dual Friction Mode Textile - Based Tire Cord Triboelectric Nanogenerator*. 2020. **30**(39): p. 2002401.
121. Dudem, B., et al., *Wearable and durable triboelectric nanogenerators via polyaniline coated cotton textiles as a movement sensor and self-powered system*. 2019. **55**: p. 305-315.
122. Jiang, C., et al., *All-electrospun flexible triboelectric nanogenerator based on metallic MXene nanosheets*. 2019. **59**: p. 268-276.
123. Hart, J.L., et al., *Control of MXenes' electronic properties through termination and intercalation*. 2019. **10**(1): p. 1-10.
124. Zhang, J., et al., *Scalable manufacturing of free - standing, strong Ti₃C₂T_x MXene films with outstanding conductivity*. *Advanced Materials*, 2020. **32**(23): p. 2001093.
125. Iqbal, A., P. Sambyal, and C.M.J.A.F.M. Koo, *2D MXenes for electromagnetic shielding: a review*. 2020. **30**(47): p. 2000883.
126. Li, K., et al., *3D MXene architectures for efficient energy storage and conversion*. 2020. **30**(47): p. 2000842.
127. Wang, D., et al., *Multifunctional poly (vinyl alcohol)/Ag nanofibers-based triboelectric nanogenerator for self-powered MXene/tungsten oxide nanohybrid NO₂ gas sensor*. 2021. **89**: p. 106410.
128. Dong, Y., et al., *Metallic MXenes: A new family of materials for flexible triboelectric nanogenerators*. *Nano Energy*, 2018. **44**: p. 103-110.
129. Gao, Y., et al., *MXene based mechanically and electrically enhanced film for triboelectric nanogenerator*. 2021. **14**(12): p. 4833-4840.

130. Xu, H., et al., *Construction of MXene/PDMS - Based Triboelectric Nanogenerators for High - Performance Cathodic Protection*. 2022. **9**(11): p. 2102085.
131. Dong, Y., et al., *Metallic MXenes: A new family of materials for flexible triboelectric nanogenerators*. Nano Energy, 2018. **44**: p. 103-110.
132. Gao, Y., et al., *MXene based mechanically and electrically enhanced film for triboelectric nanogenerator*. Nano Research, 2021. **14**(12): p. 4833-4840.
133. Xu, H., et al., *Construction of MXene/PDMS-Based Triboelectric Nanogenerators for High-Performance Cathodic Protection*. Advanced Materials Interfaces, 2022. **9**(11): p. 2102085.
134. Mashtalir, O., et al., *Amine - assisted delamination of Nb₂C MXene for Li - ion energy storage devices*. 2015. **27**(23): p. 3501-3506.
135. Lukatskaya, M.R., et al., *Cation intercalation and high volumetric capacitance of two-dimensional titanium carbide*. 2013. **341**(6153): p. 1502-1505.
136. Lian, P., et al., *Alkalized Ti₃C₂ MXene nanoribbons with expanded interlayer spacing for high-capacity sodium and potassium ion batteries*. 2017. **40**: p. 1-8.
137. Lipatov, A., et al., *Effect of synthesis on quality, electronic properties and environmental stability of individual monolayer Ti₃C₂ MXene flakes*. Advanced Electronic Materials, 2016. **2**(12): p. 1600255.
138. Chen, H., et al., *Pristine titanium carbide MXene films with environmentally stable conductivity and superior mechanical strength*. Advanced Functional Materials, 2020. **30**(5): p. 1906996.
139. Maleski, K., et al., *Size-dependent physical and electrochemical properties of two-dimensional MXene flakes*. Applied Materials & Interfaces, 2018. **10**(29): p. 24491-24498.
140. Tarhini, A., et al., *The effect of graphene flake size on the properties of graphene - based polymer composite films*. 2021. **138**(6): p. 49821.

141. Zhang, C.J., et al., *Additive-free MXene inks and direct printing of micro-supercapacitors*. 2019. **10**(1): p. 1-9.
142. Zhang, C., et al., *Highly porous carbon spheres for electrochemical capacitors and capacitive flowable suspension electrodes*. 2014. **77**: p. 155-164.
143. Zhang, R., et al., *Corrosion resistance of stretchable electrospun SEBS/PANi micro-nano fiber membrane*. 2020. **123**: p. 109394.
144. Yang, S., et al., *Exfoliated graphitic carbon nitride nanosheets as efficient catalysts for hydrogen evolution under visible light*. 2013. **25**(17): p. 2452-2456.
145. Wang, D., et al., *Multifunctional latex/polytetrafluoroethylene-based triboelectric nanogenerator for self-powered organ-like MXene/metal-organic framework-derived CuO nanohybrid ammonia sensor*. 2021. **15**(2): p. 2911-2919.
146. Sintusiri, J., et al., *Portland Cement-TiO₂ triboelectric nanogenerator for robust large-scale mechanical energy harvesting and instantaneous motion sensor applications*. 2020. **74**: p. 104802.
147. Kohara, K., et al., *Radial augmentation index: a useful and easily obtainable parameter for vascular aging*. 2005. **18**(S1): p. 11S-14S.

